Wearable Carbon Nanotube Sensors: Fabrication and Applications for Bio/Chemical Sensors

Seong-Joong Kahng

A dissertation

submitted in partial fulfillment of the

requirements for the degree of

Doctor of Philosophy

University of Washington

2019

Reading Committee:

Jae-Hyun Chung, Chair

Junlan Wang

Igor Novosselov

Program Authorized to Offer Degree:

Mechanical Engineering

University of Washington

Abstract

Wearable Carbon Nanotube Sensors: Fabrication and Applications for Bio/Chemical Sensors

Seong-Joong Kahng

Chair of the Supervisory Committee:
Associate Professor Jae-Hyun Chung
Department of Mechanical Engineering

With the advancement of micro/nanotechnology, wearable device technology is rapidly changing human lifestyle. Wearable devices armed with high-performance sensors potentially offer real-time health monitoring of human body conditions and produce massive database correlating physiological parameters with diseases, health, and behavior. However, most wearable devices do not offer wearer's comfort because the manufacturing methods are based on a stiff silicon substrate. Among nanomaterials, carbon nanotubes (CNTs) are emerging as electronic or sensing materials on a flexible substrate. For such devices, CNTs need to be patterned on a flexible substrate like polyethylene terephthalate (PET) film. Inkjet printing is one of the major patterning methods, but the pattern is discrete because of droplet-based printing.

Also, inkjet printing is limited by the ink properties, including surface tension and viscosity. Fountain pens can be used to print continuous lines but potentially damage the substrate. The contact printing methods may not be suitable to print multiple functional layers because the pen nib induces damage to existing layers.

In the dissertation, nano ink bridge-induced capillary pen printing is proposed as a novel method for continuous line printing of carbon nanotubes. Firstly, the control parameters of the noncontact capillary method are studied in terms of line width, edge roughness, and sheet resistance for uniform printing. Nanoink liquid bridge forms between the tip of the stylographic pen and substrate by capillary action. The printed pattern is characterized in the contexts of nano ink bridge formation between pen nib and substrate. Ink properties, printing temperature, printing speed, and contact angles are studied to find optimal printing conditions. The nano ink bridge-induced printing allows multiples layers of nanomaterials without damaging existing layers. This printing method facilitates the fabrication of low-cost wearable sensors on a flexible substrate. As printing applications, gas and pH sensors are demonstrated using the carbon nanotube pattern and chemical doping by the capillary pen printing method.

For biosensor fabrication, a point-of-care (POC) platform for tuberculosis screening is presented using a carbon nanotube film. Tuberculosis, caused by Mycobacterium tuberculosis (MTB), is one of the serious infectious diseases worldwide. Various methods are available for TB diagnoses, such as a Ziehl-Neelsen (ZN) method for microscopic detection, immunoassays for antigen detection, and polymerase chain reaction (PCR) for DNA or RNA detection. For a highly sensitive and specific screening tool, nanomaterials have been persistently investigated for infectious disease diagnosis. Resistive single-walled carbon nanotube (SWCNT) sensors have shown potential for rapid TB screening. However, hydrogen bonding on SWCNTs interferes the

resistance change due to target binding. In this dissertation, a resistive SWCNT biosensor is fabricated on a flexible film (PET) for low-cost TB screening. Silver electrodes are stamped as probing electrodes for SWCNTs. The sensing mechanism of SWCNTs, coupled with silver electrodes, is investigated in conjunction with hydrogen desorption. The sensitivity and specificity are characterized by MTB and surface antigen (MPT64) in physiological buffer. Subsequently, the sensor is characterized by tongue swab samples spiked MTB and MPT64. Simple resistive measurement is conducted before and after immunocomplex formation for detecting targets. The presented biosensor will offer a stepping stone for an inexpensive and versatile POC platform for rapid TB screening.

In summary, the critical challenges for SWCNT-based wearable sensors are addressed in terms of scalable fabrication and hydrogen bonding. The printing physics is investigated for nano ink-bridge induced printing of SWCNTs. A rapid TB screening sensor is developed with the investigation of hydrogen adsorption and desorption effects on SWCNTs. A thin, flexible sensing platform will facilitate the scalable fabrication of bio- and chemical sensors with low cost.

TABLE OF CONTENTS

LIST OF FIGURES

LIST OF TABLES

ACKNOWLEDGMENTS

The research and development in the dissertation were partially supported by the Office of the Assistant Secretary of Defense for Health Affairs through the Peer Reviewed Medical Research Program under Award No. W81XWH-17-1-0083. Opinions, interpretations, conclusions, and recommendations are those of the author and are not necessarily endorsed by the Department of Defense.

After one year at the University of Washington, I was trying to go back home because I could not find an advisor and a research topic. Blindly, I sent an email to Professor Jae-Hyun Chung to ask him whether I could get a chance to join in his lab. That is the start of my graduate study. I think that I am able to be here, thanks to my advisor. I also would like to thank Professor Junlan Wang, Professor Igor Novosselov, and Professor Youngjun Choe. They spared valuable time and supported me with good feedback.

Also, I would like to thank my people in True Light Church, my friends, and my family. Without their support and help, I would not be here.

DEDICATION

To my parents

Chapter 1. WEARABLE SENSORS

1.1 INTRODUCTION

With the pursuit of low-cost and portable smart technology, the form factor of sensors significantly decreases. The devices become cheaper and require minimal energy consumption. Wearable sensors play a critical role to obtain real-time information about human health and behavior in smart devices. According to the CCS Insight report in 2016 [1], the market of wearable technology will grow $34.2 billion in 2020. The total number of smart wearable devices will be 411 million units by 2020 (**Figure 1.1**)[1]. The products can be applied for health monitoring, disease diagnosis, and disease treatment. Fitness, activity & sports trackers will occupy about 76% among the segments.

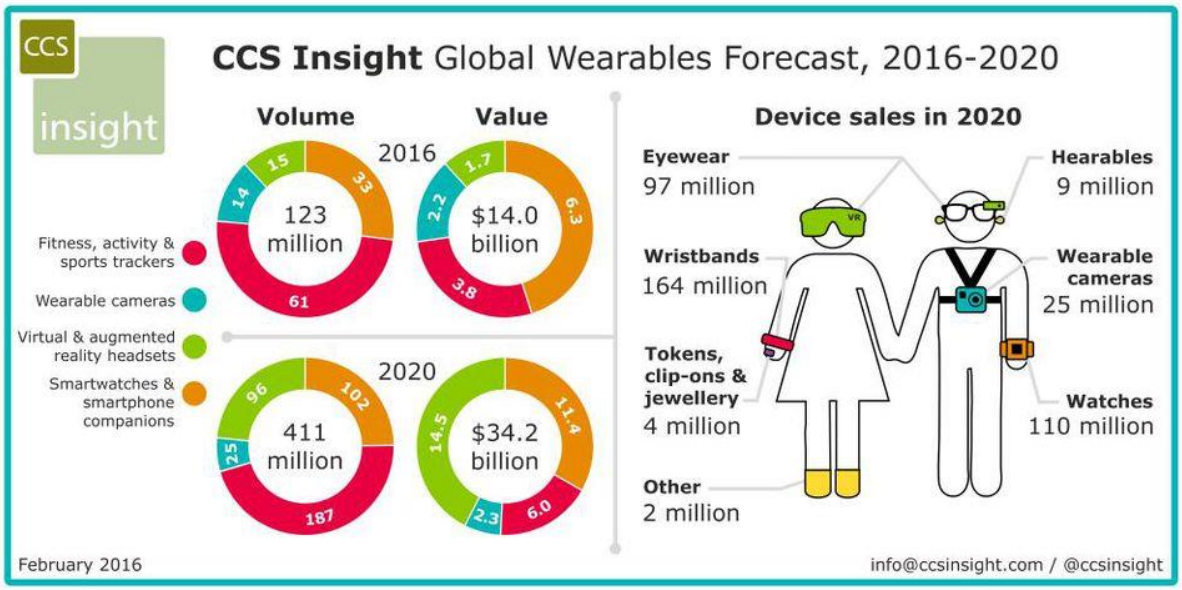

Figure 1.1. [1]. The estimated market of wearable devices between 2016 and 2020 (CCS Insight in 2016)

One of the promising fields in wearable devices is human behavior monitoring for healthcare. Physiological parameters, such as body temperature, heart rate, blood pressure, can be continuously monitored in daily life [2-4]. For example, the glucose level has been measured for diabetic patients with smart contact lenses in the eye [5, 6]. Smart contact lens provides painless and continuous glucose level monitoring while a conventional glucose meter is painful and discrete because human blood needs to be collected from the finger with an injection needle [7]. A normal pulsometer is embedded into a watch for continuous monitoring of heartbeats. These wearable monitoring devices are connected to a wireless network through a smartwatch to transfer the body information to a remote health care system for necessary treatment (**Figure 1.2**)[8].

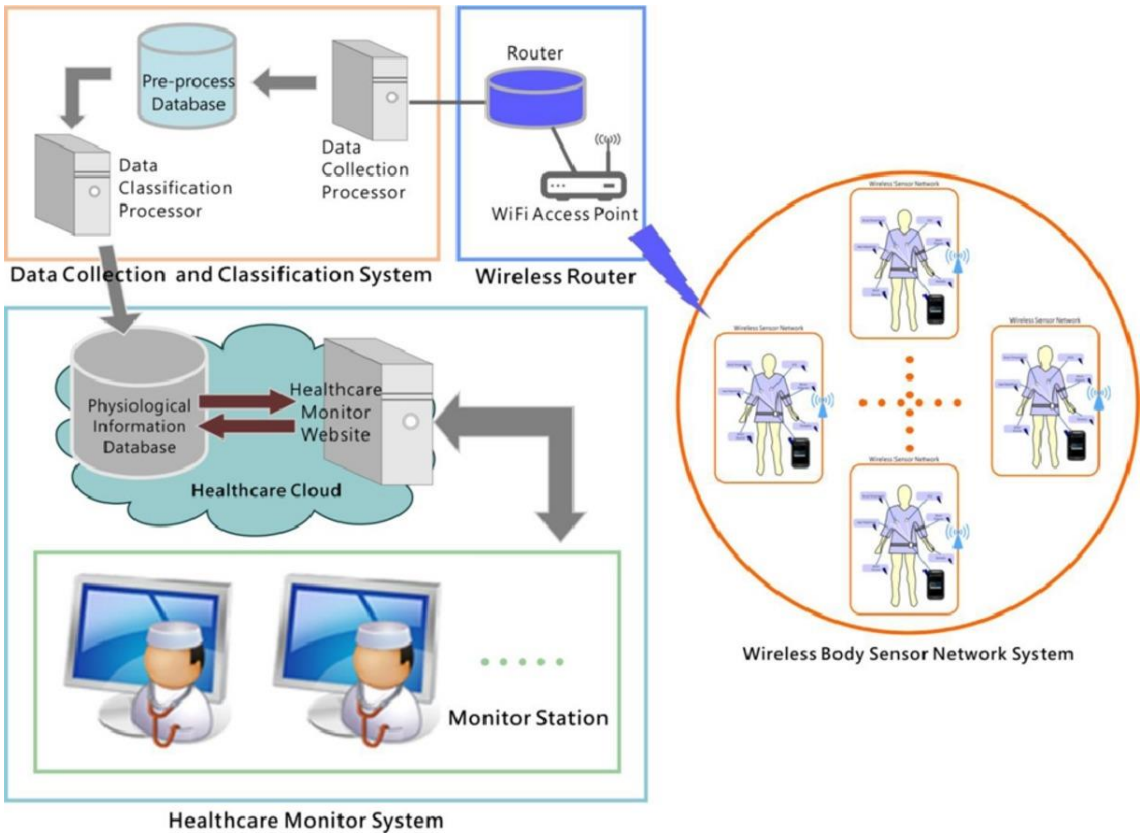

Figure 1.2. [8]. The scheme of the wireless network for wearable sensors

A small form factor is critical for portability and wearing comfort in wearable sensors [9]. Considering the major requirement for wearable sensors as flexibility, the substrate is limited to thin-film materials, such as paper, plastic, polymer, rubber. Low power consumption is an important factor for long-term operation and wireless data transfer [10]. To date, silicon-based semiconductor sensors have been used for smart devices because of the integration capability of various sensors into one chip. However, it is not flexible for curved human body profile. Although there are different types of flexible sensors, it is challenging to integrate the various sensors on a single substrate because each sensor shows different material and electrical characteristics. Sensor integration on a flexible substrate is a key step to multiplex various physiological parameters.

Personalized treatment for each is one of the growing fields in health care. Vital signs, such as heart rate, blood pressure, body temperature, and respiratory rate, are the basic physiological parameters of continuous human activity monitoring. For wearable applications of the sensors to the human body, sensors need to be soft, thin, and flexible. For whole body monitoring, a sensor array is needed to map whole human body conditions. The location of previous sensors has been limited to a few critical areas in the human body, such as arm, chest, and head. Wireless power could be used to operate the sensors and measure the parameters. Near field communication (NFC) technology with small size flexible patches was introduced as one of promising human body monitoring methods because of the simple wireless power transfer capability (**Figure 1.3**)[11]. This technology could be applied to in-hospital treatment, rehabilitation, and physical training like fitness [12]. Distributed pressure sensors on the whole

body can provide important information to prevent decubitus ulcers [13]. All the data on the whole body could be collected to a central control system through the wireless network [11].

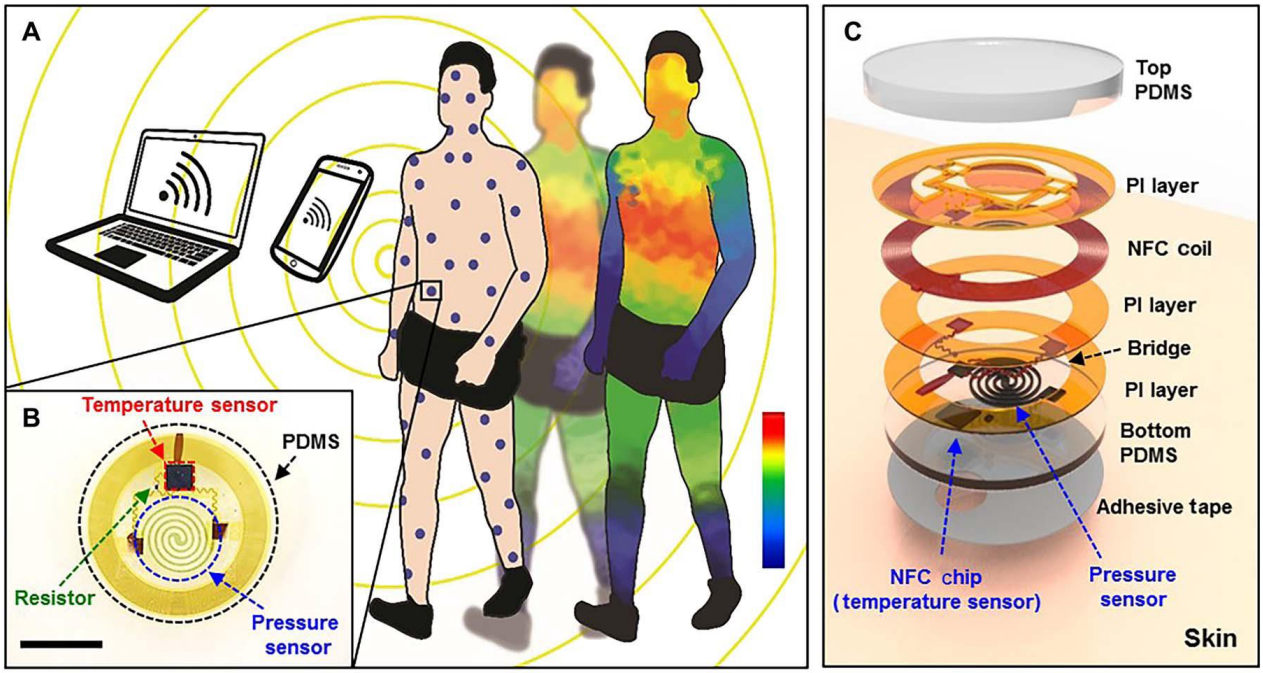

Figure 1.3. [11]. Battery-free small sized flexible sensors used for full-body monitoring. (A) Mapping data of body temperature and pressure through a wireless network. (B) Temperature and pressure sensor layout with NFC microchip (C) The device structure.

1.2 WEARABLE SENSORS

Temperature sensor: There are several test categories, such as electroencephalography (EEG) for electrical activity of the human brain, electrooculogram (EOG) for eye activity. One of the parameters is body temperature. Sleep disorder related to delayed sleep-wake phase, advanced sleep-wake phase, and jet lag can be diagnosed by mapping body temperature during sleep [13, 14]. A flexible temperature sensor based on graphite-filled polyethylene oxide (PEO) and polyvinylidene fluoride (PVDF) composites shows a high accuracy of 0.1˚C between 25 ˚C

and 42 ˚C [15]. The sensor shows consistent temperature performance under bending with different curvature and stretching on the skin surface (**Figure 1.4**). The sensing range from 25 ˚C to 42 ˚C for body temperature is ideal for medical diagnosis because the organs in the human body start to be damaged below 25 ˚C and over 42 ˚C. The sensing accuracy and physical stability of this sensor can be applied to a wearable device.

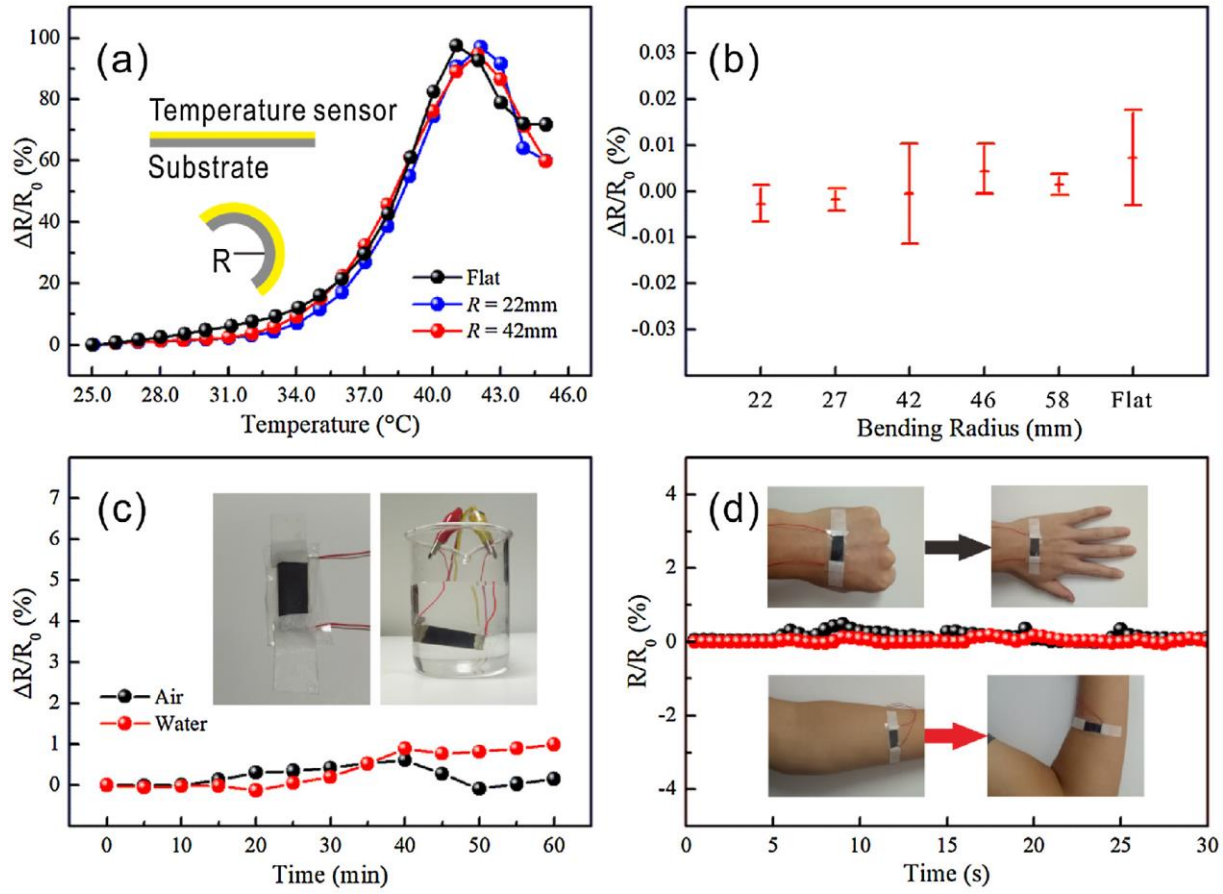

Figure 1.4. [15] (a) Comparison of temperature response between the flat sensor and bent sensors of different bending curvature (b) Resistance deviation of the temperature sensor under different bending radius. (c) Longtime measurement of the temperature sensor in the atmosphere and water. (d) Resistance deviation while stretching the arm and unclenching the fist.

The temperature coefficient of resistance (TCR) and PIN diode sensors are the resistant type of temperature sensor (**Figure 1.5**)[16]. These sensors are fabricated by semiconductor process on a flexible substrate, such as photolithography, etching, chemical vapor deposition, metal deposition. Due to the precise fabrication process, the sensor resolution is up to 1mm, and the sensitivity shows between 12 mK to 8 mK [16]. Although this sensor is wearable with high precision and ergonomic design, the fabrication is expensive and complicated.

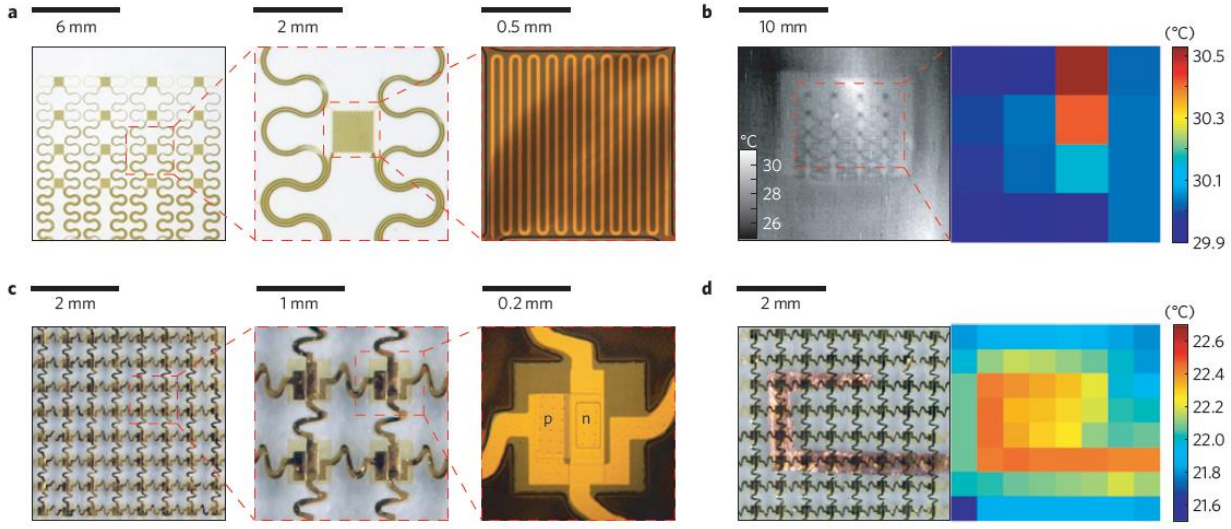

Figure 1.5. [16]. Epidermal temperature sensors (a) Images of a 4×4 the temperature coefficient of resistance (TCR) sensor array integrated on an elastomeric substrate (b) Infrared image of a similar device attached on human skin (left) and map of temperature (right), where each pixel represents the data of each sensor in the array. (c) Optical images of an 8×8 Si nano-membrane diode sensor array integrated on a thin elastomeric substrate (d) Optical image of a similar device mounted on a heater (left) and measured distribution of temperature (right).

Pressure sensor: Pressure sensors can be used for the heart rate monitoring through the pulse on the wrist or neck. A pressure sensor has been suggested on the zinc oxide (ZnO) nanoneedle/polyvinylidene difluoride (PVDF) hybrid film. The highly sensitive sensor could

detect down to 4 Pa [17]. The piezoelectric material produced an electrical potential by the deformation of the crystal structure due to an external force. The dielectric property increased a piezoelectric potential. The sensitivity of the PVDF-based sensor could be improved by the ZnO nanoneedle. This hybrid film sensor could be applied to heart rate monitoring in real time because of the rapid response and durability (**Figure 1.6**)[17].

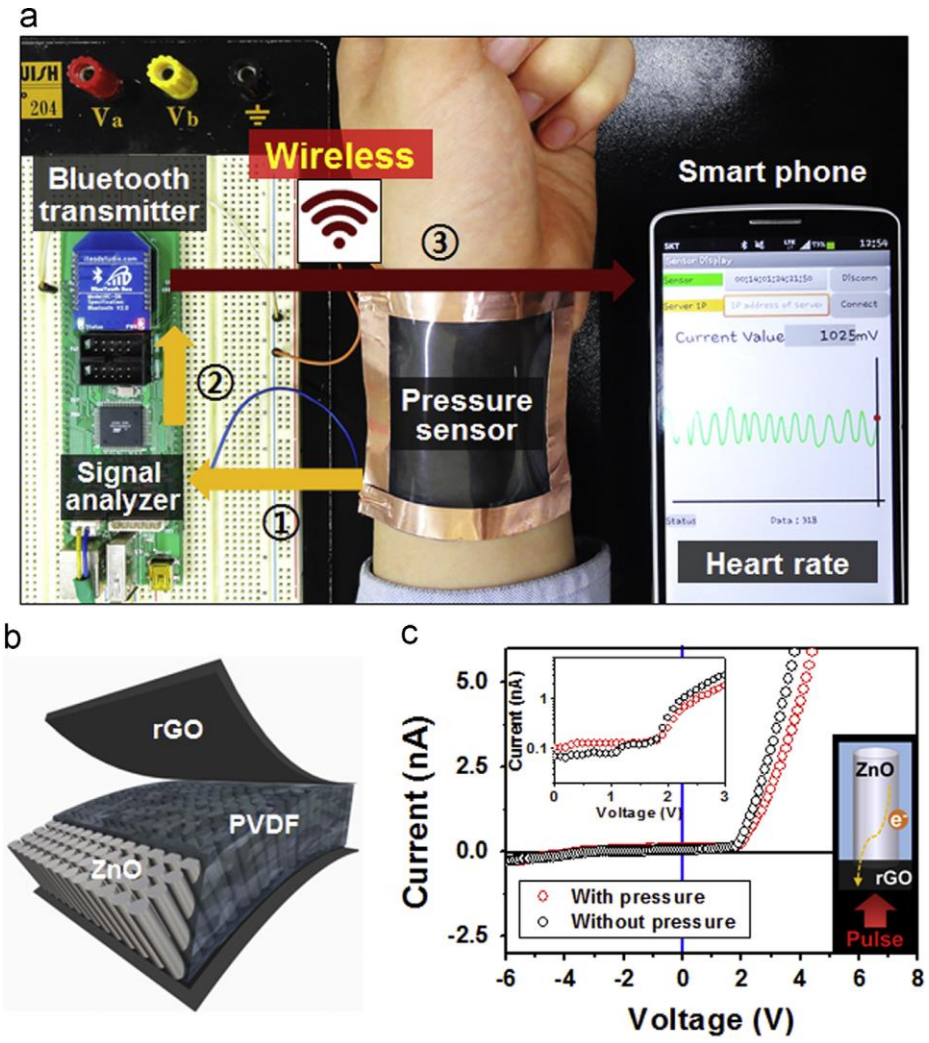

Figure 1.6. [17] (a) image of wearable and wireless heart rate sensor and (b) structure of the pressure sensor using ZnO/PVDF hybrid film between rGO electrodes. (c) The I–V curves of the pressure sensor that rectifying the behavior of Schottky contact under compressive strain. The insets show a log I vs. V plot and schematic illustration of forward bias when pressure is applied.

A piezoresistive sensor composed of polyvinylidene fluoride-co-hexafluoropropene (PVDF HFP) / poly(3,4-ethylenedioxythiophene) (PEDOT) were proposed as a blood pressure sensor (**Figure 1.7**) [18].

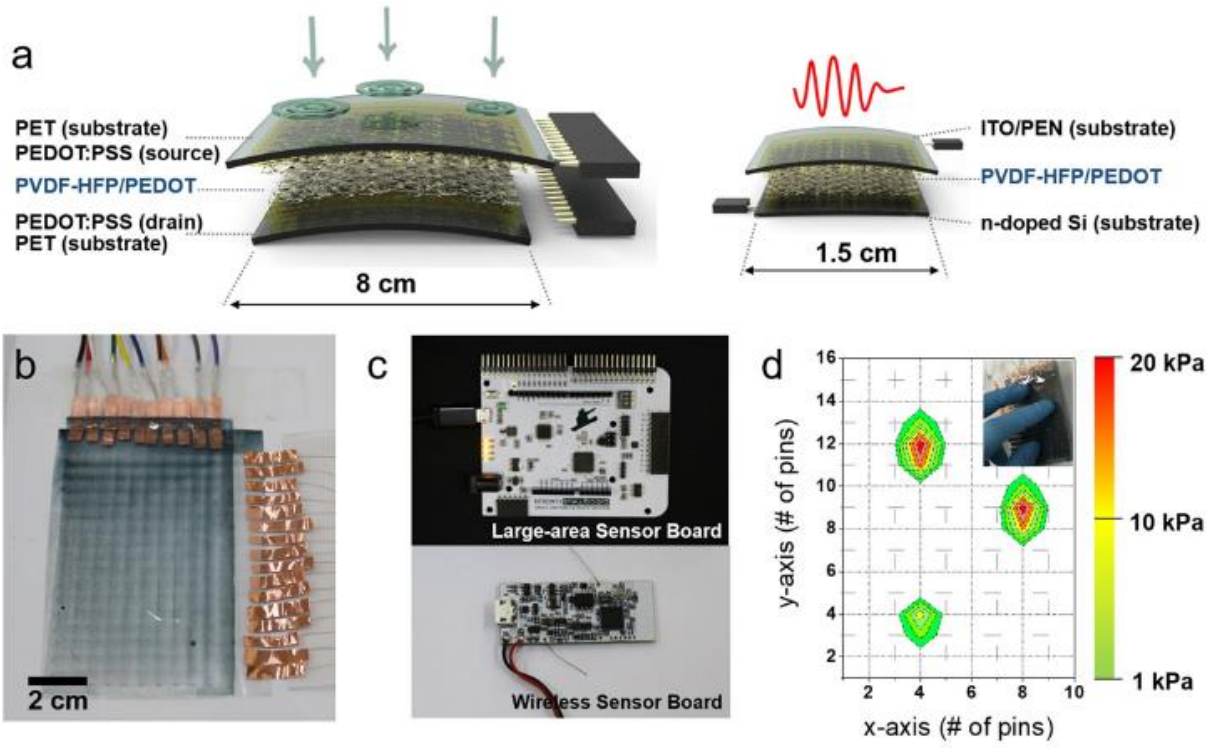

Figure 1.7. [18]. Blood pressure sensor using spherical bump PVDF HFP/PEDOT 3D NF mats. (a) Schematic view of the sensor matrix (left) and single-unit sensor systems (right). (b) Images of a PVDF-HFP/PEDOT array on an inkjet-printed electrode PEDOT: PSS/ PET film, (c) circuit board for pressure mapping (top) and a Bluetooth board (bottom). (d) Blood pressure mapping using a PVDF-HFP/PEDOT array sensor.

Strain sensor: Most piezoelectric strain sensors are highly sensitive, with small time constant and low power consumption. The main problems are poor flexibility, limited stretching capability, and low dynamic range. Piezo-resistive strain sensors consisting of CNTs have the

flexibility and good electrical property suitable to wearable sensors [19]. These can be utilized for human body movement by detecting the deformation of skin and joints. Damaged vocal cords, respiratory disorders, and angina can be diagnosed by monitoring abnormal behavior of muscle with a strain sensor. The CNT sensors can be applied to orthopedic applications to evaluate the inner spatial gap between bones and to determine the degree of change of spinal posture. Parkinson's disease can be diagnosed by detection of body movement of the arm, armpit, knee, waist, and spinal [20, 21] (**Figure 1.8**).

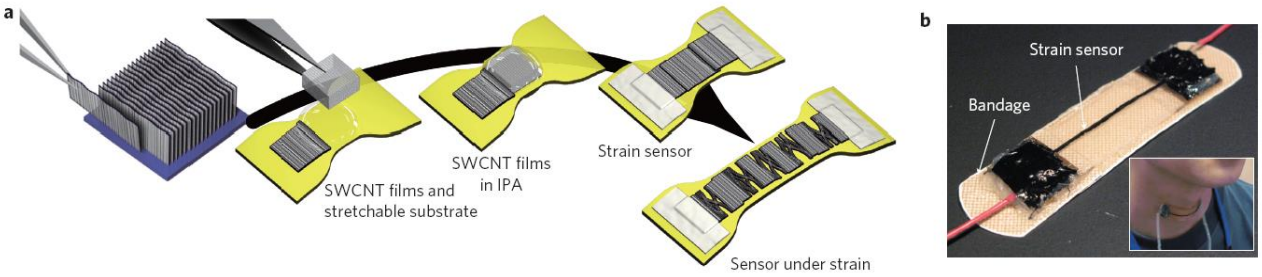

Figure 1.8. [21]. (a) The fabrication process of a vertically aligned SWCNTs strain sensor. (b) A bandage strain sensor fixed to a neck

For a strain sensor, a simple circuit model can be used (**Figure 1.9**). When a sensor is stretched, the resistance of R_1 is almost the same. With the bridge elongation, R_c shows linear behavior in the resistance value, while the resistance of R_2 increases exponentially with strain. The resistance change by strain is described as $R = 2R_1 + R_c$ [21].

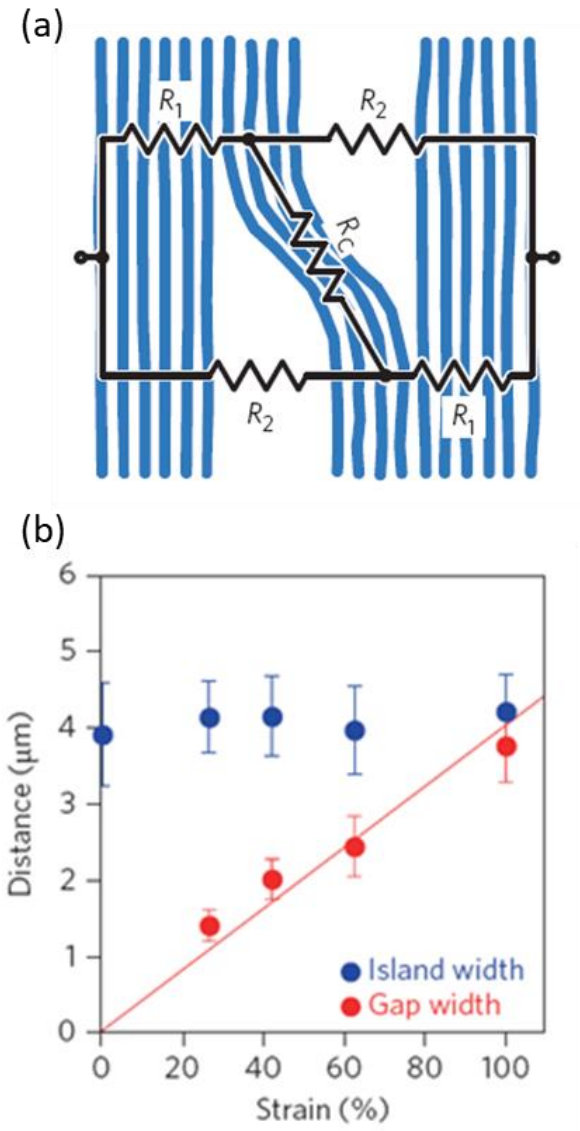

Figure 1.9. [21] (a) Model of the strain sensor. R_1, R_2, and R_c are the resistances of the island, gap, and stretched elongation bridge, respectively. (b) Average island width (blue) and gap (red) versus strain for cycling following the conditioning step.

Sweat sensor: A sweat sensor becomes one of the prime targets for health care because sweat contains critical data for health monitoring, disease diagnostic, and athletic performance evaluation [22]. Ions, metabolites, and hormones have been tried to apply for sweat analysis

using a sweat sensor [22]. Sweat sensors enable the measurement of the rate of sweat secretion and sweat sampling in real time. Sweating mechanism is complicated because the composition of ions and secretion rate are correlated [23]. Higher sweat rate increases the concentration of sodium and chloride ions. Dehydration during exercise makes sports ability worse [24]. In contrast, lactic acid and urea show higher proportion at a lower sweat rate [25]. Measuring the sweat rate has emerged as one of the key parameters to monitor physiological conditions.

Conventionally, sweat rate measurement has been tested in a specific test environmental with wired sweat patches [26]. One of the sweat rate sensors is an optical type that uses external light due to the lack of light in the sensing system [27]. Sweat sampling is complicated because sweat is prone to evaporate and contaminate with conventional methods. The sweat at the very beginning could be mixed with later discharged sweat, which could result in inaccurate data [28].

Micro-fluidic sampling can be a great alternative to these problems. An encapsulated microfluidics controls the samples without problems, such as evaporation condition, mixing of old and new samples, and contamination with another chemical [27]. There is a micro-fluidic sweat sensing patch with the chemical and electrical sensor inside the microfluidic channel for better analysis [29]. This sensor is composed of a flexible micro-fluidic channel and substrate for body attachment [29] (**Figure 1.10**). The microfluidic device detects ions in sweat and measures the sweat flow rate simultaneously to analyze the relationship between ion concentration and sweat secretion rate [29]. This system enables a real-time analysis for instantaneous feedback with the printed circuit board (PCB) that is integrated with signal processing and data transmission. With the integrated system, the existing problems could be eliminated due to the advantages of a micro-fluidic channel device [29].

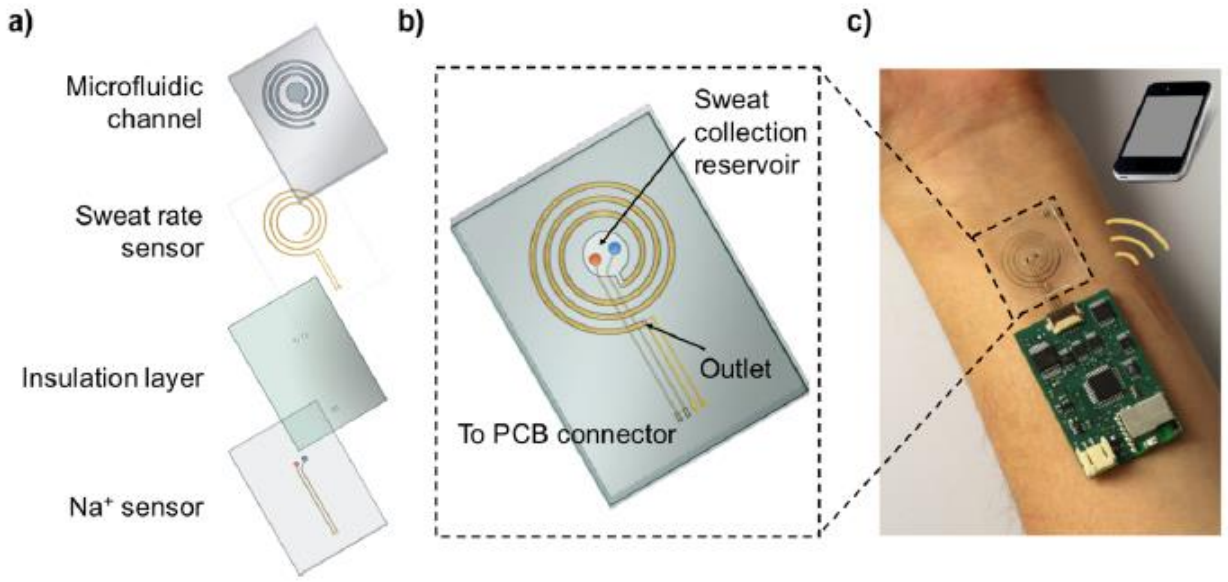

Figure 1.10. [29]. Illustrate a wearable sweat sensor. (a) a spiral-patterned microfluidic channel, Au electrodes for sweat rate sensing, an insulation layer, and Na^+ sensing electrodes. (b) Structure of the microfluidic device. The aligned Au electrodes with the microfluidic channel. The Na^+ sensor at the sweat collection reservoir. (c) The sweat sensor on human skin. The collected data from the sensor can be transferred to a cellphone through a wireless network.

In summary, it is an early stage to apply wearable sensors for ubiquitous health monitoring, but the wearable sensor technology is a rapidly growing field. The main challenge is to integrate various sensors, a battery, and wireless communication chips on a flexible substrate [30]. The separation and delamination between sensors and a substrate can be a mechanical stability issue caused by different thermal expansion and Young's modulus. Power supply and wire harness are a hurdle to be addressed. The thin film sensors measuring temperature, pressure, and strain sensor have been proven useful for health monitoring and disease diagnosis. Flexible power-generators producing electrical energy from mechanical energy can be an option to operate flexible sensors and electronics [31]. The sensors will be developed for transferring, sharing, and analyzing all data for the Internet of Things (IoT) platforms.

1.3 NON-CONTACT PRINTING METHODS

Non-contact micro and nano-printing technologies have been of great interests for various fields of electronics (**Figure 1.11**)[32] and biotechnology [33]. Major non-contact micro- and nano-printing technologies are; inkjet printing [34], pyro-electrodynamic printing [35], electro-hydrodynamic printing [36], surface acoustic wave (SAW) printing [37], dielectrophoretic (DEP) printing [38], and pen printing/deposition [39, 40]. In comparison to noncontact printing methods, contract printing methods can potentially damage underlying layers and diminish the quality of print [41]. Also, adhesion between water-based ink and the hydrophobic substrate can cause problems in relation to capillary forces [41].

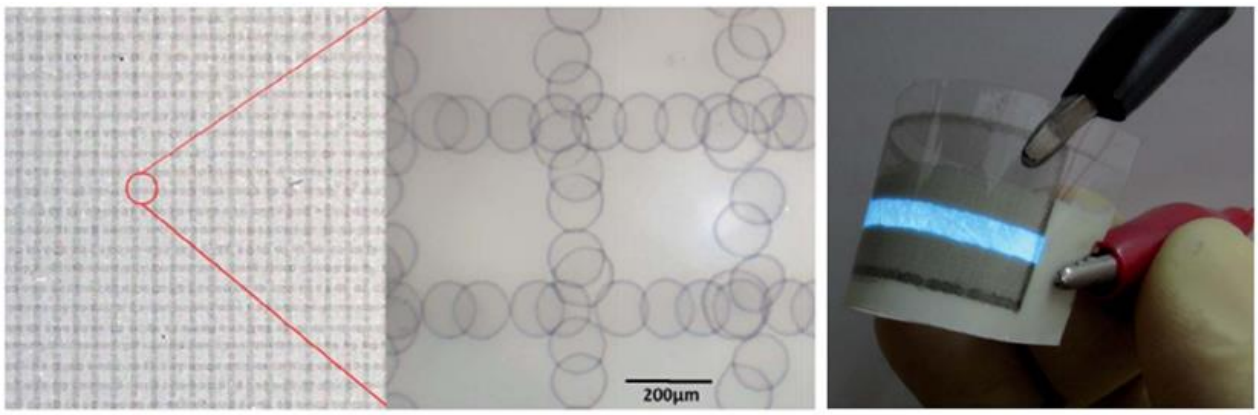

Figure 1.11. [32]. Patterned CNTs grid by inkjet printing and EL devices.

The working principles of thermal inkjet printing, piezoelectric inkjet printing, electrostatic inkjet printing, and 3D inkjet printing are similar in that the reservoir volume is

changed to eject ink. For thermal inkjet printing, flash heating is applied next to a micro-sized nozzle to induce instantaneous bubbling. The ink volume change pressurizes a portion of ink out of the chamber. The weakness in this method is that the molecules in ink should be able to withstand high temperatures. Biomolecules can be damaged at high temperature. High-Speed printing is challenging for thermal inkjet printing.

Piezoelectric printing uses the electromechanical vibration by the piezoelectric element to generate the kinetic energy of ink in a reservoir (**Figure 1.12**) [42]. The energy needs to be enough to break the surface tension in order to eject ink onto the substrate. However, piezoelectric printing is vulnerable to viscous ink because of the requirement of a higher level of energy. For high viscosity, this printing method may not be able to achieve the kinetic energy to eject an ink droplet.

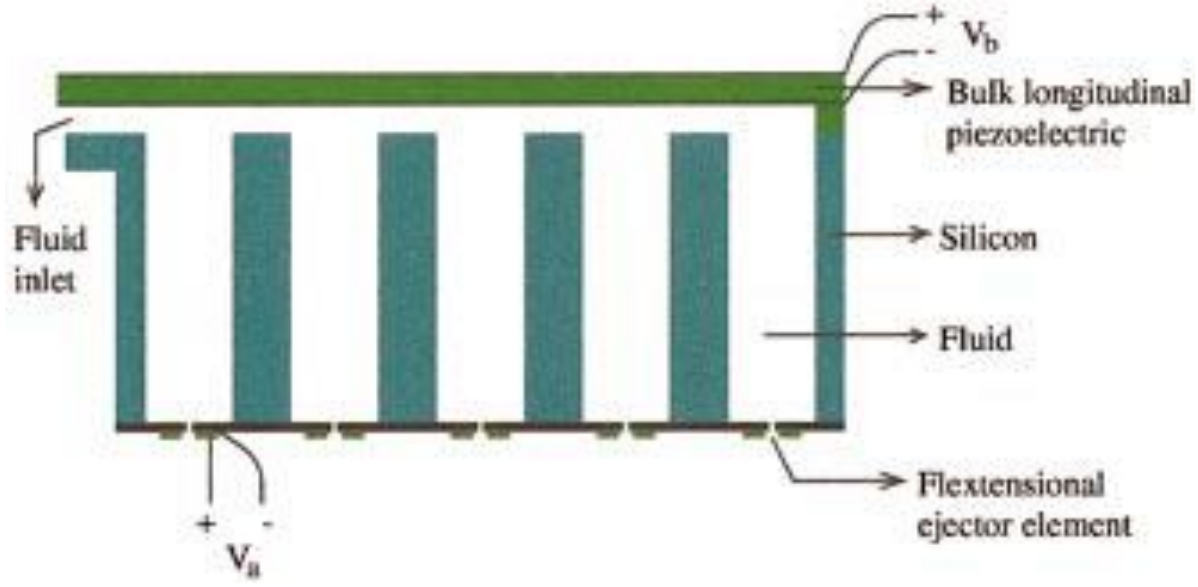

Figure 1.12. [42]. Structure of the micromachined droplet ejector.

Electrostatic inkjet printing ejects ink by the reservoir volume change [43]. The problems caused by heat or mechanical vibration can be avoided by using electrostatic force. However, working life is short [42].

3D printing dispenses polymer ink layer by layer to build a 3D object. The performance of inkjet printers is related to the viscosity of the ink and the nozzle size. Viscosity influences the printing speed as well as the material capability for printing.

All inkjet printers are influenced by ink viscosity, surface tension, particulate, and nozzle size. Particulate is a big challenge because the nozzle can be clogged by the particles in ink [44]. The resolution of inkjet printing is, therefore, unavoidably confined by particle dimensions and nozzle sizes.

Pyroelectrodynamic printing does not require electrodes or nozzles because liquid droplet is drawn from the liquid film reservoir by the pyroelectric effect. Two plates are prepared with a gap and a heat source of a heated tip in the system. A top plate is lithium niobate, and a bottom glass plate contains a liquid reservoir (**Figure 1.13**)[35]. The heat source generates thermal stimulus and occurs the electro-hydrodynamic phenomenon on the top plate by the pyroelectric effect. Local electric field exceeds a critical value and forces the ink from the top plate reservoir to be pulled on a substrate. The droplet is as small as 300 nm in radii. This printing method generates a different radius of the droplet depending on the reservoir size. The printed droplet size can be controlled, but the reservoir should be changed during the printing process. Using multiple reservoirs can address the issue of printing multiple sizes.

Pyroelectrodynamic printing is limited by the printing mechanism using heat like thermal inkjet. Heat sensitive ink material like biomaterial cannot be printed with this method. The printing speed is comparatively low due to the time to heat the substrate, though the array of the

heat source can print multiple points simultaneously.

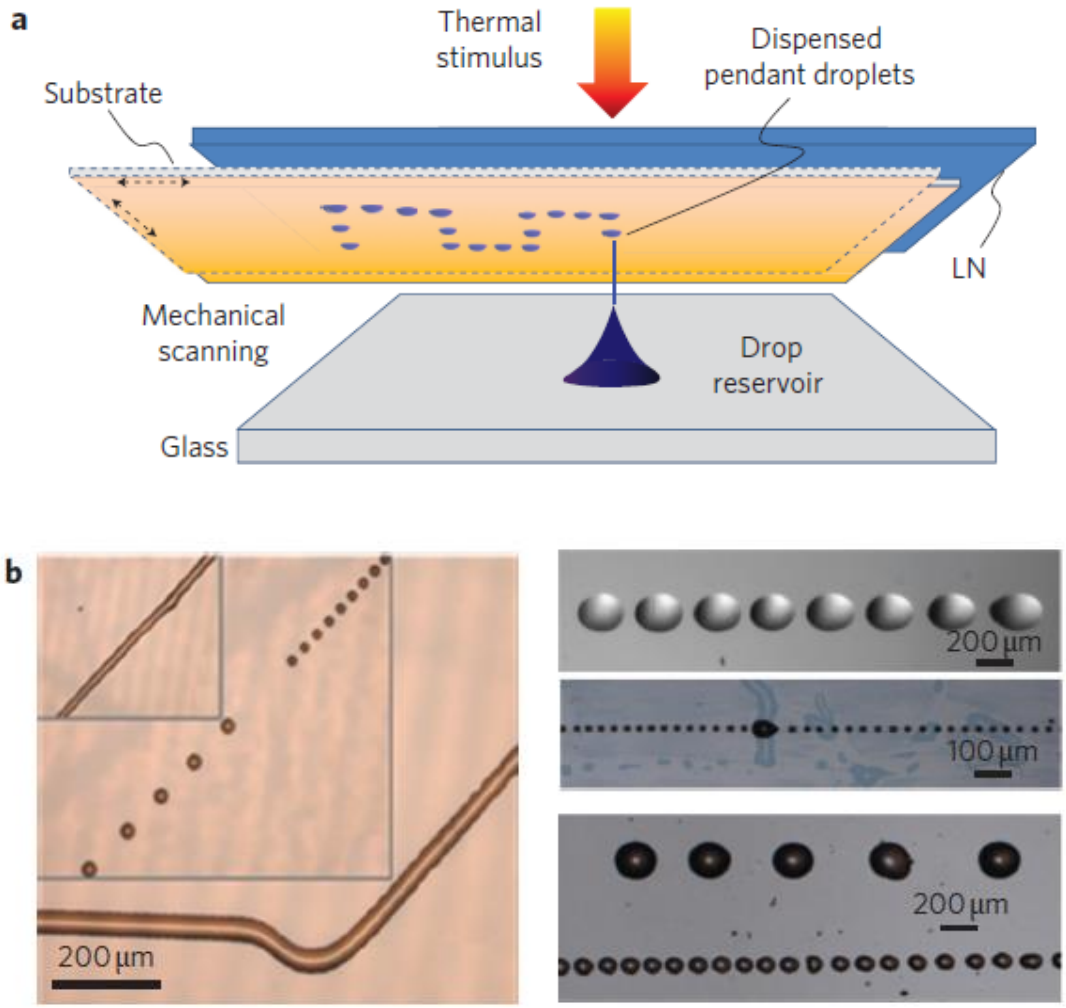

Figure 1.13. [35]. (a) Schematic image of pyroelectrodynamic printing using the LN. (c) Various patterns by pyroelectrodynamic printing, such as separate droplets, straight and curved lines.

For electrohydrodynamic (E-jet) printing, an electric field is applied to the nozzle tip and substrate to drive the ionized ink to the nozzle (**Figure 1.14**)[36]. Due to an electric field, an E-jet printing nozzle must be electrically conductive, and the substrate needs to be metallic or semiconductive.

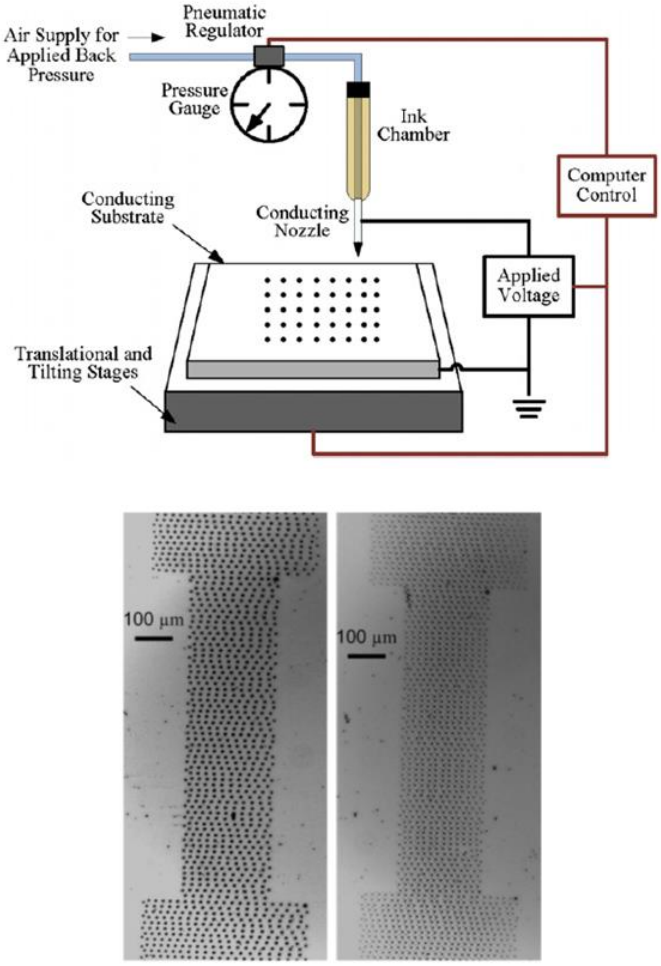

Figure 1.14. [36]. Schematic of the E-jet printing set-up (up) and printed patterns using constant voltage jetting (down left) and pulsed voltage jetting (down right).

By the electric field between the nozzle and substrate, the ions accumulate at the tip of the nozzle. Mutual Coulomb repulsion between the ions causes tangential stress on the liquid surface. The repulsion force deforms the meniscus into a conical shape called Taylor cone. The ink is printed from the tip of a Taylor cone when the electrostatic force of the ionized ink breaks the surface tension. The droplet is smaller than the submicron nozzle size. Printing speed and droplet size can be controlled by a pulsed DC signal. Using DC pulse widths ranging from 500 μs to 2500 μs, the droplet size from 3.9 to 8.1 μm is obtained with the standard deviation of 0.4

μm and 0.3 μm.

Electrohydrodynamic printing was investigated to overcome the weaknesses of other printing methods. The potential problem of electrohydrodynamic printing lies in need of a metal/conductive printing orifice. The orifice may be affected by the ink substance. To generate an electric current, the substrate needs to be either metallic or semiconducting. A major disadvantage is to limit the printing substrate to conductive materials. The printing may not be achieved on non-conductive material such as polyethylene terephthalate (PET) film.

Surface acoustic wave (SAW) printing uses an acoustic wave field to control the fluid's movement (**Figure 1.15**)[37]. The electro-elastic wave with nanometer level amplitude propagates through the surface of an elastic substrate. This printing method is capable of nanometer resolution while either a nozzle or orifices is not required. Random patterns may not be generated by using SAW printing.

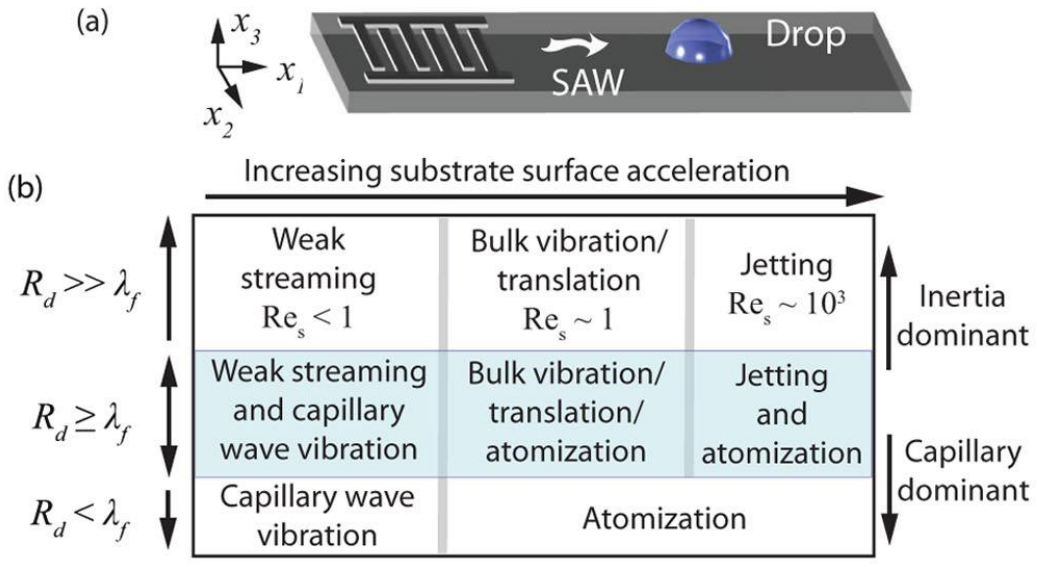

Figure 1.15. [37]. (a) Schematic view of the SAW (b) Relation between the surface acceleration magnitude and the drop size and behavior of the drop.

For dielectrophoretic (DEP) printing, DEP induces a force on the colloidal particle suspended in the liquid when DC voltage creates an electric field between the nozzle and the substrate. The DEP force results in a 175nm-size pattern of the colloidal particles on the substrate using a 150 nm nozzle (**Figure 1.16**)[38]. DEP force is subject to the dielectric constant of the liquid and the colloidal particle. The eligible printing materials are DNA [45], protein [46], the polymer [47], and metal particle. DNA, protein, and polymer materials are deposited by DEP force on the pre-patterned electrode without a nozzle

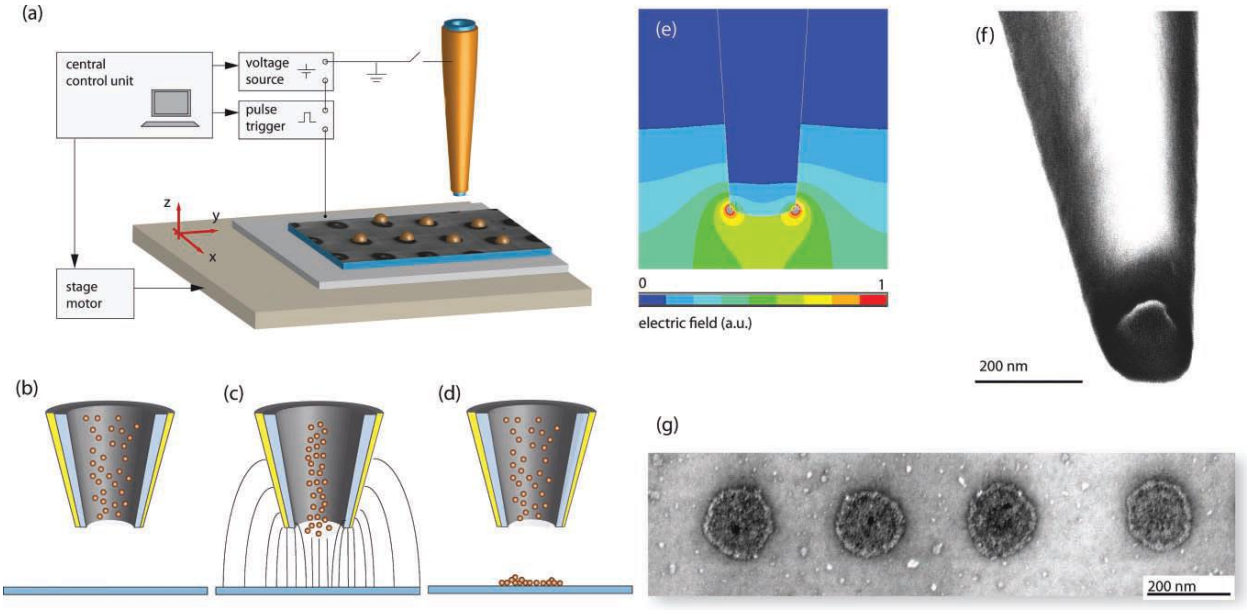

Figure 1.16. [38]. (a) Schematic of the Dielectrophoretic (DEP) printing setup. (b)–(d) The dispensing mechanism of the Dielectrophoretic (DEP) printing (e) demonstrates the electric field distribution of the nozzle. (f) Scanning electron microscopy image of glass capillary (g) Scanning electron microscopy image of corresponding Au-dots by DEP printing.

Dip-pen nanolithography utilizes capillary forces to carry molecular ink from the tip to a substrate as a nanometer size during micro-contact (**Figure 1.17**)[39]. Dip pen uses various

materials such as ink, polymers [48], DNA [49], bacterial cell [50], proteins [51], and metal particles[52]. Dip Pen is influenced by viscosity, ambient conditions, adhesion properties, substrate grain size, print speed, and contact time [39]. After being dipped in ink, the pen makes a pattern on a substrate. The pattern size is related to the interaction between the ink and the substrate. The binding force between the ink and the substrate by chemisorption or self-assembly limits the diffusion length to stabilize the pattern. The printing characteristics depend on the ink properties and the substrate. Ambient environmental conditions can affect the ink evaporation causing potentially unfavorable effects like the coffee ring effect. Such printing conditions can affect the printing resolution.

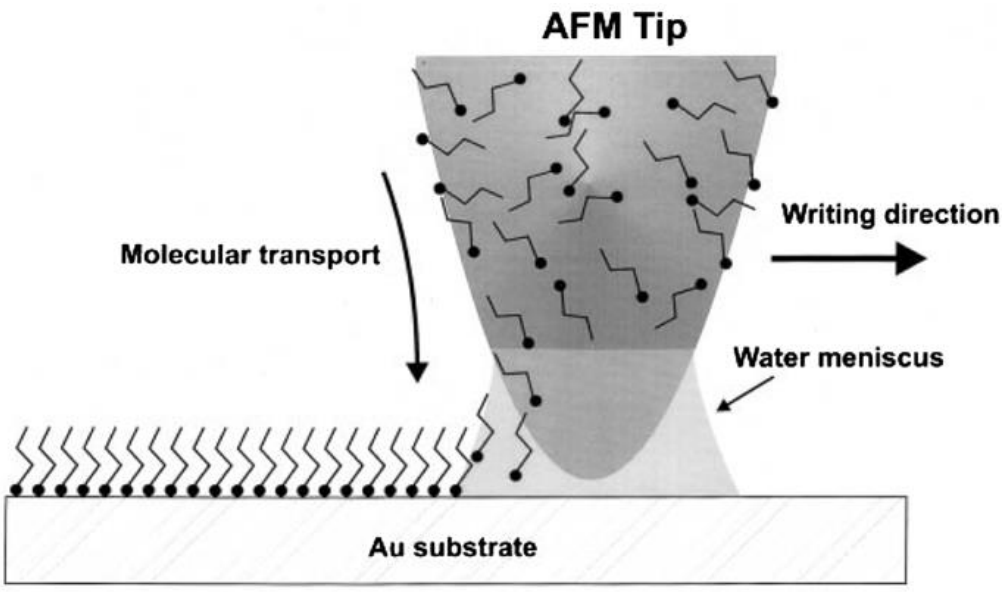

Figure 1.17. [39]. Illustration of dip-pen nanolithography (DPN) writing.

A nano fountain pen method uses a tapered pen tip that can be fabricated with a heat-drawn hollow glass or quartz. Ink is delivered through a channel of a few hundred nanometers

onto a substrate by capillary [40, 53, 54]. The liquid droplet stays on the tip by surface tension until the tip is in contact with the substrate. The ambient environmental condition affects the drying condition of the water-based ink. The condition causes the coffee ring effect to the printed pattern like dip pen lithography [55]. Polymer [56], metal [57], carbon nanotube [58], and protein [40], have been patterned by a nano fountain pen.

Printing method	**Precision**	**Nozzle**	**Nozzle structure**	**Contact**	**Printable materials**
Thermal inkjet	Micron	Yes	Complex	Non-contact	polymer, metal
Piezoelectric inkjet					polymer, metal
3-D inkjet					polymer, ceramic, glass
Electrostatic inkjet	Submicron				polymer, metal
Electrohydrodynamic			Simple		polymer, DNA, protein, metal
Dielectrophoretic					polymer, DNA, protein, metal
Pyroelectrodynamic		No			nanotubes, nanowires
SAW					polymer, metal
Dip-pen nanolithography				Contact	polymer, DNA, protein, metal
Nano fountain pen					polymer, DNA, protein, metal

Table 1. [42]. Characteristics of printing methods.

All the printing methods are summarized in (**Table 1**) [42]. Inkjet printers are widely used in comparison to other printing methods, though the inkjet resolution has micron precision. The complicated structure of the nozzle is fabricated by the semiconductor fabrication process. In spite of scalable production capability, the cost of the semiconductor process is high. Ink

materials affected by heat or mechanical vibration may not be allowed for inkjet printing. Dip-pen nanolithography and nano fountain pen are capable of using various ink materials, but these printing methods cause substrate damage because of physical contact in printing [59].

1.4 CHALLENGES

To print multiple layers of different nanomaterials on a 2-D substrate, various approaches have been investigated. Among them, non-contact printing is preferred to avoid potential damage to the substrate or the previously-printed layers. Inkjet-style printing [60-62] is the most common basis of various commercially available techniques. Thermal and piezoelectric inkjet printing methods use thermal expansion and electromechanical vibration to eject droplets, overcoming surface tension in the formation of droplets [60, 63]. Due to the physics of droplet formation, inkjet printing is limited in the range of viscosities and values of surface tension of the working fluid [64, 65]. When the nano-ink of interest has high surface tension and low viscosity, cumbersome change of ink properties is performed to generate a stable droplet [32, 66, 67].

Additionally, fragile biomolecules are not compatible with the high pressures, heat, and shear stresses associated with printing through inkjet methods [64, 68, 69]. Electrohydrodynamic printing utilizes an electric field to accurately control flow through a nozzle [70-72] but is limited to conductive or semi-conductive substrates. Pyroelectrodynamic printing uses the pyroelectric effect to cause the localized electric charge to pull drops to the substrate [73, 74]. Dielectrophoretic printing [38] and surface acoustic wave printing [37] use electric- and acoustic fields, respectively. However, printing capabilities on a 3-D surface have not been reliable.

Stencil printing [75] can spray nanomaterials through a mask pattern but is limited in random patterning.

As an alternative to current nanoparticle printing methods, fountain pens [76-78], ball pens [79] and pencils [80, 81] have been demonstrated in nanomaterial printing. However, these contact printing methods could cause damage to the substrate [78], which impedes the printing of multiple layers or large scales. For nanoscale patterning, dip-pen lithography [39, 82] has been developed for molecular printing but has limitations in terms of scalability and nano ink delivery. When using capillary pens, the nano-ink can evaporate and dry at high rates inside the capillary tube or needle, which restricts their use to very short times. This represents a major hurdle for scalable printing of molecules.

1.5 OBJECTIVES

To address the main challenge of SWCNT printing on a film, we study capillary pen printing through a nano ink bridge. The presented approach would avoid the drawbacks of surface damage due to the contact of the pen's nib on the substrate and enable the patterning of multiple layers. In particular, we propose to use a stylographic pen that consists of a capillary nozzle and a rod-shaped ink stopper.

The proposed study consists of two steps. The first is to investigate the effect of varying control parameters on the uniformity of printed features, such as width, edge roughness, and sheet resistance of the printed line on a 2-D surface. To enhance the uniformity of the printed line, the substrate can be heated to control the contact angle and evaporation of the solution. Through the dot test, the spread of the solution and the contact angle is measured under a

different temperature condition of the substrate. Moreover, then, the line is drawn by the Rotring pen. The contact angle is the key parameter for the printed line property.

Using printed SWCNTs, chemical sensors will be developed. The existing printing method is challenging to fabricate continuous line and multiple layers for doping with chemicals because of the nature of discrete drop printing. To make a continuous line, the printing needs to be repeated with alignment. Using the proposed printing methods, gas and ion sensors will be developed.

Chapter 2. NANOINK BRIDGE-INDUCED CAPILLARY PEN PRINTING

2.1 INTRODUCTION

Since the discovery of carbon nanotubes (CNTs), various patterning methods have been investigated to develop chemical and biological sensors. Early methods relied on direct growth on a substrate, assembly using an electric field, and self-assembly [83-85]. In the fabrication of wearable sensors, a non-contact printing is preferred to avoid potential damage to the substrate or existing layers. Mostly inkjet printings [60-62] utilize the principle of the thermal expansion or electromechanical vibration [60, 63]. Formation of the droplet relies on the viscosity and surface tension [64, 65], which often requires significant modifications of ink properties [32, 66, 67]. To achieve electrical conductance of the printed CNT patterns, the discrete nature of droplet deposition requires the ejector shift to connect the drops. In the printing of biological materials, it may not be usable because the high pressures, heat, and shear stresses in inkjet reservoir could damage the fragile biomolecules [64, 68, 69]. Electrohydrodynamic printing makes use of an electric field to eject ink through a nozzle [70-72], so conductive and semi-conductive substrate have to be used. Stencil printing [75] deposits nanomaterial by spraying through an open stencil mask, which is limited to the designed masking pattern.

Fountain pens [76-78], ball pens [79], and pencils [80, 81] have been researched to pattern nanomaterials. For fountain pens, the capillary force attracts ink into the tube and provides the

pressure gradient to hold ink column inside. When the capillary tube is in contact with a porous paper, the capillary pressure in pen decreases due to the contact between the nib and the porous substrate, resulting in ink flow [86]. However, printing on an impermeable film is more challenging as the contact angle is much greater than 0°. Moreover, any contact printing may damage the substrate [78] hindering multiple layer deposition required for complex sensor structures.

2.2 OBJECTIVES

In this chapter, a noncontact capillary pen printing method is characterized. The technique is demonstrated by patterning single-walled carbon nanotubes (SWCNTs) via a nano ink liquid bridge. The non-contact printing method does not physically damage the substrate or previously deposited layers. A single pass printing is sufficient to obtain a measurable electrical resistance. The resistance and the optical properties are characterized for several print geometries: a dot, a line, and a film.

2.3 NANOINK BRIDGE-INDUCED PRINTING

The noncontact capillary method deposits nano ink through a liquid bridge forming between a capillary pen and substrate (**Figure 2.1**a). A stylographic pen consists of a capillary nozzle and a rod-shaped ink stopper that assures nano ink seal when the pen is not used. During

printing, two geometric parameters require control in order to maintain the capillary bridge integrity: the pen tip height (H) from the substrate and the advancing bridge contact angle (θ_{B_a}) as illustrated in (**Figure 2.1**a). When the liquid bridge is established, the ink flow rate depends on the pressure difference between the capillary pen reservoir and the substrate surface. In a static condition, θ_{B_a} is dependent on the substrate surface properties, its temperature, and ink properties. When the pen moves to the right, θ_{B_a} increases, and the recessing angle (θ_{B_r}) decreases. As θ_{B_a} increases, the hydrostatic pressure on surface increases to reduce the ink flow. For low θ_{B_a}, the pressure difference is maximized, resulting in the high ink feed rate.

(**Figure 2.1**b) shows the printing setup consisting of an x-y-z plotter and control module. The printing direction is controlled by two step motors in x and y directions. Manual micropositioning stage sets the Z-coordinate (pen tip height; H) necessary to form a nano ink bridge. A camera with a microscopic objective lens monitors the condition of the liquid bridge for feedback control. The substrate temperature is controlled via closed-loop by a thermocouple as a sensor for a heating stage.

(**Figure 2.1**c) illustrates the printing procedure. First, the nib is pressed in the axial direction, and nano ink is released due to capillary action. Second, upon the release of the nano-ink, the pen is withdrawn from the substrate to H = 100 μm; nano ink bridge forms between the pen tip and the substrate. When the pen moves to the right, θ_{B_a} increases and θ_{B_r} decreased. Finally, the pen is retracted to stop the print. (**Figure 2.1**d) shows a typical example of the printed pattern using the nano ink-bridge printing on a polyethylene terephthalate (PET) film. A PET film is an appropriate substrate for chemical sensors because it is chemically resistant, transparent, and mechanically robust.

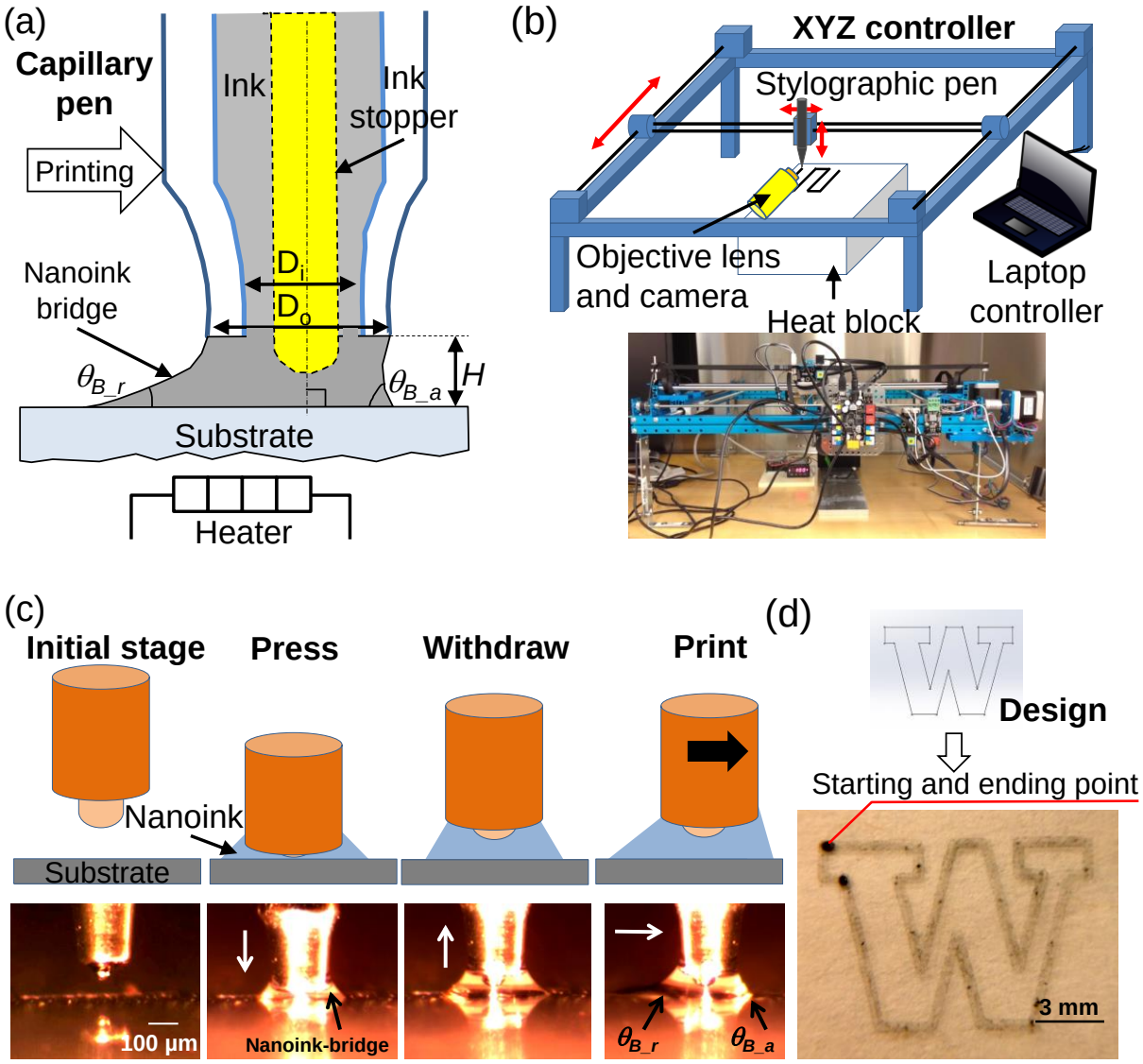

Figure 2.1. Nanoink bridge-induced capillary printing (a) Printing concept (b) Schematic of an XYZ plotter installed with a heating stage and a camera system. The top image shows a printing system, and the bottom is a photograph of the setup. (c) Nanoink-bridge induced printing using water ink on a PET film. The ink is released with pressing the stopper. Upon withdrawal by 100 μm, an ink bridge forms. The advancing contact angle increases as the pen moves from left to right. (d) W-pattern printed by SWCNT-ink at 80℃ at 1.2 mm/sec. The top image shows a design.

2.4 EXPERIMENTAL METHODS

2.4.1 *Characterization of the printing method*

To study the printing characteristics, a dot, a line and a film of SWCNTs were printed at various substrate temperatures and printing speeds. Nanoink was prepared by suspending SWCNTs (5 mg/mL) in 1 % sodium dodecyl sulfate (SDS) by sonication. In the suspension, the supernatant was used as nano-ink. The advancing contact angle (θ_{B_a}) on a PET film was measured for various substrate temperatures and printing speeds. The morphology of the printed patterns and the electrical properties were characterized. The nominal diameters of the capillary pens were 100, 300, and 700 μm. The outer diameters of the pen nib (D_o in **Figure 2.1**a) were 225, 375, and 790 μm, respectively (**Figure 2.2**). The outer diameters determined the minimum line width in printing as the meniscus attached to the outer dimension of the nib. In the paper, the nominal diameters are used hereafter.

Dot printing A single dot was printed at various substrate temperatures 20 ˚C, 40 ˚C, 60 ˚C, 80 ˚C, and 100 ˚C using a 300 μm-diameter pen. The pen reservoir was filled with SWCNT-ink and then installed on a printer. The pen was pressed and then withdrawn to H = 100 μm to form a nano ink bridge. To study the evaporation characteristics, the holding time was controlled at 1, 5, and 10 seconds at each temperature. The contact angles (θ_B) were measured for each case by using the camera images in the printer. The height profile of the dots was scanned by a profilometer (Alpha-step D-300 stylus profiler, KLA-Tencor Corporation).

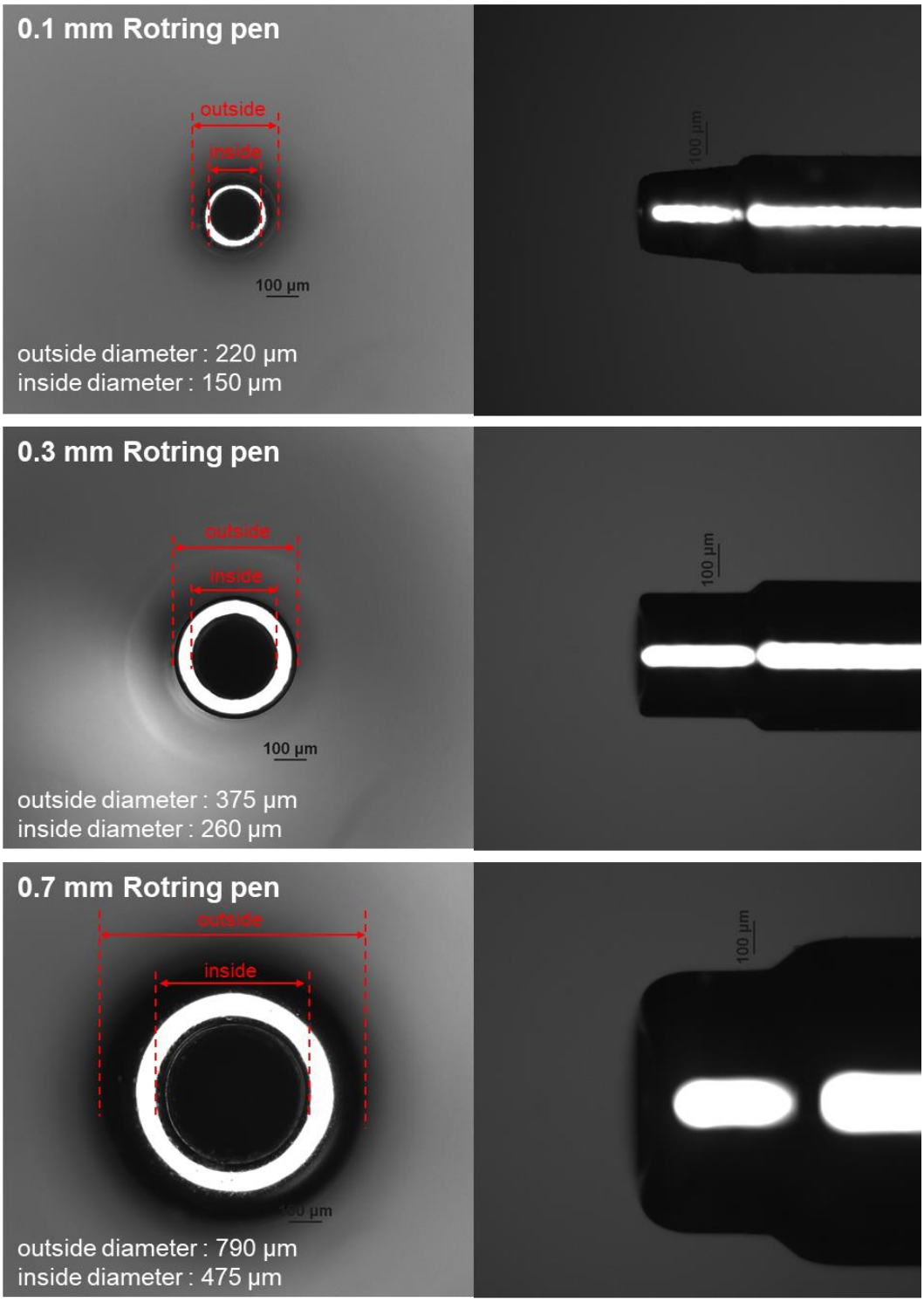

Figure 2.2. Diameters of the capillary pens. The nominal diameters of the capillary pens are 100, 300, and 700 µm. The outer diameters of the pen nib are 225, 375, and 790 µm, respectively.

Line printing To print a line, numerical control (G-code) was used to control x and y directional step motors. A 100 µm capillary pen was used. After the nano-ink bridge formed at a 100 µm gap, a straight line was deposited on a PET film. Printing speed was set in the range from 0.2 to 10 mm/s, and the temperature was controlled from 20 ℃ to 100 ℃. The line width and θ_{B_a} were measured for each speed and temperature. After printing, a silver paste was applied to both ends of the line to form electrodes. A picoammeter (6487 Picoammeter/Voltage Source, Keithley Instruments) was used to measure current-voltage (*I*-*V*) characteristics of the printed line. The printed line was imaged by an optical microscope (Olympus BX-41, Olympus, Gaithersburg, MD, USA) and scanning electron microscopy (SEM) in order to characterize the morphology of SWCNT lines.

Film printing Film printing was achieved by drawing continuous lines in linear hatch pattern covering the area of 15x15 mm^2. Printing speed was set for 2.5 mm/sec, and the substrate temperature was varied from 20 to 100℃. The nominal diameter of a capillary pen was 700 µm. To achieve complete coverage, the pen was shifted by 600µm for each pass (total of 25 parallel passes). Optical transparency measurements were performed by transmission optical microscopy (Olympus BX-41, Olympus, Gaithersburg, MD, USA). The transparency was computed as a ratio of the transmitted white light intensity through the printed area over the non-printed area. The sheet resistance was measured using a custom 4-point probe measurement system (**Figure 2.3**).

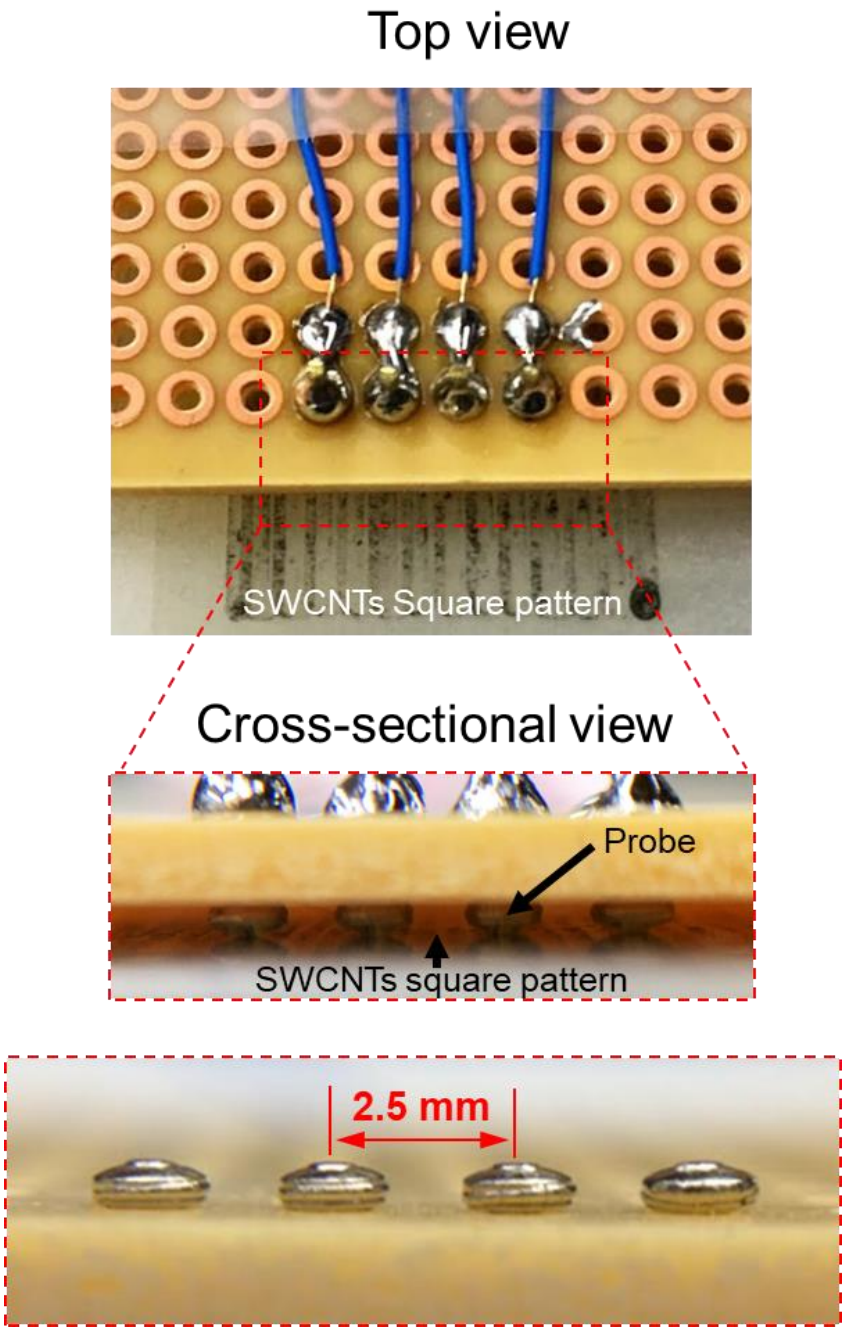

Figure 2.3. 4-point probe measurement setup. The sheet resistance is measured using a custom 4-point probe measurement system. The distance between electrodes is 2.5 mm.

2.4.2 *Doping effect*

The electrical characteristics of SWCNT lines were studied for doping polyethyleneimine (1 % PEI, Fluka). The printing sequence was varied for PEI and SWCNTs. In one case, SWCNT lines were printed first, followed by PEI deposition (SWCNT/PEI). In the other case, the order was reversed. The SWCNT lines were printed on top of PEI (PEI/SWCNT). The printing conditions were 80 ˚C with printing speed of 0.83 mm/sec where a stable line pattering could be obtained. Silver electrodes were patterned on the SWCNT lines. For both cases of SWCNT/PEI and PEI/SWCNT depositions, PEI solution (1 μL) was dispensed by 1, 2, and 3 times in order to analyze a doping effect and electrical stability. After each deposition, PEI was cured in a convection oven at 100 ˚C for 1 hour. *I-V* characteristics were measured for all cases.

2.5 RESULTS

2.5.1 *Characterization of the printing method*

Dot printing Dot printed patterns were analyzed to determine nano ink behavior at various temperatures and holding times. A circular dot printed patterns formed when a capillary pen was pressed and retracted to 100 μm on a PET film for 1, 5, and 10 seconds (**Figure 2.4**a). As the temperature increased, the ratio of the dot diameter to the outer nib diameter decreased and approached unity (**Figure 2.4**b). The dot size reduction was attributed to the increase of the

static contact angle (θ_{B_a}) and the pinning at the meniscus due to ink evaporation on the hot surface. As the substrate temperature increased, the surface tension and the viscosity decreased. However, the evaporation rate increased θ_{B_a} (**Figure 2.4**c). As θ_{B_a} approached 90°, the meniscus edge was pinned yielding the ratio of unity. As the substrate temperature increased, the drop spreading on the substrate was reduced, suggesting the effects of the increased evaporation rate at the drop edge.

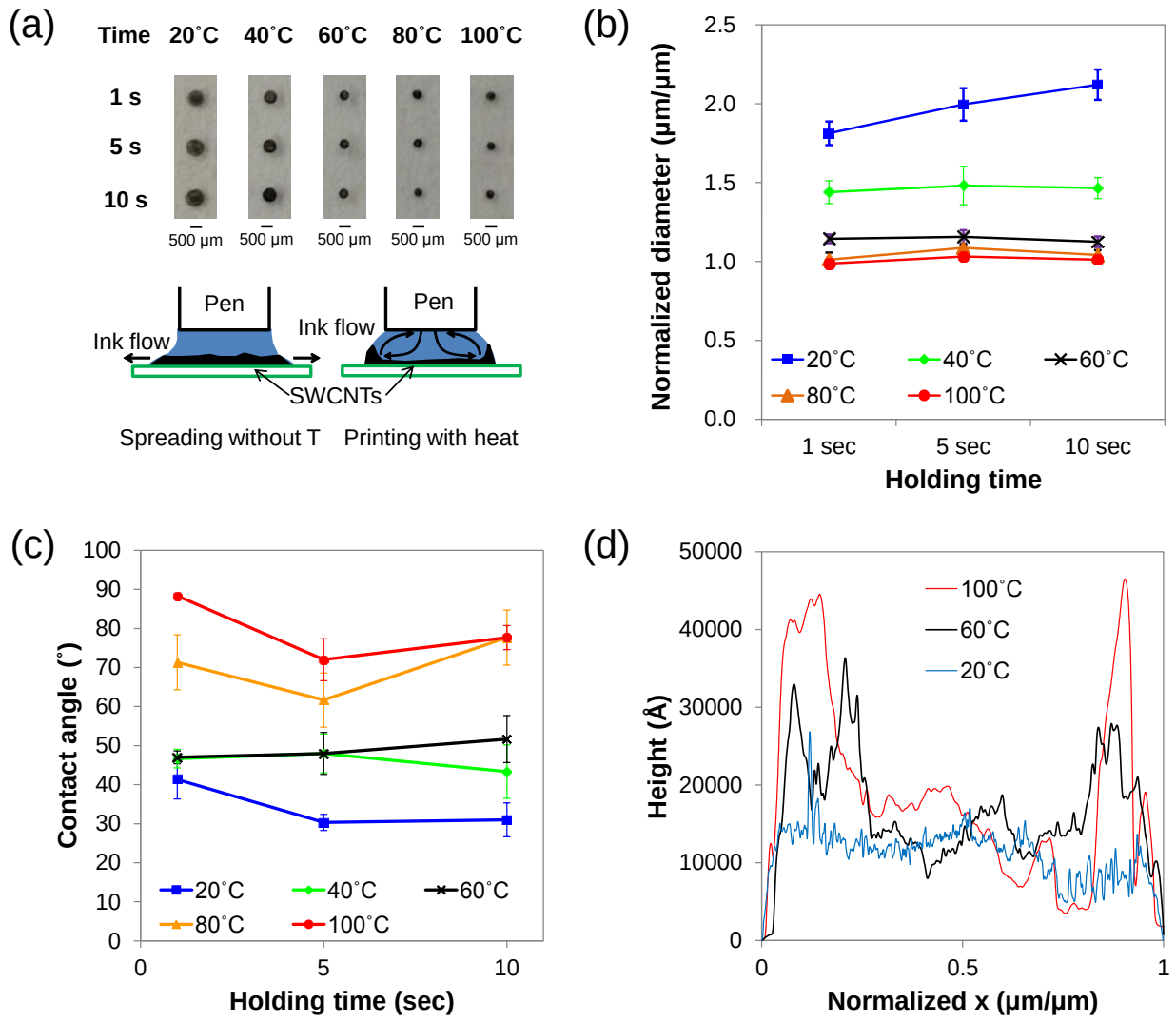

Figure 2.4. Dot printing (a) Dots printed at surface temperature 20~100℃ with holding time of 1, 5, and 10 s. Scale bar: 500μm (b) Dot diameters normalized by an outer nib diameter (c) Contact angles according to holding time (d) Dot profile at 20, 60, and 100℃ (1s holding time).

Profilometer measurements of the dot depositions show that a coffee-ring effect is present for a higher substrate temperature (**Figure 2.4**d). The greatest deposition height occurred for prints with the surface temperature of 100 ℃. During the deposition, SWCNTs were continuously delivered to the edge of the ink bridge where the liquid evaporation rate was the greatest, resulting in an increased local concentration of the SWCNTs in the solution, thus their thickest deposition at the dot edges. At room temperature, relatively uniform distribution of SWCNT ink was observed as the ink flow rate, and its deposition rate was balanced by the evaporation rate.

Line printing Microscopic observation of the printed line patterns shows that three distinct printing regions exist: (Region 1) print line width decreases with the increase of print speed in the low-temperature prints (20 and 40 ℃); (Region 2) line width is constant at medium temperature (60 and 80 ℃); (Region 3) line width increases with print speed – at high temperature (100 ℃) and lower speeds. The trend is due to changing fluid properties and θ_{B_a}.

(Region 1) was observed at the lower temperature conditions (20 and 40 ℃) and medium temperature (60 ℃) at higher print speeds; the line width reduced with the increase in print speed and the increase of the substrate temperature (**Figure 2.5**a and **2.5**b). At room temperature, the normalized line width, which is the ratio of the printed line width to the actual outside diameter of a Rotring pen, was reduced from 2.5 to 1 as the print speed increased from 0.2 to 2.5 mm/s. The nominal and actual diameters are given in the (**Figure 2.2**). At the low print speed, low contact angle, and low shear stress, the line width was not uniform, indicating the unstable behavior of the capillary bridge. As the print speed increased both shear stress and contact angle, the bridge was stabilized, resulting in the stable printing conditions exhibiting

constant line width and lower flow rate, which was also consistent with the increased sheet resistance. The reduction of the line width suggests that (i) the increased θ_{B_a} (**Figure 2.5**c) causes the increase in the contact angle on the sides of the droplet to parallel to the nib motion due to the surface tension, (ii) capillary bridge elongated along the printing direction with the shear stress. For the lower temperature condition, the prints failed at the speeds > 2.5 mm/s, as θ_{B_a} approaches 90°.

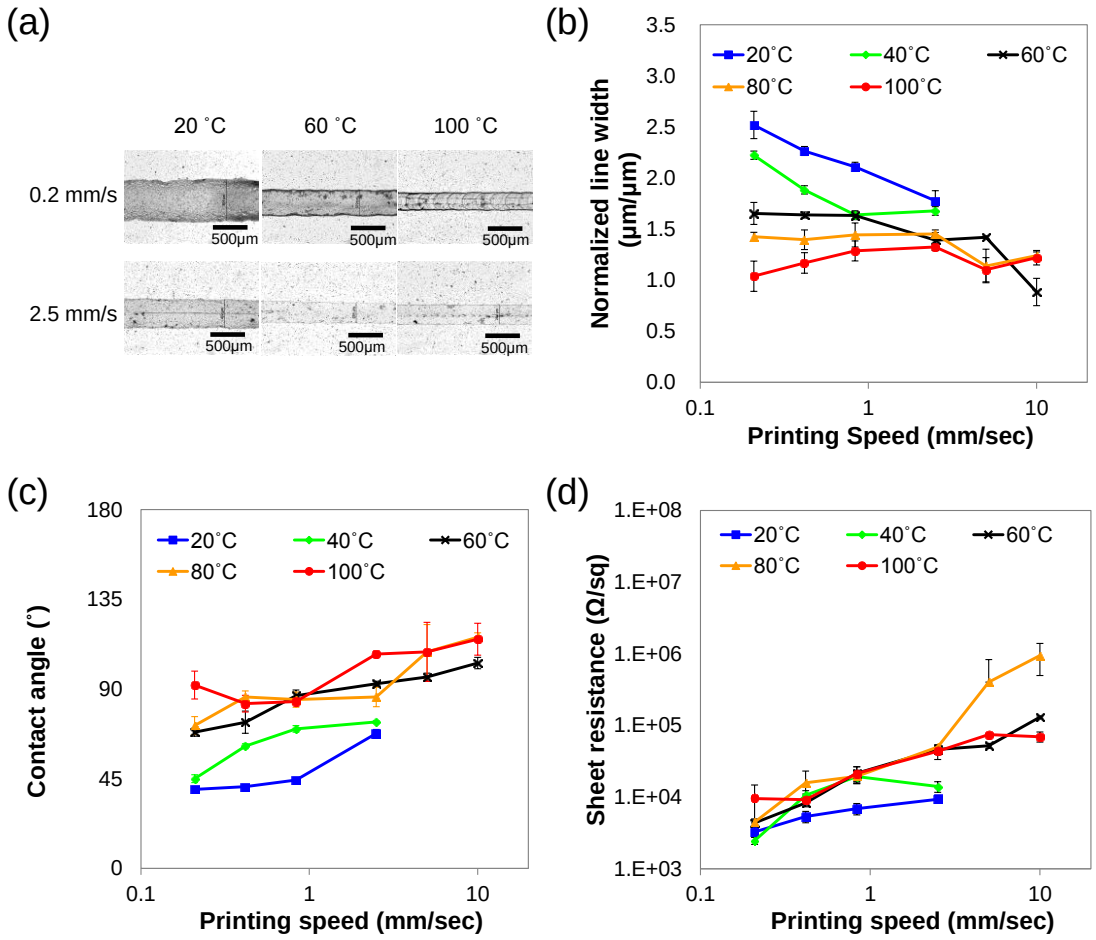

Figure 2.5. Line printing (a) Printed lines at 0.2 and 2.5 mm/s under the substrate temperature of 20~100 ℃. (b) Normalized line widths at a temperature of 20~100 ℃ with a printing speed of 0.2~10mm. (c) Advancing contact angle (θ_{B_a}) at various printing speed. (d) Sheet resistance according to print temperature and speed.

(Region 2) was characterized by relatively constant line width independent of the print speed at 60 and 80 ℃. At the higher temperatures, the ink viscosity reduced, resulting in the lower local shear stress allowing the ink to flow more uniformly at the larger contact angle. Experimentally the print speed increasing from 2.5 mm/s to 10 mm/s did not compromise the bridge stability though the advancing angle exceeded 90 ° for the faster prints. The high θ_{B_a} resulted in the high and stable contact angles on both sides of the bridge.

(Region 3) was characterized by the increase in the line width as print speed increased at T=100 ℃ and print speed below 2.5 mm/s. It is speculated that the effect was caused by the high rate of ink evaporation at the low print speeds as the liquid in the bridge approached its boiling point. As the speed increased, the time allowed for evaporation reduced. The ink was delivered to the substrate more effectively resulting in a wider print line. At the higher speeds (>2.5 mm/s), the normalized line width reduced, which was consistent with the increase of θ_{B_a} as shown in (**Figure 2.5**c).

Related to the optimization of the print conditions: at the temperatures greater than 60 ℃, SWCNTs could be printed as $\theta_{B\_a} > 90°$. At the temperature of 80 and 100 ℃, a stick-slip effect was observed at the advancing meniscus of a nano ink bridge. The beach mark pattern in (**Figure 2.5**a) and an SEM study were consistent with the stick-slip effect (**Figure 2.6**). Similar to the dot printing, the printed lines showed a coffee-ring effect at the temperature > 60 ℃ while a flat profile was observed at the temperature < 60 ℃. The thickness of the printed line was well below 1 μm, which could not be measured by a profilometer or an atomic force microscope (AFM) because of the relatively rough PET surface. The formation of the coffee ring could be observed by the higher contrast in an optical microscope and SEM (**Figure 2.6**).

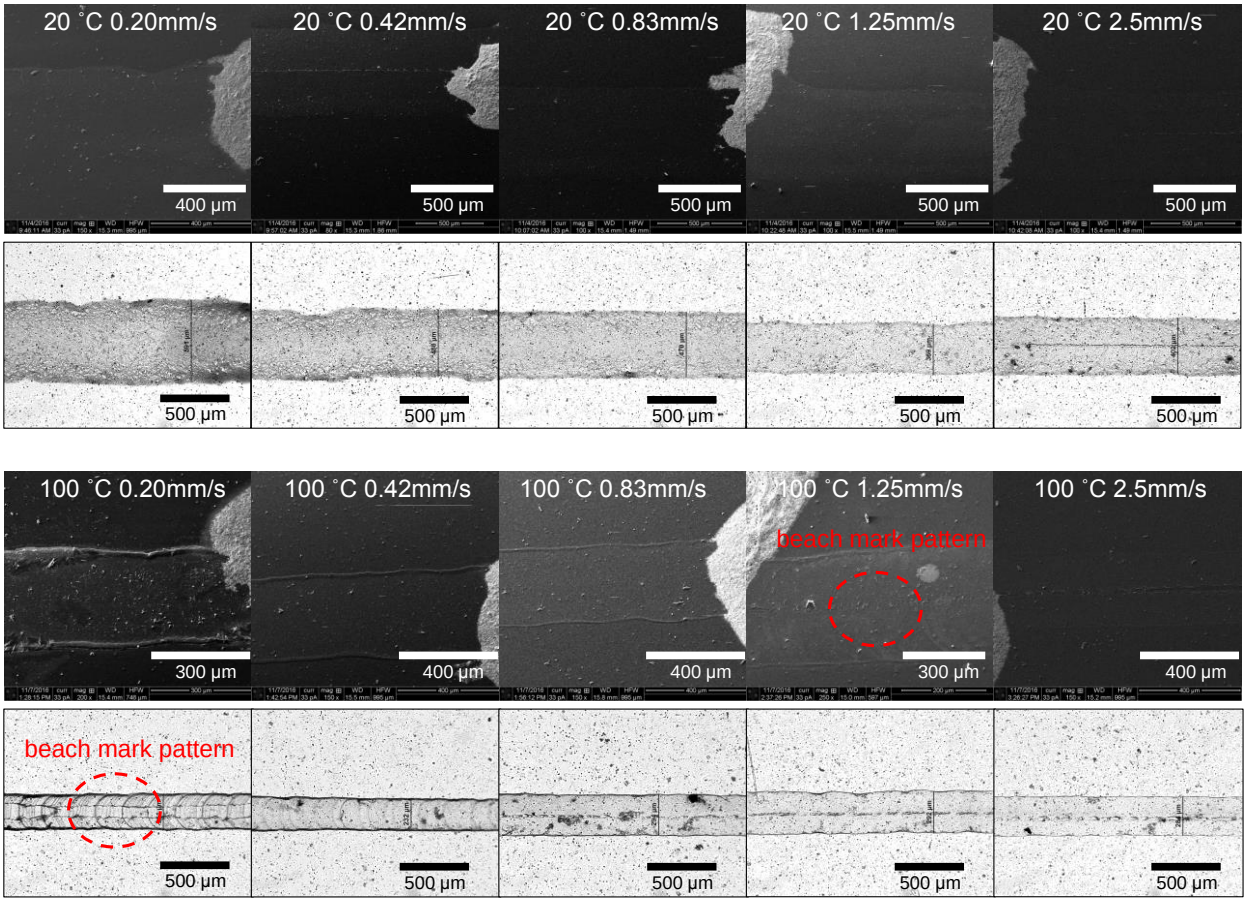

Figure 2.6. Printed SWCNT lines at 20 and 100 ℃. Top rows are SEM images, and bottom rows are optical microscope images for 20 and 100 °C, respectively. The beach-mark pattern is observed at 100℃ due to a stick and slip effect. The two lines at the edge of an SWCNT line at 100℃ A form by a coffee ring effect.

For electrical characterization of the prints, a silver electrode was patterned at the ends of a printed line. In comparison to 4-point probe measurement, the contact resistance using the 2-silver electrodes was only 9.6 ± 0.6 %, which was consistent throughout multiple measurements (N = 6). The *I-V* characteristics showed a linear trend due to the metallic SWCNTs in the printed lines. The sheet resistance of the lines became larger as both temperature and speed became higher (**Figure 2.5**d). With the increase of θ_{B_a}, the smaller pressure difference reduced the flow rate of SWCNT ink, which increased the sheet resistance.

Overall, the increase in the print speed yielded the greater sheet resistance as a result of the higher contact angle and reduced flow rate. At the higher speed, the contact angle increased the pressure on the substrate, which resulted in the smaller nano ink flow rate thus the reduction of SWCNTs deposition and greater transparency of the print (**Figure 2.7**). Unlike in the inkjet printing, both desired transparency and electrical resistance could be obtained with a single print, which shows the advantage of the nano-ink bridge induced capillary printing.

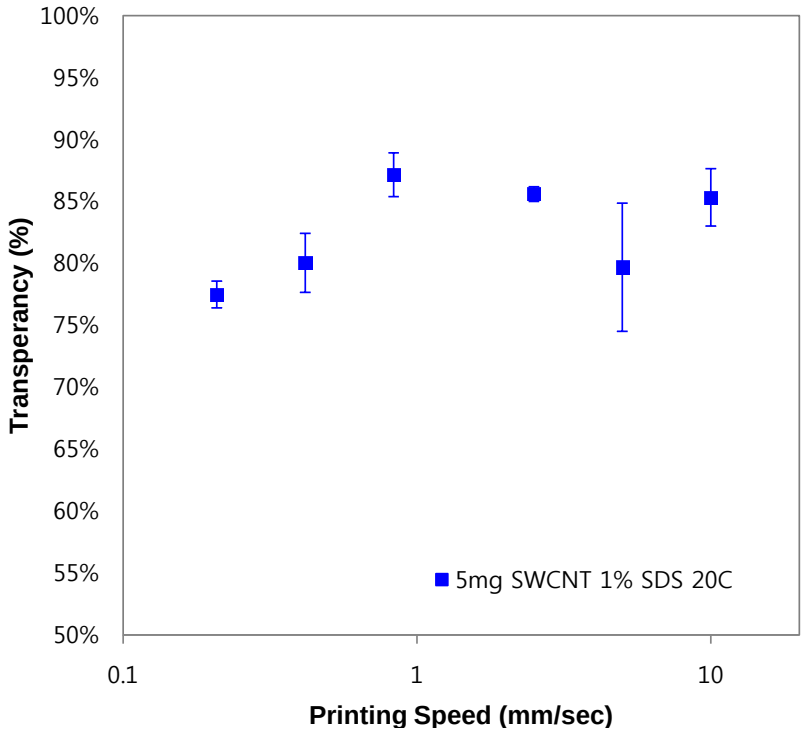

Figure 2.7. Transparency for an SWCNT line according to various printing speed at 20℃.

Film printing For film printing, the area of 15x15 mm^2 was printed in 3 minutes with the nib speed of 2.5 mm/sec. When the printing lines were overlapped at T = 20℃, the nano-ink was smudged across the printed lines. The optical transparency of the film increased from 67 % to 89 % as the temperature increased (**Figure 2.8**a). For print temperatures > 60 ℃, SWCNT clusters were observed; during printing, the SWCNTs were aggregated at the stopper, leaving clusters on the substrate. The sheet resistance increased from 2.5 to 62.4 kΩ/sq as the temperature increased (**Figure 2.8**b), due to the larger bridge contact angles and thus, the reduced ink flow rate. The sheet resistance was the highest at 80 ℃ and reduced at 100 ℃, consistent with line printing observations.

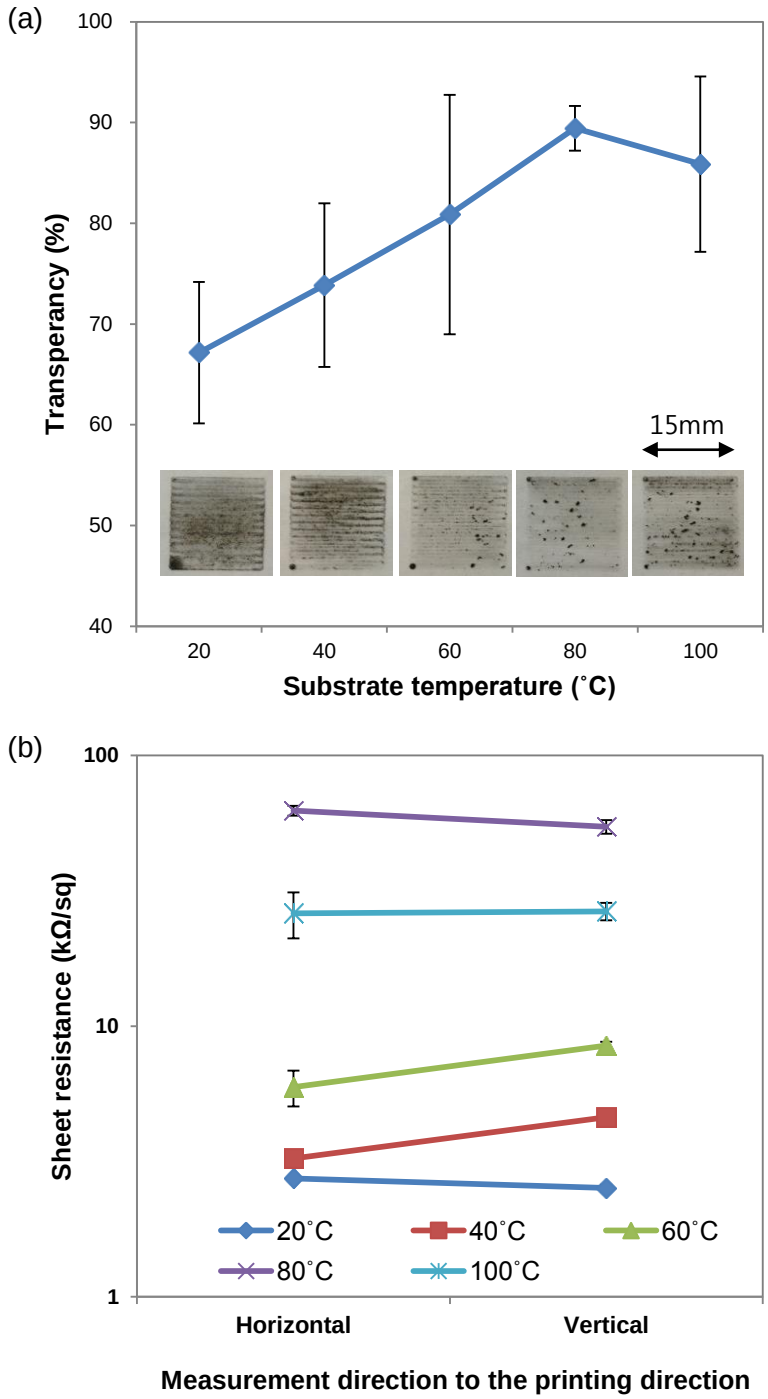

Figure 2.8. (a) Transparency of printed films at temperatures of 20~100℃. Printing speed: 1 mm/s (b) Sheet resistance in the printing and its vertical directions.

2.5.2 *Doping effect*

The doping effect of SWCNTs was studied by using PEI. PEI was deposited before or after SWCNT printing. For SWCNT/PEI lines, the current decreased as the number of PEI deposition layers increased (**Figure 2.9**a) based on *I*-*V* characterization (inset Figure of **Figure 2.9**a). For the repeated tests (N = 3), the error bars for the electric current showed ± 9.5, ± 6.8, ± 5.3, ± 1.6 % for 0, 1, 2, and 3 depositions. With more depositions, the error bars were reduced because semiconducting SWCNTs with various chirality reached current saturation by the doping. Considering the initial p-type SWCNTs, the current decreased due to the PEI' amine group doping. For measurement over 1000 s, the resistance change was only ± 0.09 %, showing layer stability (**Figure 2.9**b).

For PEI/SWCNT lines, the doping effect was not as reproducible as the SWCNT/PEI lines (**Figure 2.9**c): the SWCNTs might not be fully covered with PEI. The resistance could increase or decrease for forward and backward printing directions (**Figure 2.9**d). The large change in the resistance appeared to be related to the physisorption and reaction with air. When the SWCNT device was placed in a vacuum chamber (125 mmHg), the resistance was constant because of the low oxygen environment (**Figure 2.9**d). (**Figure 2.9**c and **2.9**d) suggest that the *I*-*V* nonlinearity resulted from the continuous change of PEI/SWCNT resistance due to the interaction with air.

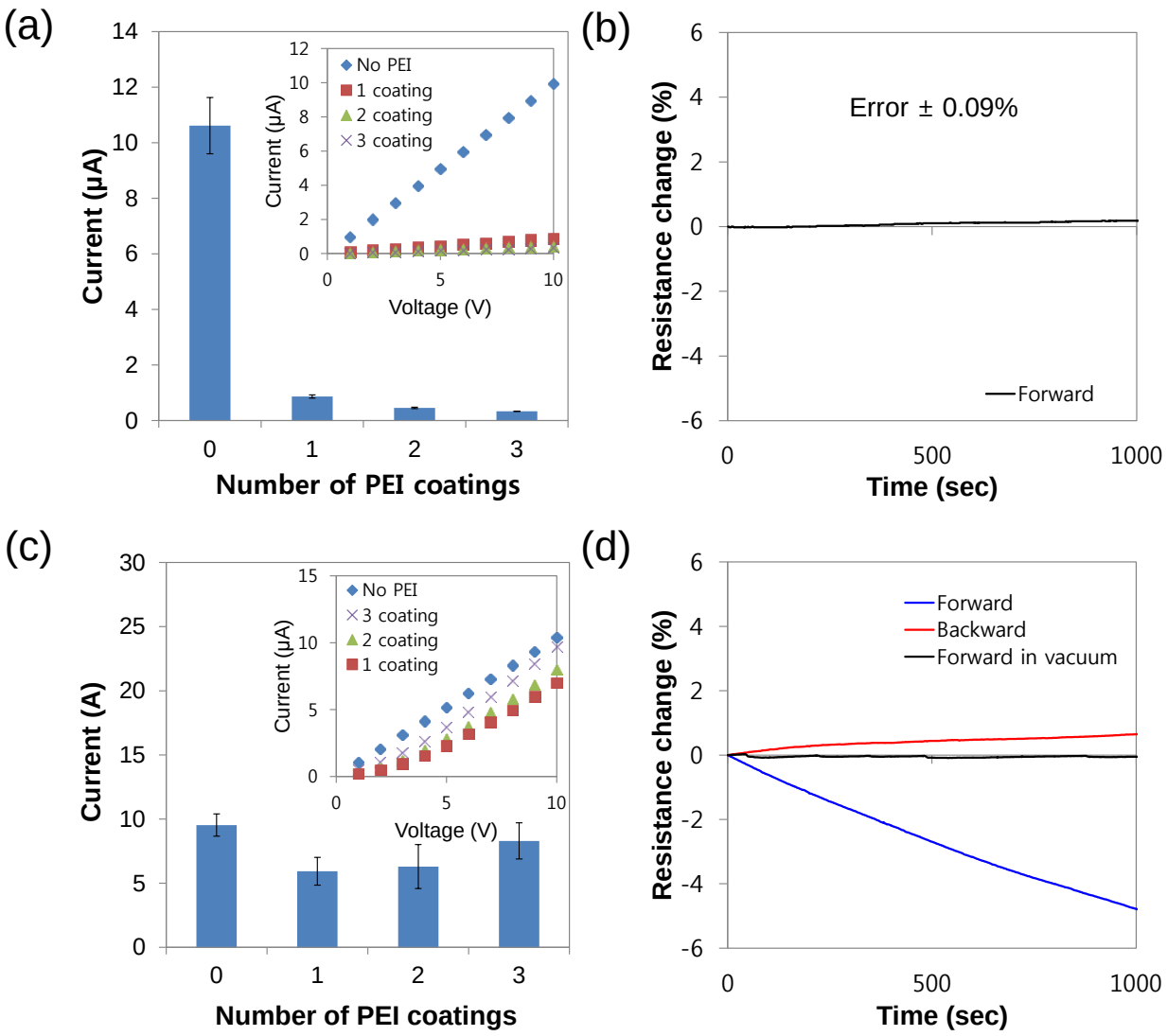

Figure 2.9. Resistance change for SWCNT/PEI and PEI/SWCNT lines (a) Current change at 10 V for 1, 2, and 3-PEI depositions. (b) Resistance change for an SWCNT/PEI line. (c) *I-V* characteristics of PEI/SWCNT lines for 1, 2, and 3-PEI depositions. (d) The resistance change of an SWCNT device for forward and backward printing directions in the air and forward direction in a vacuum (125 mmHg).

2.6 DISCUSSION

Due to the non-contact nature of the bridge-induced printing, the SWCNTs could be deposited without damaging substrate surface. The contact mode printing with the same capillary pen resulted in scratch marks on the substrate. The print line width was determined by the pen's outside diameter and the contact angle. For the examined ink formulation and substrate type, the contact angle was a function of substrate temperature and print speed. The smallest line width was obtained at θ_{B_a} ~90 ° and was equal to the outside diameter of a pen nib. According to our characterization, PEI solution with known surface tension coefficient and viscosity showed that the line width was determined by solution viscosity at low speed (**Figure 2.10**). As the speed increased, the line width was determined by the contact angle and Capillary number. Since the flow rate decreased with the higher contact angle, the resulting sheet resistance increased at the lower flow rate. For example, using the smallest ink drop radius (110 μm) and water surface tension coefficient (0.073 N.m), the pressure difference (ΔP) at the substrate surface could range from 0 to 1.3 kPa. At room temperature, ΔP was close to 0 kPa due to the spreading of nano ink, which increased to 1.3 kPa at θ_{B_a} = 90 °. Considering that the working principle yields a very low-pressure gradient in the system, the noncontact nano ink-bridge induced printing method can be beneficial for printing water-based molecular ink.

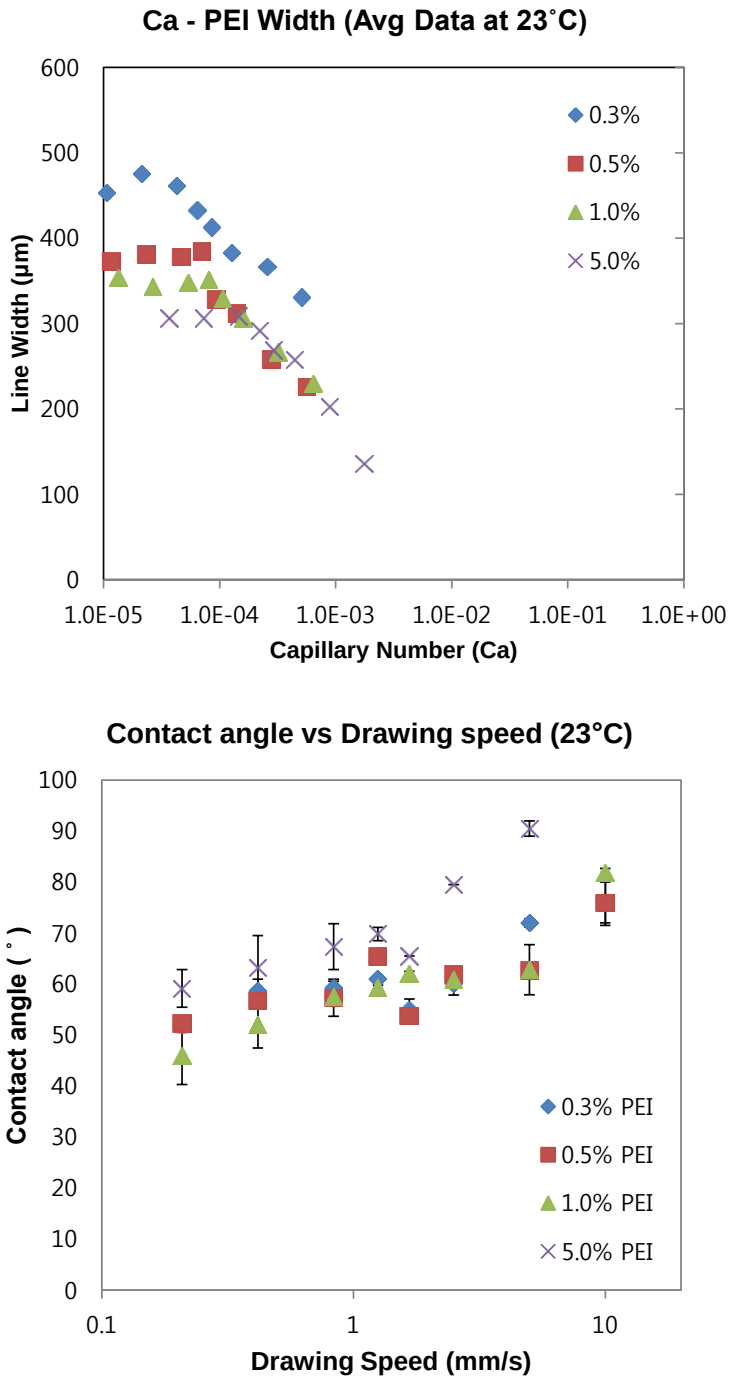

Figure 2.10. Line width for various concentrations of PEI diluted in deionized water.

2.7 CONCLUSION

In summary, the noncontact capillary pen printing method was developed for the fabrication of SWCNT sensors. Using a custom printer, the patterns of a dot, a line, and a film were printed and characterized in the contexts of morphology, electrical properties, and optical transparency. During the printing process, the contact angle was measured and related to the substrate temperatures and printing speeds. For a dot printing, a coffee ring effect was clearly shown for high-temperature substrate due to the rapid evaporation and the pinning effect in the ink bridge. The contact angle gradually decreased at room temperature, which formed a relatively uniform height of an SWCNT dot. For a line printing, the advancing contact increased as the substrate temperature, and the print speed increased. For these conditions, the higher pressure at the substrate reduced the ink flow rate increasing the sheet resistance and the optical transparency of the SWCNT line. For print uniformity, optimal printing temperatures are in the 60~80 ℃ range. A film could be printed to obtain an average sheet resistance of 7.2 kΩ/sq by a single printing at 60 ℃. To obtain consistently high-quality prints, the advancing contact angle needs to be monitored. The nano ink bridge-induced printing allows for printing complex sensor geometries without damage of previous layers. The non-contact printing approach facilitates printing of large array sensors at low cost for wearable and film-type platforms.

Chapter 3. FABRICATION AND CHARACTERIZATION OF CHEMICAL SENSORS

3.1 INTRODUCTION

The significance of monitoring gaseous pollutants spans multiple areas vital to the environment and human health. The use of flexible and low-cost sensors in many applications has significant advantages over more expensive gas analyzers. These advantages are useful to sensor networks, where the area sample has to be taken at multiple locations, and personal exposure monitors, where the assessment of the exposure needs to be characterized from the prospective of the moving subject. Recent literature shows that exposure to gaseous pollutants can trigger diseases, including asthma and cardiovascular disease [87-89] and significant lung inflammation [90-96]. Various sensors have been developed in the last few decades, such as electrochemical detection, semiconductors, photoionization (PID), catalytic detection, and infrared detection. For individual use, lightweight gas sensors are fabricated by using field effect transistors (FETs). Heating to a few hundred degrees can improve the low sensitivity, but heating requires significant power (>100 mW). Typical sensitivity is at a sub-ppm level with limited specificity. Therefore, a portable and high-performance gas sensor is an urgent need for the assessment of individual exposure to toxic gases.

Recent advances in nanomaterial research have resulted in the development of novel sensor platforms [97-102]. Among nanomaterial gas sensors, carbon-based materials, including amorphous carbon, carbon nanotubes (CNTs), and graphene sheets, were very popular due to their well-developed synthesis methods and well-characterized detection mechanisms [103-106].

In comparison to graphene, SWCNTs show a higher sensitivity because their effective density of states around the Fermi level is lower than that of graphene [107]. The rolled structure of SWCNTs provides greater edge effects than that of the planar structure of graphene, which contributes to the superior sensing performance of SWCNTs. Since the first discovery of a CNT gas sensor [108], sensors for the detection of various gas molecules were developed (e.g., NO_2 [109] and NH_3 [110]). To enhance sensitivity, the CNT matrix needs to have high density with controlled doping levels of SWCNTs. To enhance specificity, an array of sensors can be used to mimic an olfactory system response [111], and a specific target can be identified by mapping the response of the array.

Further, an array of 32 SWCNT sensors were integrated into a silicon chip, which could identify NO_2 from humidity and chlorine [112]. However, the fabrication process (specifically, the precise functionalization of the SWCNTs) is challenging when micromachining is used. Simple dropping and drying of dopants on SWCNTs do not offer reliability in sensor fabrication or reproducibility in performance.

To overcome the drawbacks of micromachining-based processes, various bottom-up methods were developed. Early methods relied on direct growth using self-assembly aided by electric or magnetic fields [83, 84]. In order to print multiple layers of nanomaterials, various approaches have been investigated. Among them, non-contact printing is preferred to avoid potential damage to the substrate or the previously-printed layers. Inkjet-style printing [60-62] is the most common method of various commercially available techniques. Thermal and piezoelectric inkjet printing use thermal expansion or electromechanical vibration to eject droplets, overcoming surface tension in the formation of droplets [60, 63]. Due to the physics of droplet formation, inkjet printing is limited to the range of viscosities and values of surface

tension of the working fluid [64, 65]. When the nano-ink of interest has high surface tension and low viscosity, cumbersome change of ink properties is performed to generate a stable droplet [32, 66, 67]. In addition, CNTs could be easily clogged in the nozzle, and repeated writing is required to connect the printed dots. Polymer doping on SWCNTs was another challenge because of the discontinuous pattern. Microcontact printing was capable of patterning CNTs, but defects could be generated due to the nonuniform contact [113]. Fountain pens [76-78], ball pens [79], and pencils [80, 81] have been demonstrated in nanomaterials printing. However, these contact printing methods could induce damage to the substrate [78], which impeded the printing of multiple layers or large scales. A pencil made of carbon nanotubes could be used, but the substrate was limited to paper with a lack of doping capabilities [81].

In summary, despite the great potential of SWCNTs for the sensitive and selective sensing of gas molecules, current micromachining and printing methods do not meet the controlled doping and reliable printing needs to be required for SWCNTs. A reliable printing method is crucial for the development of a sensor array with enhanced sensitivity and specificity. Such challenges have limited the use of SWCNT sensors to resistive sensing mechanisms. SWCNTs have not been demonstrated for capacitive and inverter gas sensor use. To address these challenges, we will use a noncontact capillary pen to integrate SWCNT-based capacitance, resistance, and inverter sensors into a sensor array. Density functional theory-based computation will elucidate the sensing mechanisms in order to enhance the detection limit for various target gas molecules.

3.2 OBJECTIVES

Using the developed printing method in Chapter 2, a continuous SWCNT line will be patterned for SWCNT sensors. Polymers as activation material will be aligned and printed on the SWCNT line for doping. Using liquid bridge, PEI and nafion will be deposited without damaging previous patterned SWCNTs line. Ammonia and NO_x gas are tested.

For pH sensor, two silver electrodes are stamped first, and then one of them is changed to AgCl as a reference electrode by electrolysis. The pH sensor performance will be characterized.

3.3 SENSOR FABRICATION

Gas sensor To fabricate a gas sensor, SWCNT electrode was printed as a line using a 300μm-diameter pen (**Figure 3.1**a). The substrate temperature was held at 80 ˚C, and printing speed was 0.83 mm/s. Silver ink was deposited on both ends of the SWCNTs for electrical connection. The SWCNT electrode was functionalized by depositing 1 μl drop of 1 % PEI, which was cured for 1 hr at 100 ˚C in a convection oven. A second SWCNT electrode was coated with 1 μl drop of 1 % Nafion (Nafion 117 solution, Sigma-Aldrich Co, LLC.) and cured for 1 hr at 120 ˚C in a convection oven. Both sensors were

exposed to two different concentrations of NO_2 (8 and 22 ppm). The sensors' resistance was measured and recorded by a multimeter (287 True RMS Multimeter, Fluke Corporation).

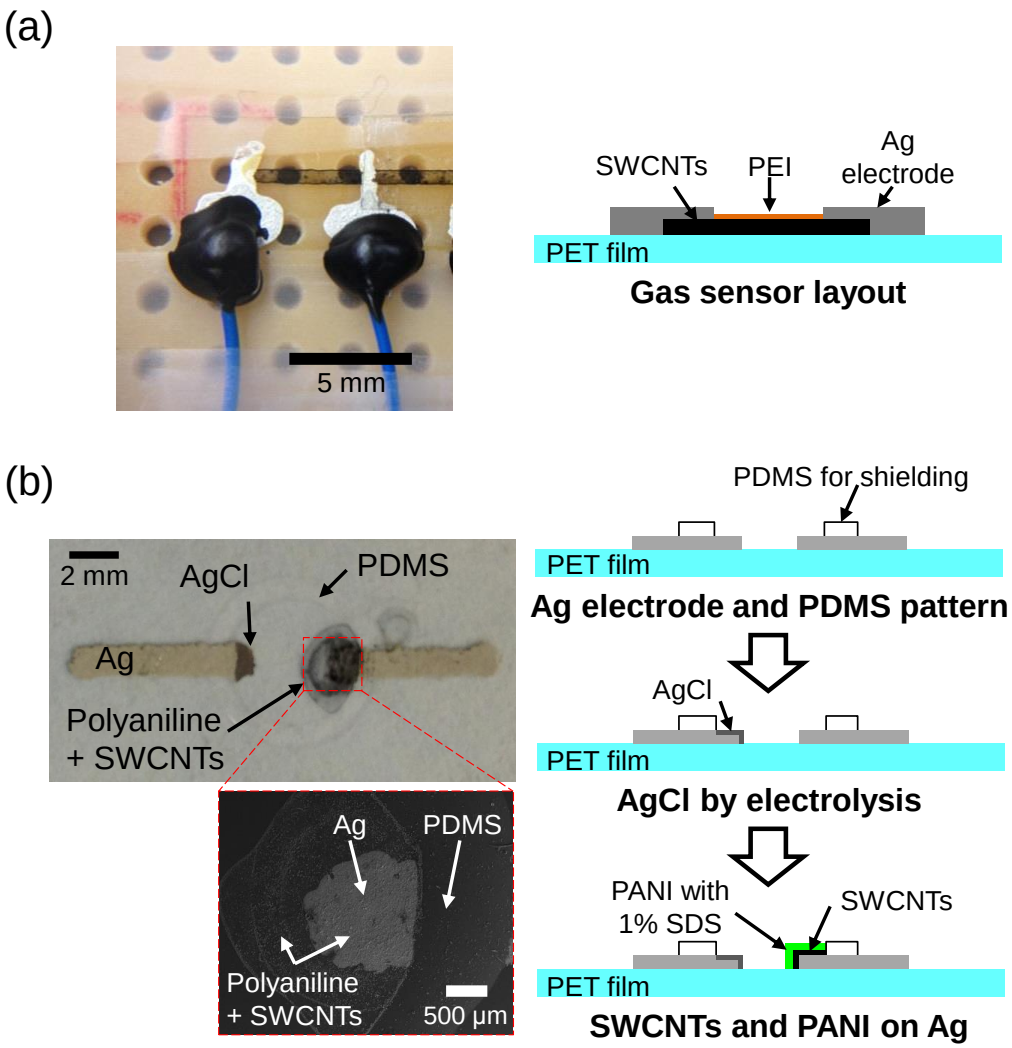

Figure 3.1. Fabrication steps (a) Images and cross-section of an SWCNT-gas sensor (b) Optical and SEM images and fabrication steps of an SWCNT-pH sensor.

pH sensor Silver electrodes were screen-printed on PET film (**Figure 3.1**b and **3.2**), which was cured at 100 ˚C for 10 min. Polydimethylsiloxane (PDMS; Sylgard 184

silicone elastomer, Dow Corning Corporation) was stamped in a ring shape to hold analyte solution inside the ring. The PDMS was cured at 75 ˚C for 1 hour in a convection oven. One of the silver electrodes (cathode) was modified to form an AgCl layer by electrolysis (1.5 V_{dc} for 1 minute in 1 M HCl solution). The other electrode (anode) was printed with SWCNTs**.** The SWCNT (5 mg/ml) solution was deposited via capillary bridge printing using a 300 µm-diameter pen that covered the entire silver electrode surface. The SWCNT printed electrode was cured for 10 min on a 100 ˚C hotplate. Polyaniline (5 mg/mL; PANI; emeraldine salt, Sigma-Aldrich Co, LLC.) suspended in 1 % SDS was deposited on top of the SWCNT electrode using two 1µL drops, followed by curing at 120 ˚C for 1 hour. The voltage between the AgCl electrode and PANI electrode was measured using an Arduino circuit for standard pH solutions of pH 4, 7, and 10 (Omega Engineering, Inc.). Since the circuit measured the voltage difference ranging 0~3 V, a 1.61 V AA battery was serially connected to shift the voltage potential above 0 V in the control pH ranges (pH 7~10).

3.4 EXPERIMENTAL RESULTS

Gas sensor The section aims to characterize an SWCNT gas sensor. When SWCNTs were doped with PEI and nafion, the sensor showed selectivity due to electrostatic interaction. PEI doped SWCNTs could selectively detect NO_2 while nafion doped SWCNTs could selectively detect NH_3.

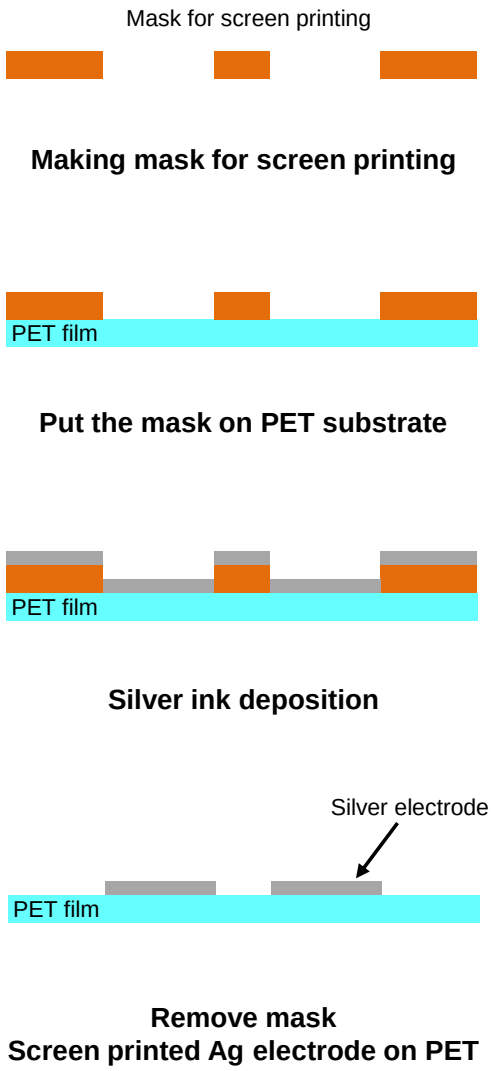

Figure 3.2. Silver electrode patterning. Sensor electrodes for a pH sensor are screen-printed to form silver electrodes on a PET film. The mask material for screen printing is PET film

The non-contact printing technique was used for fabrication of a gas sensor. To achieve uniform resistance, PEI was coated on an SWCNT line. The SWCNT sensor doped with PEI showed a response to NO_2 gas (**Figure 3.3**a). Nafion-doped SWCNTs showed a negligible change when exposed to NO_2 gas (**Figure 3.3**b) but had a significant response to ammonia (**Figure 3.4**). The specificity of the SWCNT-sensors to NO_2 and ammonia gases were consistent with the previous report [110]. However, the response

trends were opposite from the reported trends using n-type SWCNTs. The doping can change the sensitivity and selectivity of an SWCNT sensor [114]. For example, a positively charged dopant makes an SWCNT sensor sensitive to negatively charged gas molecules but insensitive to positively charged gas molecules. Without doping, an SWCNT sensor is also sensitive to gas molecules regardless of the electric charge of gas molecules. Note that our results were from SWCNTs printed on a PET film while the previous report used semiconducting SWCNTs grown on the micromachined electrodes.

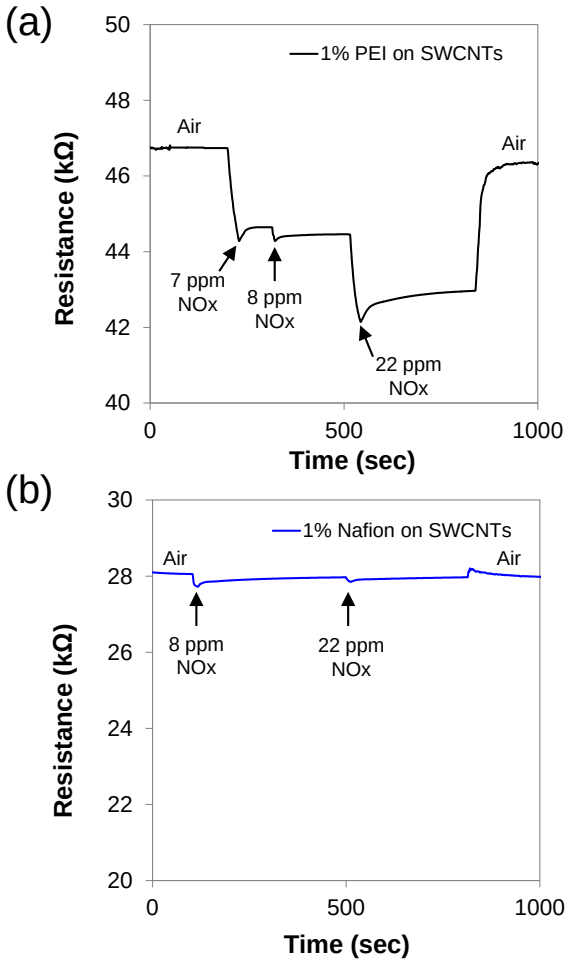

Figure 3.3. Gas response test (a) Change of PEI-doped SWCNT resistance for NOx gas, (b) Change of Nafion-doped SWCNT resistance for NOx gas.

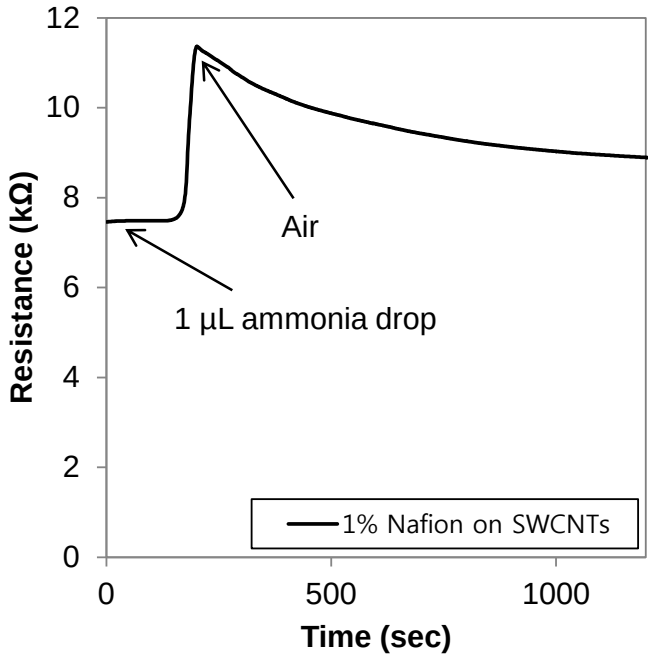

Figure 3.4. Change of Nafion-doped SWCNT resistance for ammonia gas. Nafion can differentiate between NOx and Ammonia with high accuracy, showing specificity.

For ammonia detection, SWCNT sensors with and without Nafion doping were prepared. A commercial sensor was also prepared to calibrate the concentration of ammonia. The ammonia concentration was changed from 1 to 20, 120, and 2580 ppb, the resistances of the SWCNT sensors increased (**Figure 3.5**a). At 1 ppb, the resistance did not change. As the ammonia concentration increased, the resistance increased with different sensitivity for the SWCNT sensors with and without Nafion doping. The commercial sensor showed a response from 120 ppb to 2580 ppb, which showed lower sensitivity than the SWCNT sensors. Since the sulfonic group in Nafion was negative, the Nafion-doped sensor was sensitive to ammonia but did not show the response to NO_2. (**Figure 3.5**b) shows the sensitivity of the SWCNT sensors to ammonia. Considering the electrical noise level, the detection limit is between 5 and 10 ppb.

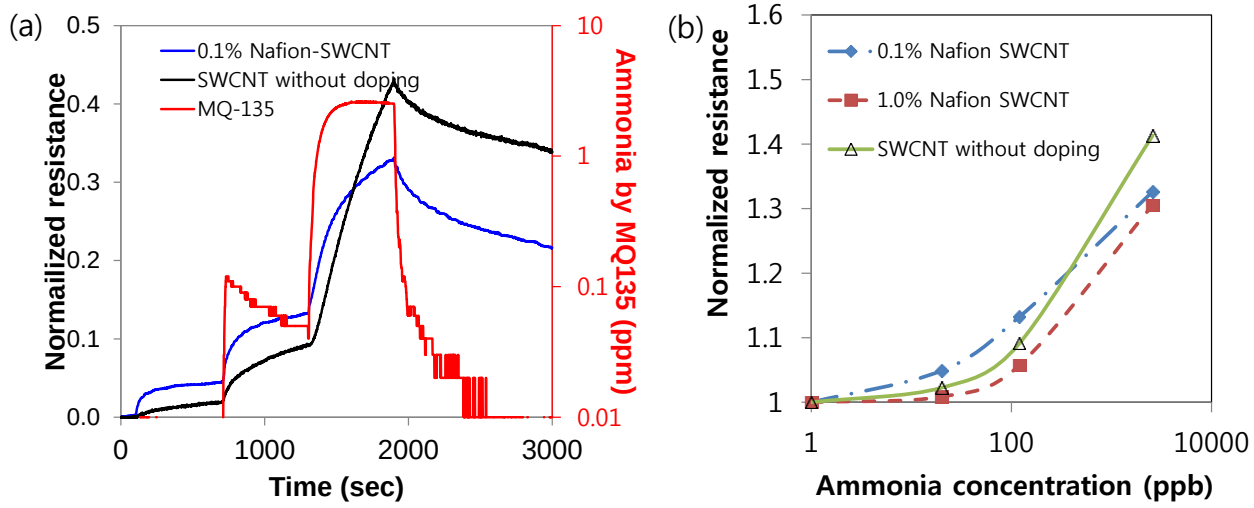

Figure 3.5. (a) Response of 0.1% Nafion-doped SWCNT, non-doped SWCNT and MQ-135(commercial) sensors for ammonia concentrations of 1, 20, 120 and 2,580 ppb. (b) The sensitivity of SWCNT sensors with 0.1% Nafion and 1% Nafion doping and without doping. Normalized resistance change vs. ammonia concentrations.

pH sensor The section aims to characterize an SWCNT-pH sensor. The sensitivity showed 61 mV/pH. A pH sensor was fabricated using silver electrodes (**Figure 3.6**). As for the fabrication, silver electrodes were stamped on a PET film. One of the silver electrodes (cathode) was modified to form an AgCl layer by electrolysis (1.5 V dc for 1 minute in 1M HCl solution). The other electrode (anode) was printed with single-wall CNTs (SWCNTs) using the capillary pen printing method. The SWCNTs were sensitive to pH and enhance electron transfer on the electrode surface. The SWCNT solution (5 mg/ml) was deposited via capillary bridge printing using a 300 μm-diameter pen that covered the entire silver electrode surface. The SWCNT printed electrode was cured for 10 min on a 100 ˚C hotplate. Polyaniline (5 mg/mL; PANI;

emeraldine salt, Sigma-Aldrich Co, LLC.) suspended in 1 % SDS was deposited on top of the SWCNT electrode using two 1 µL drops, followed by curing at 120 ˚C for 1 hour.

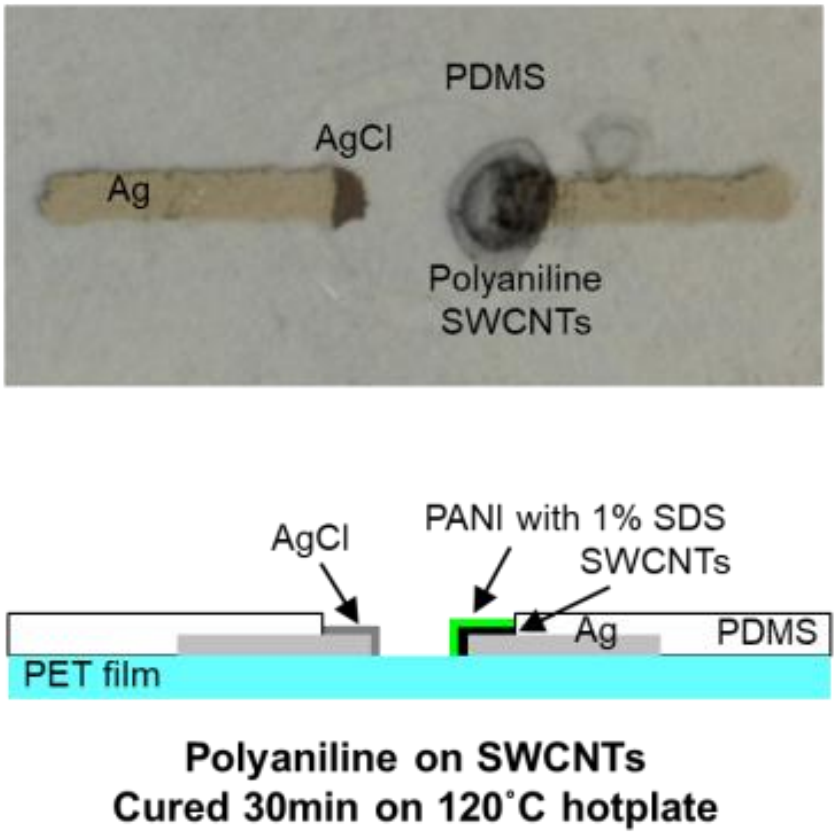

Figure 3.6. Fabricated pH sensor

The voltage between the AgCl electrode and PANI electrode was measured using an Arduino circuit for standard pH solutions of pH 4, 7, and 10 (Omega Engineering, Inc.) (**Figure 3.7**a). Since the circuit measured the voltage difference ranging 0~5 V, a 1.61 V AA battery was serially connected to shift the voltage potential above 0 V in the control pH ranges (pH 4~10).

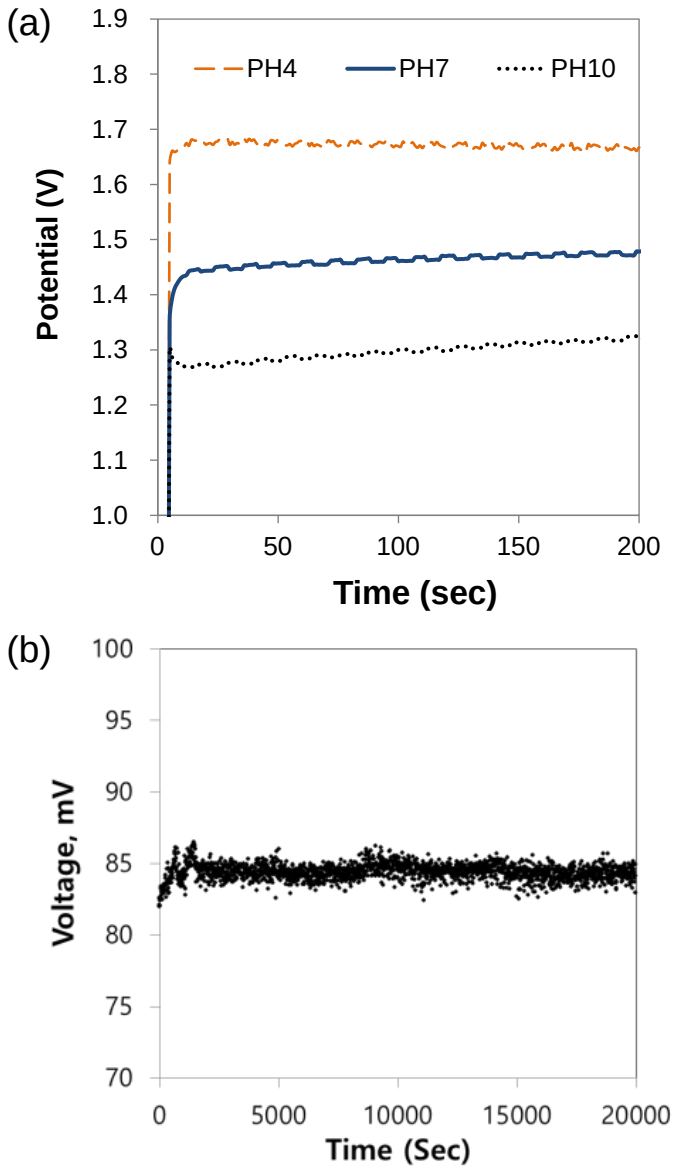

Figure 3.7. (a) Voltage measured for a pH sensor using standard solutions of pH 4, 7, and 10. Note that the voltage is shifted by using a 1.61 V-AA battery. (b) Stability of a pH sensor for 20,000 seconds

When the solution drops of pH = 4, 7, and 10 were sequentially interrogated using the fabricated sensor, the potential decreased as pH changed from pH 4 to 10. Note that the actual potential needs to be subtracted from the measured value because a 1.61 V bias potential was

added to the circuit. The average slope was 61 mV/pH at 100 s, which was consistent with the theoretical Nernstian slope as mentioned in equation (3). When NaCl salt was added to the standard pH4 solution, the potential becomes stable as 84 mV for 20,000 seconds (5.5 hours) with temperature calibration (**Figure 3.7**b).

3.5 DISCUSSION

Using the SWCNT sensor, pH was measured for pH 4, 7, and 10 solutions. The voltage generated from the electrode surface was dependent on ion concentration, which is described by the Nernst equation.

$$E = E^0 + 2.303\frac{RT}{nF}\log_{10}\left(\frac{[\mathrm{Ox}]}{[\mathrm{Red}]}\right)$$

, where Ox: oxidized species, Red: reduced species, [ ]: molar concentration, *F*: Faraday constant (96485 C/mol), *R*: gas constant (8.314 J/K mol), *n*: The number of electrons transferred. E^0: Potential in comparison to hydrogen electrode. T: absolute temperature.

When silver chloride electrodes were used, the reduced species becomes 1; the equation is simplified into $E = E^0 + 0.000198T\ log_{10}[Ox]$. When the temperature was room temperature (298K), $E = E^0 + 0.0591\ log_{10}[Ox]$. Therefore, the potential change becomes 59.1 mV at room temperature when the concentration of a target ion changed by 1 order of magnitude. In our

results, 61 mV/pH was measured in average for the standard pH solutions, which agreed with the theoretical value.

The major difference between conventional ion sensors and the fabricated sensor was in the solid-state layers for pH measurement. Conventional ion sensors are bulky with solution-phase transfer mechanism of ions through an ion selective membrane. The fabricated sensor used SWCNTs as a transducer to change pH into voltage potential. For selective detection of pH, ion selective membrane needs to be added onto the pH sensor.

3.6 CONCLUSIONS

In summary, a gas sensor and a pH sensor were demonstrated using the SWCNT sensors printed with the capillary pen method. The SWCNT sensor doped with PEI showed a response to NO_2 gas. Nafion-doped SWCNTs showed a negligible change when exposed to NO_2 gas but showed very high sensitivity to ammonia gas (3 ppb). The pH sensor showed the voltage potential of 61 mV/pH, which was close to the theoretical value of 59.1 mV/pH.

Chapter 4. A FLEXIBLE IMMUNO-SENSING PLATFORM USING SINGLE-WALLED CARBON NANOTUBES (SWCNT)

4.1 INTRODUCTION

Tuberculosis, caused by *Mycobacterium tuberculosis* (MTB), is one of the serious infectious diseases worldwide. Although the case number gradually declines, developing countries have shown a significantly higher mortality rate[115]. In Asian and African countries, over 80% of populations show positive cases[116]. For initial TB screening, three sputum samples are collected from a patient in the early morning [117]. The sample collection procedure is repeated for a few times in order for initial screening. The collected samples are diagnosed with various methods, such as a Ziehl-Neelsen (ZN) method for microscopic detection, immunoassays for antigen detection[118], polymerase chain reaction (PCR) for DNA or RNA detection[119, 120]. The ZN smear method is labor-intensive, and not sufficiently sensitive for TB diagnosis. Enzyme-linked immunosorbent assay (ELISA) is a rapid and relatively easy tool but with low sensitivity. Among the approaches, PCR-based methods have shown clinical sensitivity and specificity greater than 95% but with 2 hours of detection time [121].

In the whole screening time, the significant time for the screening is occupied by the liquefaction process of sputum samples. Since sputum samples are thick and viscous, the samples need to be dissipated potentially with disinfection process for safe screening. The processing time typically requires at least 20 minutes, which has been a major hurdle for point-

of-care (POC) screening of TB. In addition, sputum sample collection has been a challenging problem for kids and babies. Recently, a clinical study has been conducted to discover a new biosample source. Oral swab samples have been found as a convenient and noninvasive source for TB diagnosis [122, 123]. Using oral swab samples, a POC screening tool can be realized as far as a simple but highly sensitive and specific sensor is offered.

For a highly sensitive and specific screening tool, nanomaterials have been persistently investigated for infectious disease diagnosis. Among the nanomaterials, single-walled carbon nanotubes (SWCNTs) are one of the potential candidates to enable a simple resistive transducer to detect the binding of a target analyte with high sensitivity. In comparison to optical and fluorescent detection, a resistive sensor runs with small power and small form factors. Since optical focus and magnification is not required, a light pocket-size device can be developed as a measurement unit. The high sensitivity of an SWCNT biosensor is originated from the small diameter (~1 nm) comparable to the size of single biomolecules and the thickness of electrical double layers in physiological buffer [124].

Resistive SWCNT sensors can detect targets by two distinct mechanisms [125-128]. One is to change the free carrier density of doped SWCNTs by electrostatic interaction. The other is to change the work function of the metal electrodes-SWCNT interface, thus leading to Schottky barrier modulation. For semiconducting nanotubes, both mechanisms play a role in modulating the resistance. When SWCNTs were deposited on gold electrodes patterned on a silicon substrate, viral particles and bacteria could be detected by measuring the resistance change [129, 130]. The detection limit of swine influenza virus (H1N1) was 177 TCID (50 % Tissue culture Infective Dose) /mL [129]. The detection limit for B. Subtilis was 100 CFU/mL [130]. SWCNTs functionalized with heparin could detect dengue virus as low as 840 TCID/mL [131]. The lowest

detection limit was 1 PFU/mL to detect H1N1 [132]. In addition, a similar configuration of SWCNT sensor was applied to detect peanut allergen in food extract with the detection limit of 5 ng/mL [133]. In mRNA detection, the detection limit was demonstrated in an attomolar level, which has the potential to detect nucleic acid without amplification [134]. In our previous work, nanotips made of SWCNTs could be used for bacterial detection [135]. The crossbar junctions coated with SWCNTs were fabricated to detect target bacteria in food samples [136]. The sensor substrate, electrical layers, target samples, detection limit, and targets are summarized in **Table 2**.

Number	reference	Substrate	Electrical layer	Target sample	Detection limit	Target
1	[132]	Silicon/oxide	On Au	Buffer	1 PFU/mL	H1N1
2	[130]	Silicon/oxide	On Au	Buffer	100 CFU/mL	B. Subtilis
3	[133]	Silicon/oxide	On Au	Food extract	5ng/mL	Ara h 6
4	[129]	Silicon/oxide	On Au	buffer	177 TCID/mL	H1N1 (10, 20 and 50 um gaps)
5	[131]	Silicon/oxide	On Au	buffer	840 TCID/mL	dengue virus
6	[134]	Silicon	On Au	buffer	aM	mRNA
7	[135]	Tungsten wire coated with Au	On Au	buffer	10^3 CFU/mL	BCG bacteria
8	[136]	Crossing tungsten wires coated with Au	On Au	buffer	10^2 CFU/mL	Escherichia coli

Table 2. Resistive single-walled carbon nanotubes for detection of bioanalytes

In spite of the great potential as a POC screening sensor, few resistive SWCNT biosensors have been demonstrated for target detection in human samples. One of the main

challenges was the screening effect by high ion concentrations in physiological buffer. Positive and negative ions covering SWCNTs rendered both electrostatic and Schottky modulation disabled and unpredictable. For immunoassay, the challenge was resolved by rinsing with deionized (DI) water. The sensing mechanism of DI-rinsed SWCNTs could be recovered without losing the binding activity of antigen-antibody. In addition to the screening effect, hydrogen binding on SWCNTs in the water-based buffer could generate unreliable resistance change due to absorption and desorption of hydrogen. For example, when SWCNTs were bound with antibodies in the physiological buffer, hydrogen was bound on SWCNTs to increase the resistance. As soon as the sensor was exposed to air out of the buffer, the electrical resistance started to decrease. The resistance change by target bindings could be interfered with that by hydrogen release, which could reduce the sensitivity and reliability.

In this paper, a resistive SWCNT biosensor is fabricated on a flexible film, polyethylene terephthalate (PET) for low-cost TB screening. Silver electrodes are stamped as probing electrodes for SWCNTs. The sensing mechanism of SWCNTs coupled with silver electrodes is investigated in conjunction with hydrogen desorption. The sensitivity and specificity are characterized by MTB and surface antigen (MPT64) in PBS. Subsequently, the sensor is characterized by tongue swab samples spiked MTB and MPT64. Simple resistive measurement is conducted before and after immunocomplex formation for detecting targets. The presented biosensor will move one step further to a POC platform for rapid and low-cost TB screening.

4.2 OBJECTIVES

The objective in this chapter is to develop a flexible immuno-sensing platform using single-walled carbon nanotubes (SWCNT) with high sensitivity. A resistive SWCNT biosensor is fabricated on a flexible film, polyethylene terephthalate (PET) for low-cost TB screening. Silver electrodes are stamped as probing electrodes for SWCNTs. The sensing mechanism of SWCNTs coupled with silver electrodes is investigated in conjunction with hydrogen desorption. The sensitivity and specificity are characterized by MTB and surface antigen (MPT64) in PBS. Subsequently, the sensor is characterized by tongue swab samples spiked MTB and MPT64. Simple resistive measurement is conducted before and after immunocomplex formation for detecting targets. The presented biosensor will facilitate a POC TB screening platform with a small form factor, low power requirement, and easy use.

4.3 EXPERIMENTAL METHOD

4.3.1 *Sensor fabrication*

The sensor was fabricated on a polyethylene terephthalate (PET) film (**Figure 4.1**a). Target cells and antigen are detected by using an SWCNT sensor functionalized with Polyethyleneimine (PEI) and antibodies (**Figure 4.1**b). Silver electrodes are patterned for

resistive detection. When targets are bound on the sensor surface, the resistance decreases due to the electrostatic interaction.

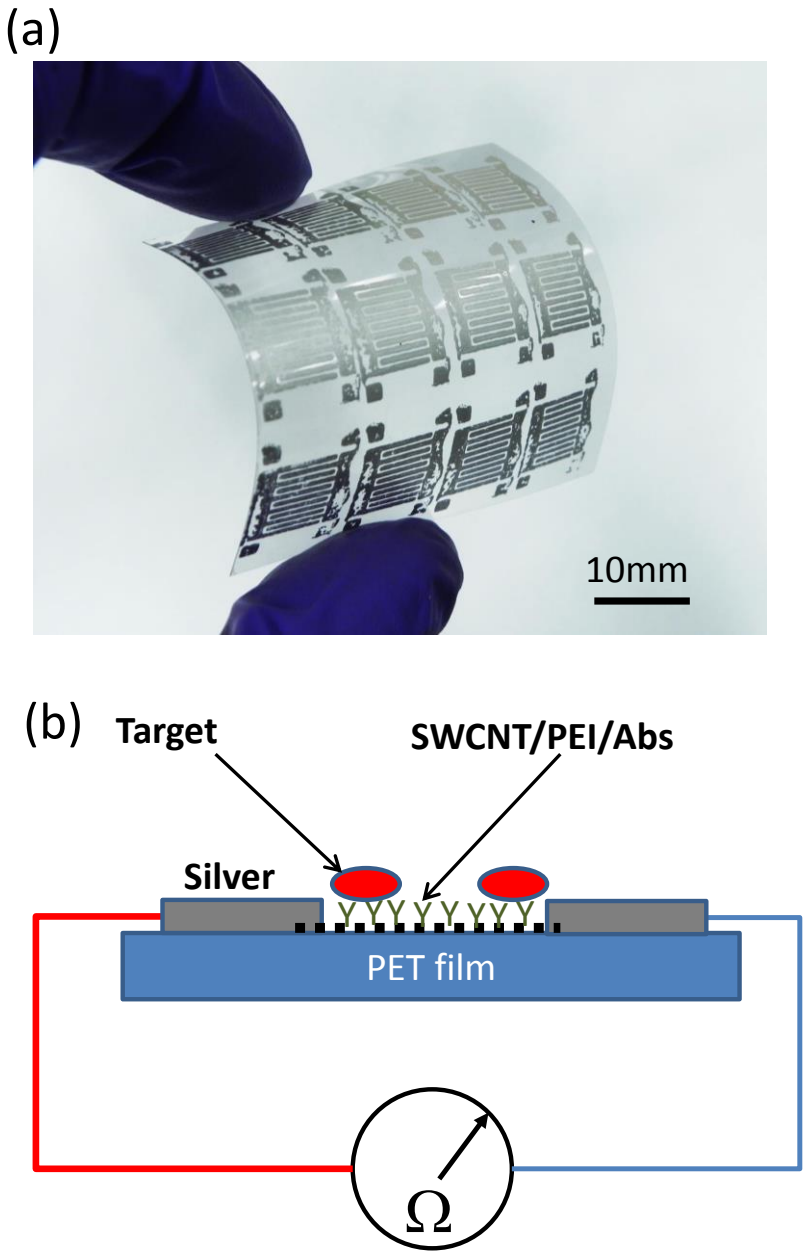

Figure 4.1. (a) An SWCNT-based sensor on a flexible PET film. (b) Cross section of a resistive SWCNT immunosensor.

For fabrication (**Figure 4.2**a~**4.2**d), SWCNTs were dispersed in SDS at a concentration of 1 mg/mL using a sonicator at room temperature for 8 hours. The SWCNTs were spin-coated on a PET film at 6000 rpm for 20 seconds. PEI (0.1 %) was coated on the SWCNT surface. Silver ink was stamped on the PEI coated SWCNT surface. For silver electrode patterning, a Delrin® mold was machined by using an end mill. The stamp was made of polydimethylsiloxane (PDMS) cured in a mold at room temperature for 3 days. The PDMS stamp coated with silver ink was stamped on a PEI-coated SWCNT sensor. The sensor was cured on a hot plate for 10 min at 100 ℃. A polyclonal IgY antibody (1.8 mg/mL) raised against MPT64 protein was physisorbed on the SWCNT surface for 24 hours in the refrigerator (4 ℃). Subsequently, one sensor was cut by scissors by half in order to make 2 sensors. With the cutting, a total of 24 sensors could be fabricated on a 40x40 mm^2 PET film. **Figure 4.2**e shows a photo showing a sensor composed of two interdigitated electrodes. The gap is filled with functionalized SWCNTs. The magnified image shows the gap size of 200~300 μm.

Unlike other SWCNT immunosensors, the SWCNTs in a sensor were coated with silver electrodes, which minimized the exposure of the interfacial area between SWCNTs and silver electrodes. The sealing of the interfacial area could offer a uniform contact resistance and isolate the Schottky effect in the sensing mechanism. The electrostatic gating effect was only the mechanism to detect the target analytes. In the configuration, the oxidation of the silver electrode surface should not interfere with the resistive change for target detection.

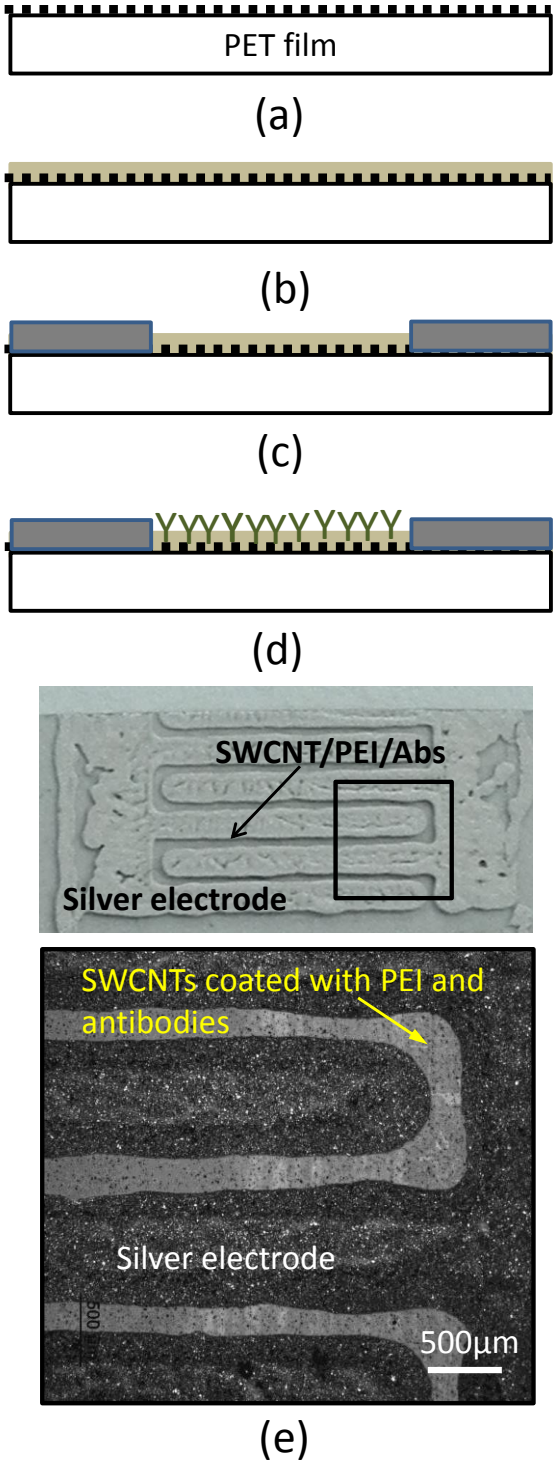

Figure 4.2. The fabrication process of an SWCNT-based immunosensor (a) Spin coating of SWCNTs on a PET film (b) Spin coating of PEI (c) Stamping of silver electrodes. (d) Antibody immobilization (e) Photo and optical microscope images of an SWCNT immunosensor.

4.3.2 *Antibody preparation*

A polyclonal IgY antibody (pAb) was raised against purified MPT64 protein in Aves Labs (Davis, CA, USA). Complete Freund's adjuvant was used; thus, antibodies were reactive to MTB as well as MPT64. The antibodies were raised in two hens and evaluated by ELISA to determine protein binding, and filter plate EIA to determine reactivity to target cells.

To evaluate antibodies against *Mycobacterium*, cultures of BCG and MTB H37Ra cells were diluted to $1x10^7$ cells/mL in PBS. Cell solutions were then added to a 96-well filter bottom plate (Millipore 0.45 µM, #MAHVN4510), 100 µL of a $1x10^7$ cells/mL solution of MTB or BCG. The cells were trapped by the 0.45-micron filter, and buffer/media was washed. Cells were washed with vacuum filtration, 3x200 µl DPBS. 28 µg/mL IgY antibody (100 µl) was added to each well and incubated for 30 min at 37 ℃. Control (pre-immune IgY) antibodies were tested at the same concentration. The IgY solution was washed with 4x200ul DPBS. A 100 µl solution of a 2 ° antibody (1:1000 dilution Rab anti-IgY-HRP Conjugate, Thermo Scientific #31401) was added and incubated for 30 min at 37 ℃, followed by DPBS washing (3x200 µL). Finally, 100 µl ABTS substrate (Thermo Scientific #37615) was added, followed by a 10-minute incubation at room temperature. The solution was then filtered through the filter plate and into a clear 96-well plate and read at A_{405} in a microplate reader. **Figure 4.3**a shows the positive results of the antibodies for both BCG and MTB H37Ra. According to the results, the polyclonal antibodies were specific to Mycobacterium strains, potentially, including non-tuberculosis Mycobacterium (NTM) species. The specificity test will be conducted using an SWCNT immunosensor.

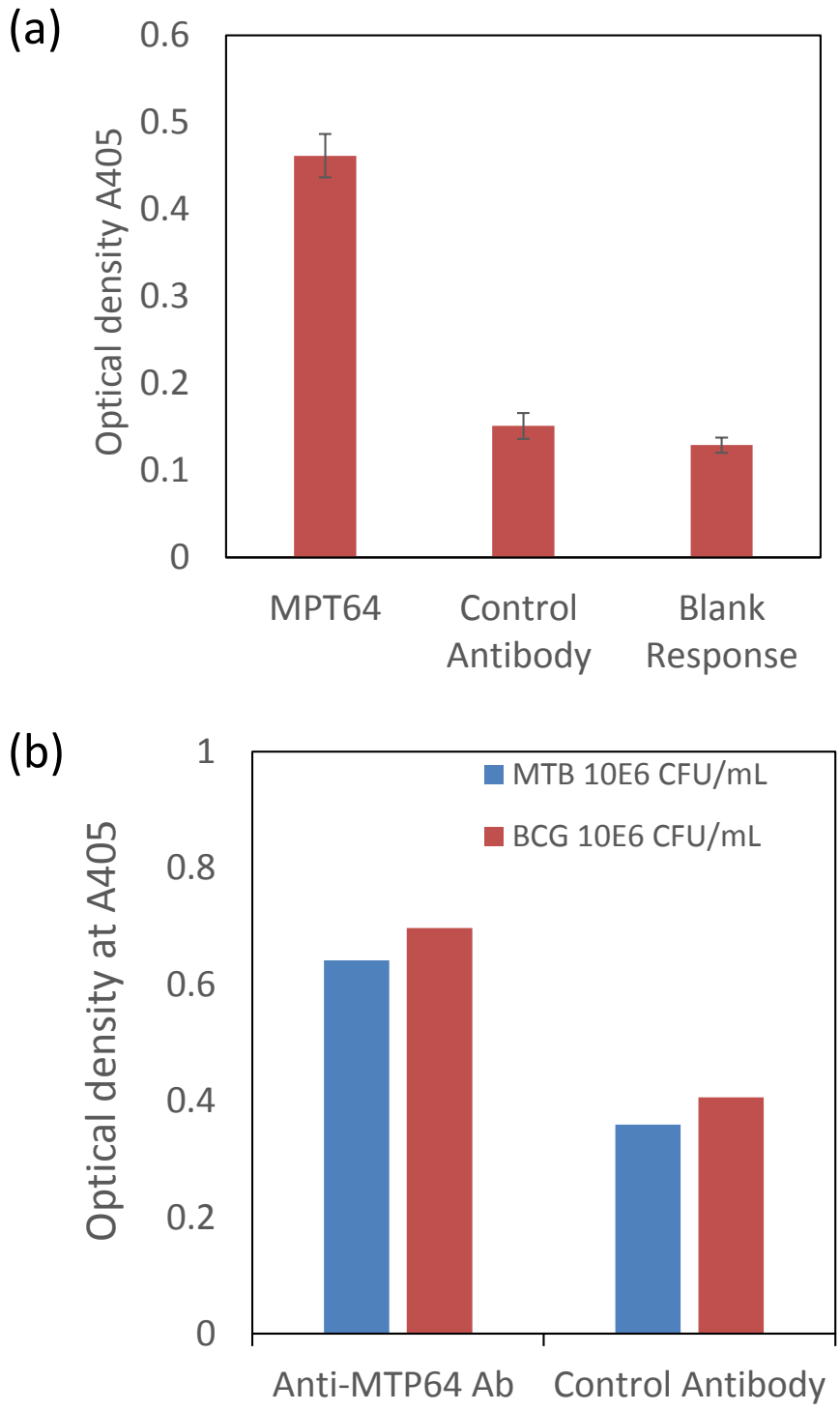

Figure 4.3. (a) Optical density showing the binding of MPT64 antibodies to MTB (10^6 CFU/mL) and BCG (10^6 CFU/mL) at 28 µg/mL. (b) Optical density showing the binding of MPT64 antibodies to MPT 64 in comparison to control.

To assay the MPT 64 protein, 100 µL of a 100 µg/mL solution of MPT-64 in DPBS was added to an ELISA protein binding 96-well plate (Immulon 2HB, Thermo Scientific #3455). The mixed solution was incubated overnight at room temperature, followed by 1 hour at 37 ℃, and then washed with 3x200 µL DPBS. To block the remaining sites in the well, a 200 µl BSA solution in DPBS at 1 mg/ml was added and incubated for 1 hour at 37 ℃ followed by washing with 3x200 µL DPBS. A 100 µL solution of IgY raised to MPT-64 was added to each well at a concentration of 28 µg/ml in DPBS. Control (pre-immune IgY) antibodies were tested at the same concentration. A 100 µl solution of a 1:1000 Dilution of 2 ° (Rab anti-IgY-HRP Conjugate, Thermo Scientific #31401) was then added and incubated for 30 min at 37 ℃, followed by DPBS washing (3x200 µL). Finally, 100 µl of ABTS substrate (Thermo Scientific #37615) was added and measured at A_{405} after 10-minute incubation at room temperature. **Figure 4.3**b shows the positive results from the antibodies to MPT-64 compared to pre-immune antibodies.

It is acknowledged that antibody secretion and characterization were conducted by Mr. Soelberg in Furlong's group. We appreciate the advice and support for the successful development of the TB screening assay.

4.3.3 *Sensor characterization*

After antibody immobilization, the resistance of SWCNT sensors increased due to antibody binding and hydrogen binding on SWCNTs. To study the contribution of resistance increase in an antibody immobilization step, the antibody concentration varied from 0, 0.9, 1.8, and 4.5 mg/mL in PBS buffer. After 24 hours of incubation of SWCNT sensors in each solution, the normalized resistance change was measured before and after antibody immobilization.

As soon as the sensor was exposed to air, the sensor resistance started to decrease due to the desorption of hydrogen. The desorption process was critical to obtain a reproducible resistance measurement after binding targets. To characterize the resistance change due to the hydrogen desorption, the resistance change was measured for 5 hours. One sensor was incubated at 25 ℃, and the other sensor was incubated at 35 ℃ on a hot plate. The relative humidity was 25~30 % in the tests. Since antibodies were immobilized on the sensor surface, the sensor temperature was not tested over 35 ℃ in order to avoid potential damage or degradation of antibodies.

To characterize how the sensor response was changed due to hydrogen desorption, the sensor response to targets (MTB at 10^6 CFU/mL in PBS) binding was tested after 5, 20, 40 and 120 minutes of incubation at both 25 and 35 ℃. The sensor response for MTB at 10^6 CFU/mL in PBS was compared for each condition in comparison to the control (PBS). The incubation time of 5, 20, 40, and 120 minutes was determined in consideration of the slope change of the resistance at 35 ℃.

4.3.4 *Sensitivity and specificity tests*

For sensitivity and specificity tests, both MTB and MPT64 were suspended in 1x PBS buffer. For MTB, various concentrations of MTB cells were suspended in PBS from 10^1~10^5 CFU/mL. MPT64 was also suspended in PBS from 0.1 ng/mL to 1μg/mL with 10 fold dilutions. 1 mL of each solution was supplied in each plastic cup where a sensor was dipped for immunocomplex

formation. After 10 min of incubation, the sensor was rinsed with DI water. After the gentle blow dry with nitrogen, the resistance was measured. The resistance values before and after immunocomplex formation were R_0 and R_f, respectively. The normalized resistance change [R_f-R_0)/R_0] was computed to compare the normalized resistance change from control.

For specificity test, the response for MTB (10^2 CFU/mL) was compared with Staphylococcus epidermidis (S. Epi at 10^3 CFU/mL), Mycobacterium Avium (M. Avium at 10^3 CFU/mL), and Mycobacterium Bacillus Calmette–Guérin (M. BCG at 10^3 CFU/mL). Each bacterium species was suspended in 1 mL-PBS.

4.3.5 *Test using tongue swab samples*

As described earlier, a tongue swab sample was one of the new types of oral swab samples that contained MTB markers. To evaluate LLD for MTB and MPT 64 in tongue swab samples, swab samples were prepared by scraping tongue surface from deidentified volunteers as illustrated in **Figure 4.4**. After a complete dry of swabs in air, the swab samples were immersed in 1 mL PBS contained in an individual microtubule for 20 minutes with gentle stirring. Subsequently, 500 μL of target analytes (MTB or MPT 64) in PBS was mixed with 500 μL of the eluted swab solution. The 1 mL solution was used to test LLD. The concentrations of MTB were 10~10^5 CFU/mL with 10 fold dilutions. The concentrations of MPT64 ranged from 1 ng/mL to 10 μg/mL with 10 fold dilutions. A sensor was incubated in 1 mL sample solutions for 10 minutes. After rinsing with DI water, the resistances were measured. Before and after the incubation, the resistances were measured to compute a normalized resistance.

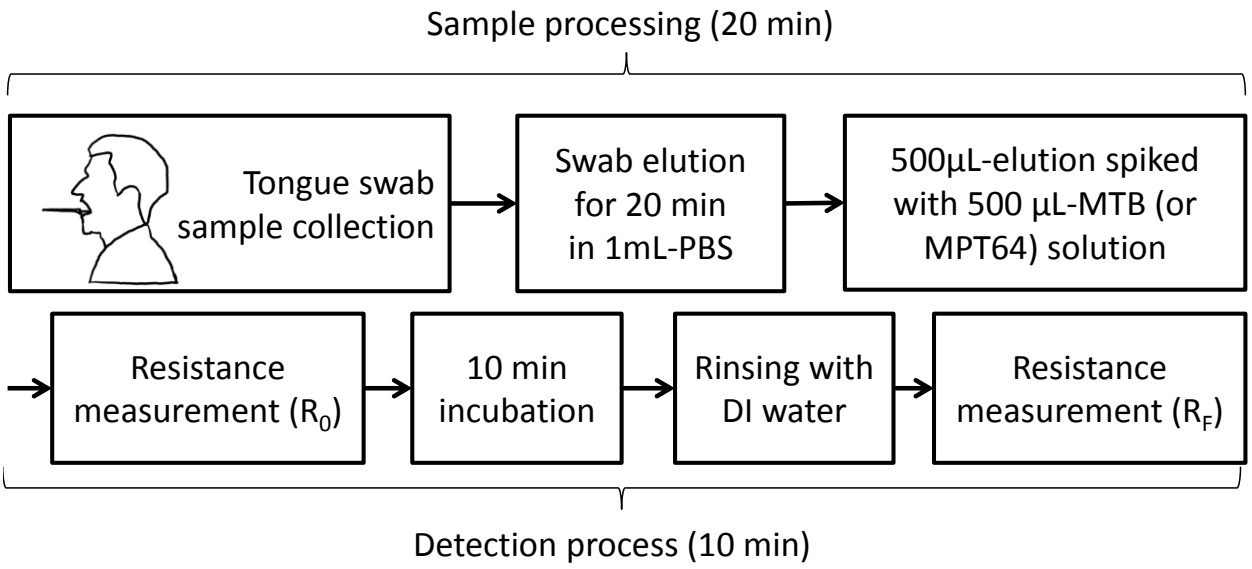

Figure 4.4. Preparation protocol of tongue swab samples and resistive detection procedure.

4.4 EXPERIMENTAL RESULTS

In the antibody immobilization step of 24 hours, the resistance of SWCNT sensors was changed by the bindings of both hydrogen and antibodies. Since the most ions in PBS were washed in the rinsing step after antibody immobilization binding, the effect of ions in PBS could be neglected. **Figure 4.5**a shows the normalized resistance change of SWCNTs before and after antibody immobilization for antibody concentrations of 0.9, 1.8, and 4.5 mg/mL. The normalized resistance change of SWCNTs in PBS was 1.78 while that in antibody solutions varied from 2.04

to 2.12 on average. 78 % of the resistance change was contributed by hydrogen binding, and 30 % was by antibody binding.

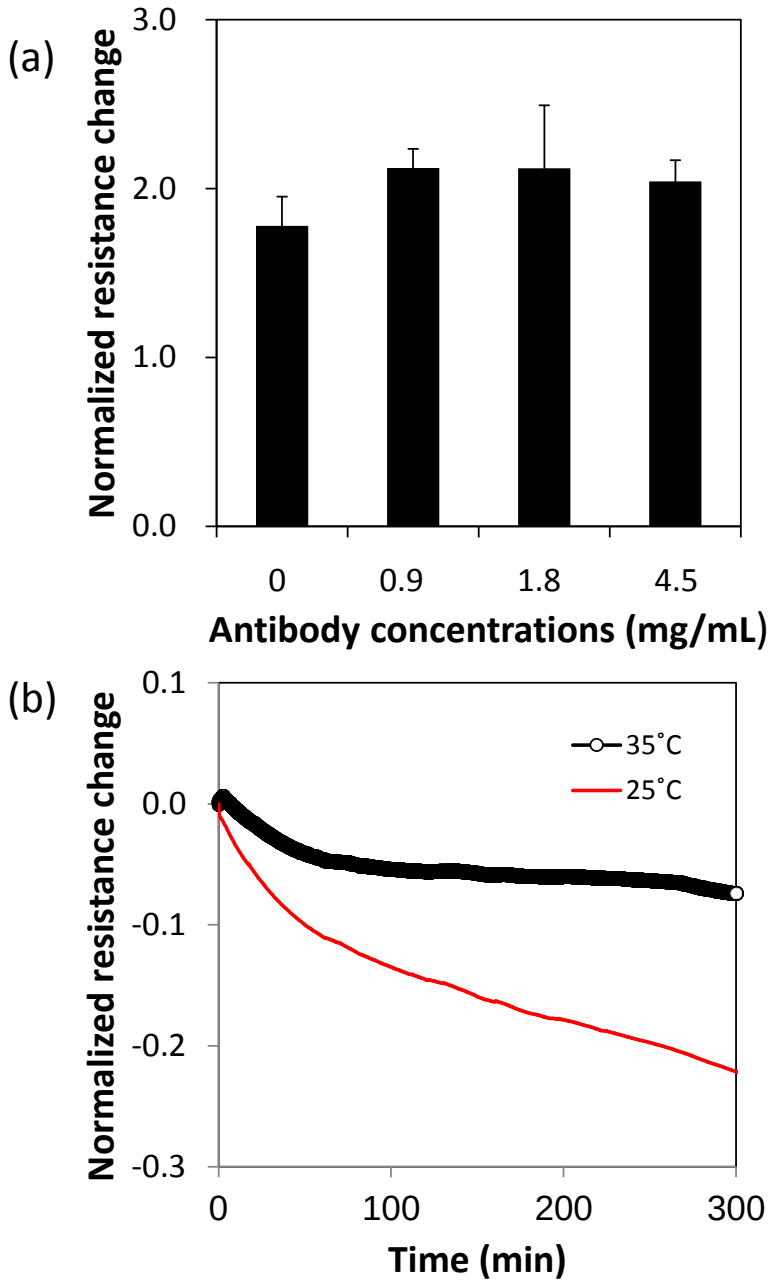

Figure 4.5. (a) Normalized resistance change before and after antibody immobilization on SWCNT sensors (N=4) (a) Normalized resistance change of an SWCNT immunosensor at 25 and 35 ℃ after antibody immobilization.

To study the resistance change due to antibody binding and proton adsorption, the resistances were measured after antibody immobilization of 24 hours. The resistance rapidly decreased as soon as sensors were taken out of the antibody solution container. When sensors were exposed to air, one batch of the sensors was left in air at 25 ℃, and the other batch was heated 35 ℃ for 300 min. **Figure 4.5**b shows the normalized sensor resistance change at 25 and 35 ℃ for 300 min. The resistance drop for 25 ℃ was monotonous while that for 35 ℃ was larger before 20 min and smaller after 20 min. The larger drop at 35 ℃ was expected because a larger number of hydrogen were desorbed at a higher temperature. As time went by, the resistance drop at 25 ℃ became more significant. The resistance decrease also affected the doping level of an SWCNT sensor. For SWCNTs immersed in water, the SWCNTs could be doped with a high concentration of hydrogen and proton, which could dominate the resistance change.

To study the desorption effect of hydrogen on sensor performance, the immunoassay using SWCNT sensors was tested for a sensor after 5, 20, 40, and 120 minutes of incubation at 25 and 35 ℃. **Figure 4.6**a shows the change of a normalized resistance for MTB (10^6 CFU/mL) in comparison to the control.

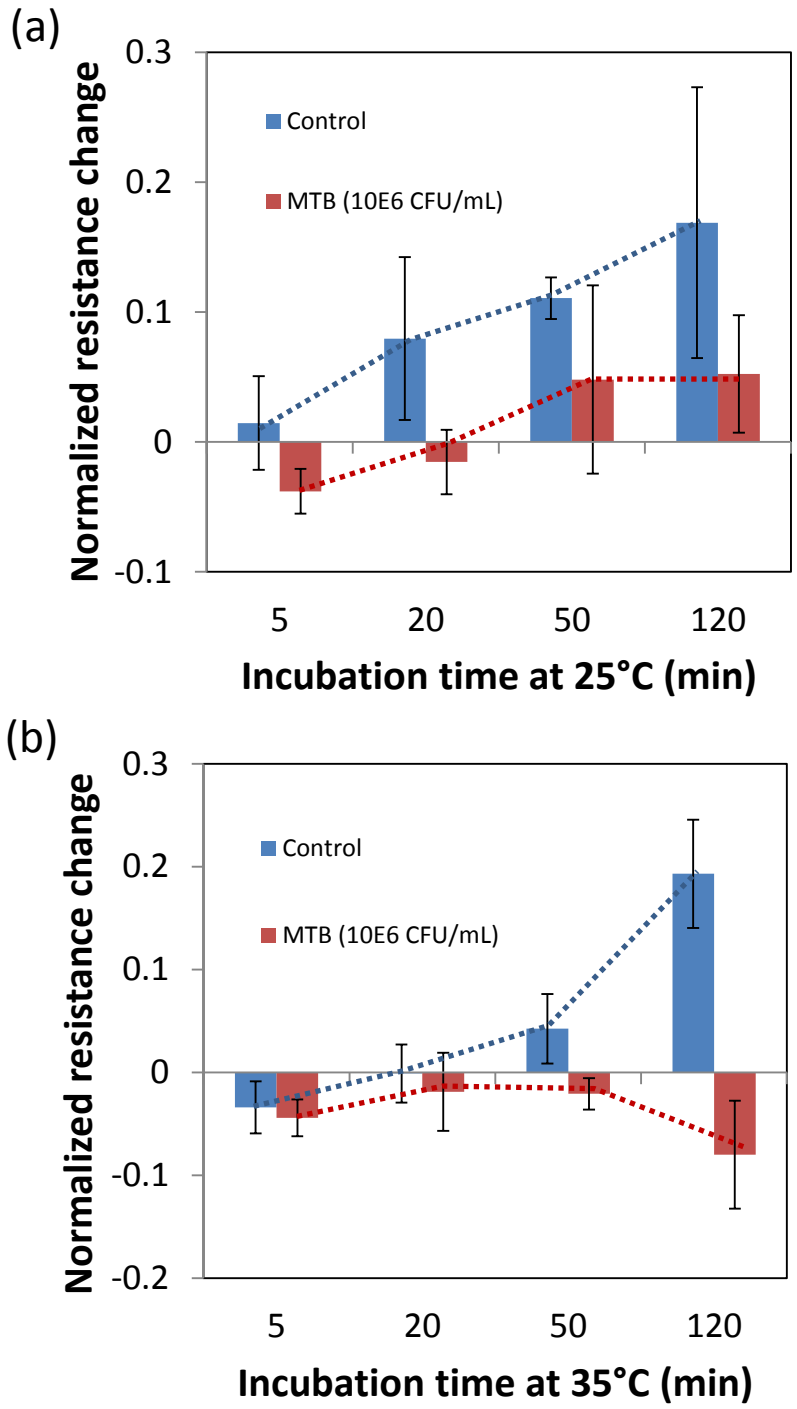

Figure 4.6. (a) The resistance change of an SWCNT immunosensor at 25 and 35 ℃ after antibody immobilization. (b) Normalized resistance change of a SWCNT sensor for control and MTB (10^6 CFU/mL) in PBS (N = 4). The sensor is tested after 5, 20, 40, and 120 min incubation at 25 ℃.

The normalized resistance of the control samples increased for both control and MTB. However, the error bar was too large to differentiate the MTB signal from the control. **Figure 4.6**b shows the normalized resistance change for MTB (10^6 CFU/mL) at 35 °C. The control was negative at 5 min and gradually increased to the positive value. The normalized resistance of the positive MTB samples maintained slightly negative values and dropped to -0.08. When the control was compared with the positive cases, a signal could be detected for the samples of 40 and 120 min incubation at 35 °C. **Figure 4.7** shows the resistance change of an SWCNT sensor after 0.1% PEI coating and antibody coating with 120 min incubation. The resistance of SWCNT sensors increased from 292 to 669 Ω after antibody coating. In a further experiment, the incubation time was set as 120 min for reliable performance of the sensors.

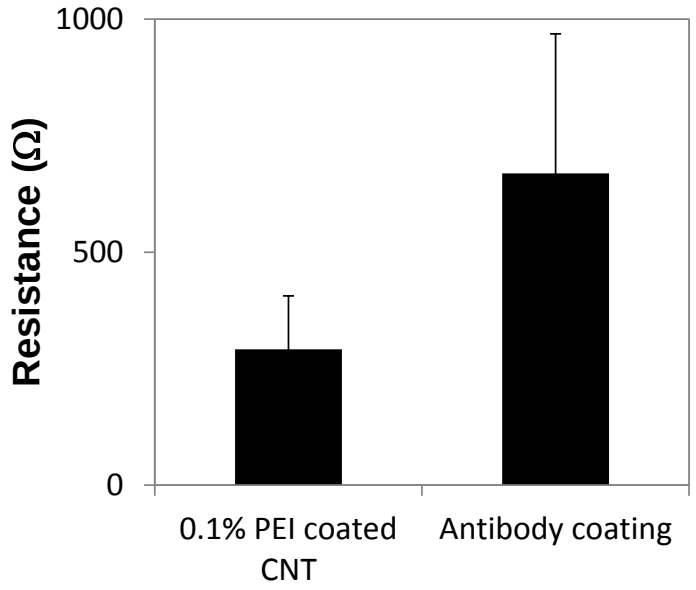

Figure 4.7. Resistances of 0.1% PEI coated SWCNTs and antibody-coated SWCNTs. The resistance is measured after 2 hours at 35 ℃.

For a sensitivity test, various concentrations of MTB cells in a PBS buffer were tested, as shown in **Figure 4.8**a. In comparison to the control group, the signal was measured from 10 CFU/mL. In the tests, the normalized resistance change for the control was measured between 0.15 and 0.25 throughout the tests. The average value of the normalized resistance for the control was shifted to 0 for convenience of signal reading. According to the down-shift of the control, the signal was further shifted by the same magnitude. In spite of the high sensitivity, the resistance change was not quantitative in comparison to the MTB concentrations. When the dose-response test was conducted for antigen MPT64 **Figure 4.8**b, the signal was measured form 10 ng/mL.

For a specificity test, the signal of MTB at 100 CFU/mL was clearly differentiated from the control and S. epi at 10^3 CFU/mL (**Figure 4.9**). However, M. Avium (10^3 CFU/mL) and M. BCG (10^3 CFU/mL) showed the signal due to the polyclonal antibodies, which showed the cross-reactivity to Mycobacterium strains, including NTM. The cross-reactivity to Mycobacterium strains was consistent with that to the ELISA assay.

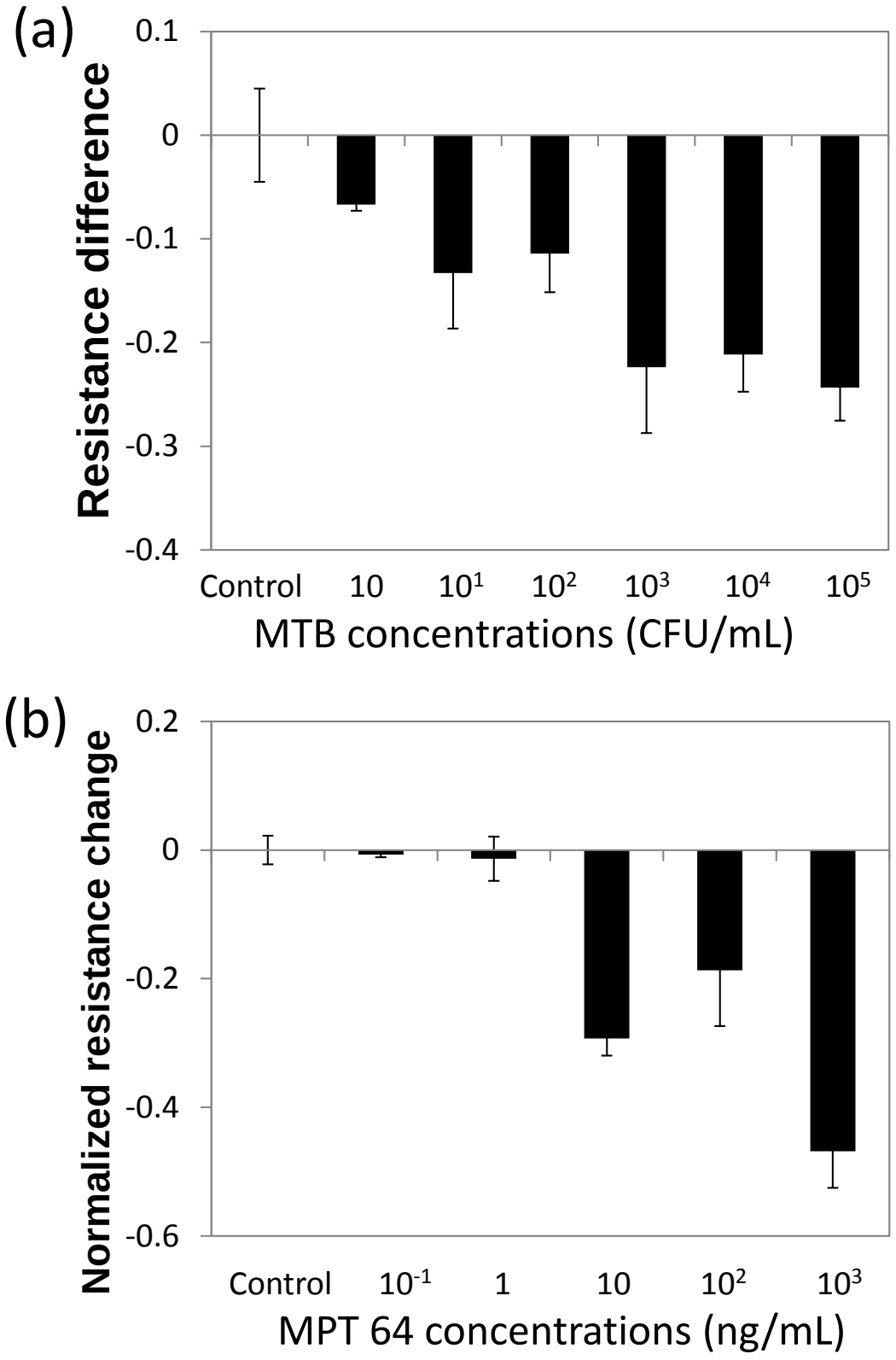

Figure 4.8. (a) Sensitivity test for MTB in PBS. (b) Sensitivity test for MPT64 in PBS.

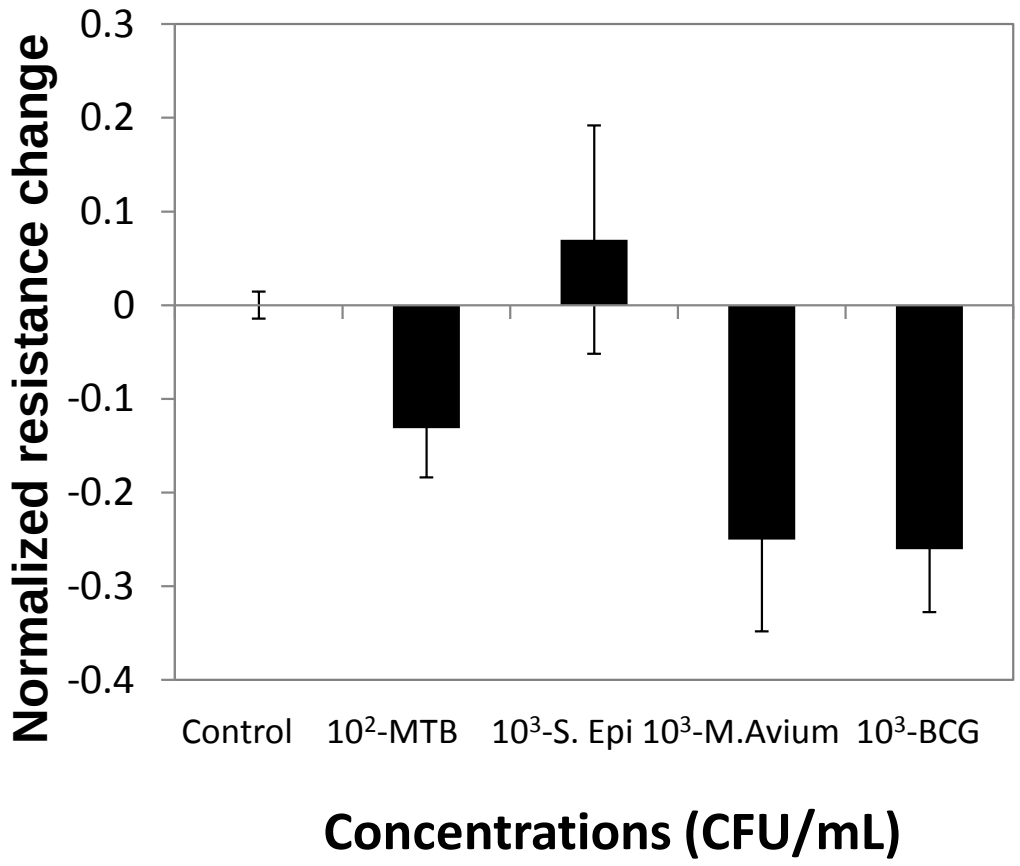

Figure 4.9. Specificity test results for MTB (10^2 CFU/mL), S. Epi (10^3 CFU/mL), M. Avium (10^3 CFU/mL), and M. BCG (10^3 CFU/mL).

To validate if the target cells were captured on a sensor surface, MTB cells (10^6 CFU/mL) stained with SYTO9 green fluorescent dyes (Excitation/Emission: 485/498 nm; LIVE/DEAD BacLight Bacterial Viability Kit, ThermoFisher Scientific) were observed on the sensor surface (**Figure 4.10**). The signal was not clear to detect an individual cell due to the high background fluorescent signal of a PET film and silver surface. However, big colonies could be detected on the SWCNT sensor surface. The qualitative, not quantitative signal could be caused by the

binding nature between bacterial cells and sensor surface. Considering the effective range of electrostatic detection as 10 nm, the nonuniform binding of target cells could cause the qualitative signal. The nonquantitative signal could also be coupled with the large gap size of 500 μm, explaining the saturation of the resistance change in large gap size.

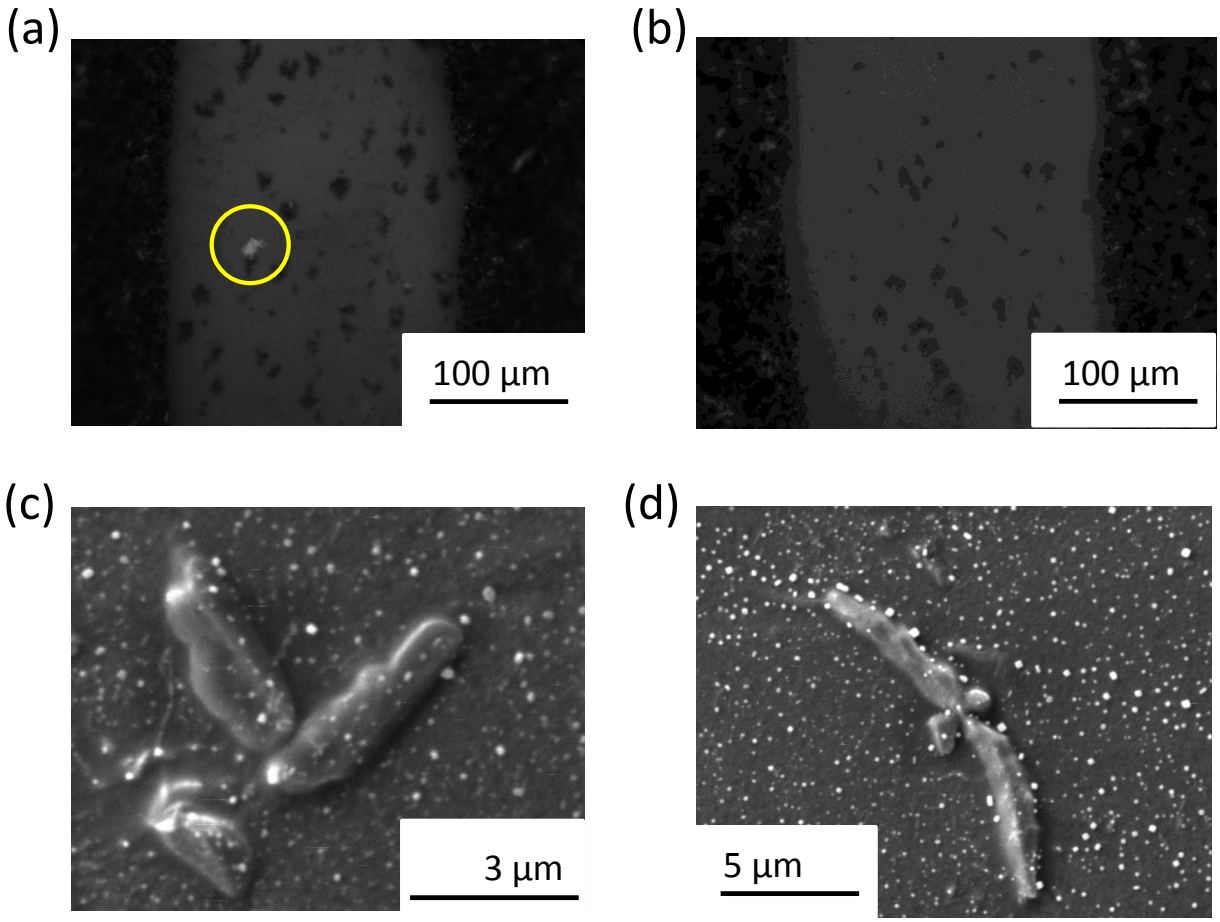

Figure 4.10. (a) Fluorescence microscope images for an MTB colony (10^6 CFU/mL). (b) Control samples. The grey area is the SWCNTs on a PET film. The black area is a silver electrode. (c) and (d) SEM images of MTB cells (10^6 CFU/mL).

To evaluate the LLD for tongue swab samples, MTB at various concentrations from 10 and 10^5 CFU/mL were spiked in tongue swab samples. The detection limit was 10 CFU/mL

(**Figure 4.11**a). According to the dose-response test, the resistance change was not quantitative but qualitative. For the detection limit test using MTP-64 antigen, the LLD was 100ng/mL, which was also qualitative (**Figure 4.11**b).

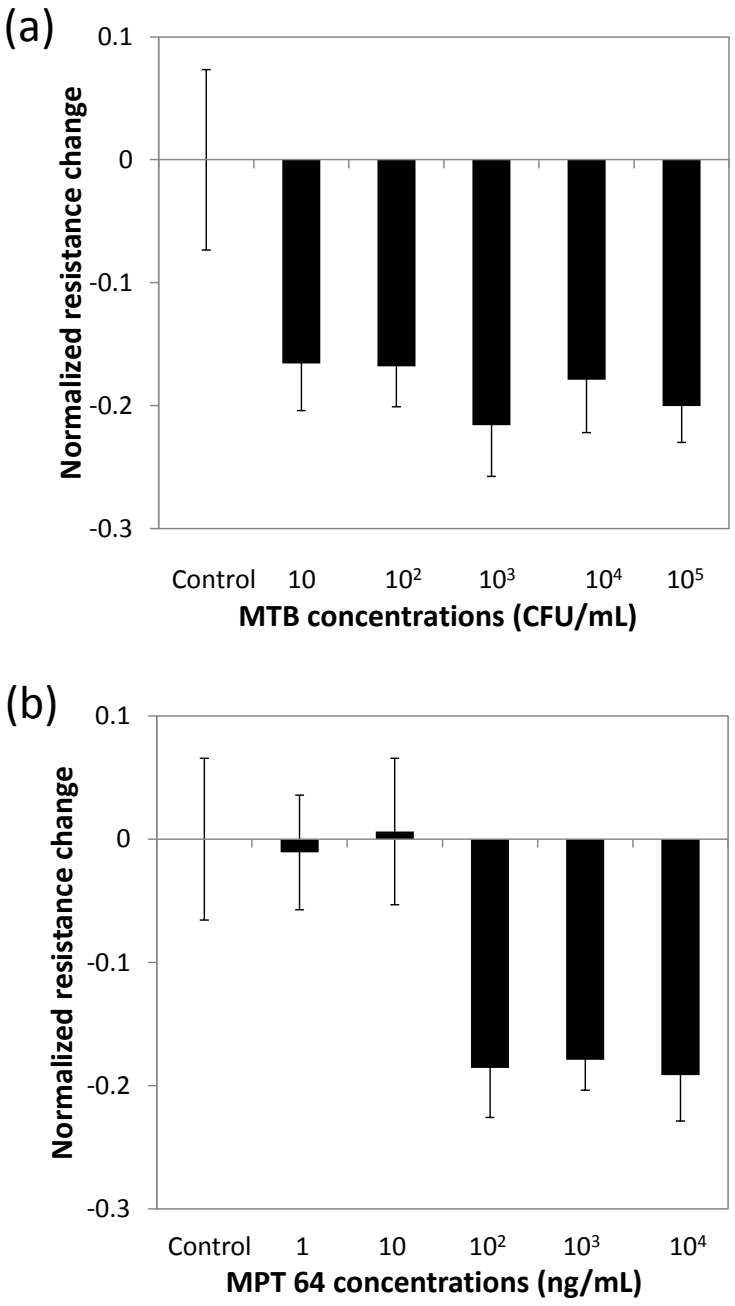

Figure 4.11. Detection limit tests for MTB and MPT 64 (a) MTB spiked in tongue swab samples, (b) MPT64 antigen spiked in tongue swab samples.

Given that tongue swab samples were replete with human cells, bacteria, and other microorganisms, these results also demonstrated the superior specificity of the SWCNT sensor.

The substrate used for the sensor was a PET film. Since the PET film was flexible, the sensor could be attached or bent to fit a testing condition, the resistance change upon bending was tested (**Figure 4.12**).

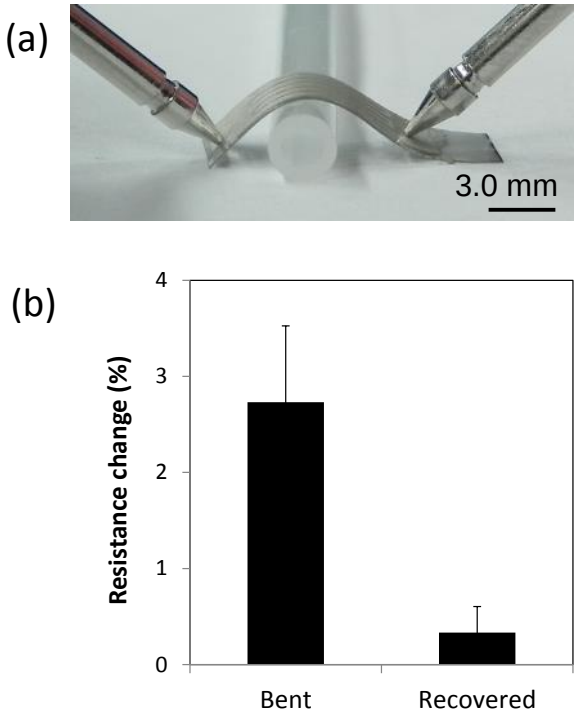

Figure 4.12. (a) Bending test using 3 mm silicone bar (b) Resistance change for the 1st bending and the 1st recovery (N=6).

When the sensor was bent by a radius of 1.5 mm and recovered with the stress release, the resistance change was 0.33 %. In comparison to the change of signal resistance of 10 or more percentage, 0.33 % resistance change could be neglected. However, the resistance change upon

bending was 2.73 %, which could not be neglected. The bending test results show that the sensor could be bent during target binding and operation. However, the measurement should be conducted without external stress. The flexible nature of the sensing platform will benefit the sensor application to platforms requiring a small form factor and low cost.

4.5 CONCLUSIONS

In summary, the resistive immuno-SWCNT sensor was developed to specifically detect Mycobacterium cells spiked in tongue swab samples. The detection limit was 10 CFU/mL in tongue swab samples, which was comparable to PCR but without requiring bacteriological culture, centrifugation, or nucleic acid amplification. MPT64 antigen spiked in tongue swab samples was detected at 100 ng/mL. To achieve such high sensitivity and specificity, a challenge of an SWCNT sensor coupled with hydrogen adsorption and desorption was studied to find optimal curing time of 2 hours at 35 °C. Due to the desorption of proton on the SWCNT surface, more stable resistance measurement could be obtained. Unlike other SWCNT-based sensors, the presented sensor was fabricated on a flexible PET film, which offered an extremely low cost and lightweight platform. The small form factor will benefit low-cost diagnosis of TB in military bases and underdeveloped countries. The simple resistive measurement will allow rapid screening by minimally trained personnel within 30 minutes from tongue swab samples. In addition, the minimal power requirement (<1 W) combined with low assay cost is ideal for point-of-care (POC) screening in limited resource settings.

REFERENCES

[1] P. Lamkin, "Wearable Tech Market To Be Worth $34 Billion By 2020," *Forbes*, pp. https://www.forbes.com/sites/paullamkin/2016/02/17/wearable-tech-market-to-be-worth-34-billion-by-2020/#622e0d763cb5, 2016.

[2] E. S. Izmailova, J. A. Wagner, and E. D. Perakslis, "Wearable Devices in Clinical Trials: Hype and Hypothesis," *Clinical Pharmacology & Therapeutics*, vol. 104, pp. 42-52, Jul 2018.

[3] J. Edwards, "Wireless Sensors Relay Medical Insight to Patients and Caregivers," *Ieee Signal Processing Magazine*, vol. 29, pp. 8-12, May 2012.

[4] K. Malhi, S. C. Mukhopadhyay, J. Schnepper, M. Haefke, and H. Ewald, "A Zigbee-Based Wearable Physiological Parameters Monitoring System," *Ieee Sensors Journal*, vol. 12, pp. 423-430, Mar 2012.

[5] H. Yao, Y. Liao, A. R. Lingley, A. Afanasiev, I. Lahdesmaki, B. P. Otis, *et al.*, "A contact lens with integrated telecommunication circuit and sensors for wireless and continuous tear glucose monitoring," *Journal of Micromechanics and Microengineering*, vol. 22, Jul 2012.

[6] J. Park, J. Kim, S. Y. Kim, W. H. Cheong, J. Jang, Y. G. Park, *et al.*, "Soft, smart contact lenses with integrations of wireless circuits, glucose sensors, and displays," *Science Advances*, vol. 4, Jan 2018.

[7] S. Shibata, Y. Kishi, N. Murashige, and M. Kami, "The lower pole of the earlobe is an alternative site for painless blood sampling in the self-assessment of blood glucose concentrations," *Internal Medicine*, vol. 43, pp. 787-791, Sep 2004.

[8] F. Y. Leu, C. Y. Ko, I. You, K. K. R. Choo, and C. L. Ho, "A smartphone-based wearable sensors for monitoring real-time physiological data," *Computers & Electrical Engineering*, vol. 65, pp. 376-392, Jan 2018.

[9] M. Z. Poh, N. C. Swenson, and R. W. Picard, "A Wearable Sensor for Unobtrusive, Long-Term Assessment of Electrodermal Activity," *Ieee Transactions on Biomedical Engineering*, vol. 57, pp. 1243-1252, May 2010.

[10] B. W. An, J. H. Shin, S. Y. Kim, J. Kim, S. Ji, J. Park, *et al.*, "Smart Sensor Systems for Wearable Electronic Devices," *Polymers*, vol. 9, Aug 2017.

[11] S. Han, J. Kim, S. M. Won, Y. J. Ma, D. Kang, Z. Q. Xie, *et al.*, "Battery-free, wireless sensors for full-body pressure and temperature mapping," *Science Translational Medicine*, vol. 10, Apr 2018.

[12] A. Kalita, S. Hussain, A. H. Malik, N. V. V. Subbarao, and P. K. Iyer, "Vapor phase sensing of ammonia at the sub-ppm level using a perylene diimide thin film device," *Journal of Materials Chemistry C*, vol. 3, pp. 10767-10774, 2015.

[13] M. A. Carskadon, S. E. Labyak, C. Acebo, and R. Seifer, "Intrinsic circadian period of adolescent humans measured in conditions of forced desynchrony," *Neuroscience Letters*, vol. 260, pp. 129-132, Jan 1999.

[14] S. M. Abbott, K. J. Reid, and P. C. Zee, "Circadian Rhythm Sleep-Wake Disorders," *Psychiatric Clinics of North America*, vol. 38, pp. 805-+, Dec 2015.

[15] Y. Huang, X. Zeng, W. D. Wang, X. H. Guo, C. Hao, W. D. Pan, *et al.*, "High-resolution flexible temperature sensor based graphite-filled polyethylene oxide and polyvinylidene fluoride composites for body temperature monitoring," *Sensors and Actuators a-Physical*, vol. 278, pp. 1-10, Aug 2018.

[16] R. C. Webb, A. P. Bonifas, A. Behnaz, Y. H. Zhang, K. J. Yu, H. Y. Cheng, *et al.*, "Ultrathin conformal devices for precise and continuous thermal characterization of human skin," *Nature Materials*, vol. 12, pp. 938-944, Oct 2013.

[17] K. Y. Shin, J. S. Lee, and J. Jang, "Highly sensitive, wearable and wireless pressure sensor using free-standing ZnO nanoneedle/PVDF hybrid thin film for heart rate monitoring," *Nano Energy*, vol. 22, pp. 95-104, Apr 2016.

[18] O. Y. Kweon, S. J. Lee, and J. H. Oh, "Wearable high-performance pressure sensors based on three-dimensional electrospun conductive nanofibers," *Npg Asia Materials*, vol. 10, Jun 2018.

[19] P. Slobodian, P. Riha, R. Benlikaya, P. Svoboda, and D. Petras, "A Flexible Multifunctional Sensor Based on Carbon Nanotube/Polyurethane Composite," *Ieee Sensors Journal*, vol. 13, pp. 4045-4048, Oct 2013.

[20] T. Q. Trung and N. E. Lee, "Flexible and Stretchable Physical Sensor Integrated Platforms for Wearable Human-Activity Monitoring and Personal Healthcare," *Advanced Materials*, vol. 28, pp. 4338-4372, Jun 2016.

[21] T. Yamada, Y. Hayamizu, Y. Yamamoto, Y. Yomogida, A. Izadi-Najafabadi, D. N. Futaba, *et al.*, "A stretchable carbon nanotube strain sensor for human-motion detection," *Nature Nanotechnology*, vol. 6, pp. 296-301, May 2011.

[22] H. Y. Y. Nyein, W. Gao, Z. Shahpar, S. Emaminejad, S. Challa, K. Chen, *et al.*, "A Wearable Electrochemical Platform for Noninvasive Simultaneous Monitoring of Ca2+ and pH," *ACS Nano*, vol. 10, pp. 7216-7224, Jul 2016.

[23] Z. Sonner, E. Wilder, J. Heikenfeld, G. Kasting, F. Beyette, D. Swaile, *et al.*, "The microfluidics of the eccrine sweat gland, including biomarker partitioning, transport, and biosensing implications," *Biomicrofluidics*, vol. 9, May 2015.

[24] R. J. Maughan and S. M. Shirreffs, "Dehydration and rehydration in competative sport," *Scandinavian Journal of Medicine & Science in Sports*, vol. 20, pp. 40-47, Oct 2010.

[25] S. M. Shirreffs and R. J. Maughan, "Whole body sweat collection in humans: An improved method with preliminary data on electrolyte content," *Journal of Applied Physiology*, vol. 82, pp. 336-341, Jan 1997.

[26] L. B. Baker, J. R. Stofan, H. C. Lukaski, and C. A. Horswill, "Exercise-Induced Trace Mineral Element Concentration in Regional Versus Whole-Body Wash-Down Sweat," *International Journal of Sport Nutrition and Exercise Metabolism*, vol. 21, pp. 233-239, Jun 2011.

[27] A. Koh, D. Kang, Y. Xue, S. Lee, R. M. Pielak, J. Kim, *et al.*, "A soft, wearable microfluidic device for the capture, storage, and colorimetric sensing of sweat," *Science Translational Medicine*, vol. 8, Nov 2016.

[28] J. Heikenfeld, "Non-invasive Analyte Access and Sensing through Eccrine Sweat: Challenges and Outlook circa 2016," *Electroanalysis*, vol. 28, pp. 1242-1249, Jun 2016.

[29] H. Y. Y. Nyein, L. C. Tai, Q. P. Ngo, M. H. Chao, G. B. Zhang, W. Gao, *et al.*, "A Wearable Microfluidic Sensing Patch for Dynamic Sweat Secretion Analysis," *Acs Sensors*, vol. 3, pp. 944-952, May 2018.

[30] W. H. Yeo, Y. S. Kim, J. Lee, A. Ameen, L. K. Shi, M. Li, *et al.*, "Multifunctional Epidermal Electronics Printed Directly Onto the Skin," *Advanced Materials,* vol. 25, pp. 2773-2778, May 2013.

[31] F. R. Fan, W. Tang, and Z. L. Wang, "Flexible Nanogenerators for Energy Harvesting and Self-Powered Electronics," *Advanced Materials,* vol. 28, pp. 4283-4305, Jun 2016.

[32] A. Shimoni, S. Azoubel, and S. Magdassi, "Inkjet printing of flexible high-performance carbon nanotube transparent conductive films by "coffee ring effect"," *Nanoscale,* vol. 6, pp. 11084-11089, 2014.

[33] M. Tijero, R. Diez-Ahedo, F. Benito-Lopez, L. Basabe-Desmonts, V. Castro-Lopez, and A. Valero, "Biomolecule storage on non-modified thermoplastic microfluidic chip by ink-jet printing of ionogels," *Biomicrofluidics,* vol. 9, Jul 2015.

[34] G. Percin and B. T. Khuri-Yakub, "Micromachined droplet ejector arrays for controlled ink-jet printing and deposition," *Review of Scientific Instruments,* vol. 73, pp. 2193-2196, May 2002.

[35] P. Ferraro, S. Coppola, S. Grilli, M. Paturzo, and V. Vespini, "Dispensing nano-pico droplets and liquid patterning by pyroelectrodynamic shooting," *Nature Nanotechnology,* vol. 5, pp. 429-435, Jun 2010.

[36] S. Mishra, K. L. Barton, A. G. Alleyne, P. M. Ferreira, and J. A. Rogers, "High-speed and drop-on-demand printing with a pulsed electrohydrodynamic jet," *Journal of Micromechanics and Microengineering,* vol. 20, Sep 2010.

[37] M. K. Tan, J. R. Friend, and L. Y. Yeo, "Interfacial Jetting Phenomena Induced by Focused Surface Vibrations," *Physical Review Letters,* vol. 103, Jul 2009.

[38] N. C. Schirmer, C. Kullmann, M. S. Schmid, B. R. Burg, T. Schwamb, and D. Poulikakos, "On Ejecting Colloids Against Capillarity from Sub-micrometer Openings: On-Demand Dielectrophoretic Nanoprinting," *Advanced Materials,* vol. 22, pp. 4701-+, Nov 2010.

[39] R. D. Piner, J. Zhu, F. Xu, S. H. Hong, and C. A. Mirkin, ""Dip-pen" nanolithography," *Science,* vol. 283, pp. 661-663, Jan 1999.

[40] H. Taha, R. S. Marks, L. A. Gheber, I. Rousso, J. Newman, C. Sukenik, *et al.*, "Protein printing with an atomic force sensing nanofountainpen," *Applied Physics Letters,* vol. 83, pp. 1041-1043, Aug 2003.

[41] X. Zhou, H. H. Xu, J. Y. Cheng, N. Zhao, and S. C. Chen, "Flexure-based Roll-to-roll Platform: A Practical Solution for Realizing Large-area Microcontact Printing," *Scientific Reports,* vol. 5, Jun 2015.

[42] C. H. Ru, J. Luo, S. R. Xie, and Y. Sun, "A review of non-contact micro- and nano-printing technologies," *Journal of Micromechanics and Microengineering,* vol. 24, May 2014.

[43] S. Kamisuki, T. Hagata, C. Tezuka, Y. Nose, M. Fujii, and M. Atobe, "A low power, small, electrostatically-driven commercial inkjet head," in *Proceedings MEMS 98. IEEE. Eleventh Annual International Workshop on Micro Electro Mechanical Systems. An Investigation of Micro Structures, Sensors, Actuators, Machines and Systems (Cat. No.98CH36176*, 1998, pp. 63-68.

[44] (2006). *Ink-Jet - an overview | ScienceDirect Topics*. Available: https://www.sciencedirect.com/topics/chemistry/ink-jet

[45] S. Mahshid, J. Lu, A. A. Abidi, R. Sladek, W. W. Reisner, and M. J. Ahamed, "Transverse dielectrophoretic-based DNA nanoscale confinement," *Scientific Reports*, vol. 8, Apr 2018.

[46] A. Nakano and A. Ros, "Protein dielectrophoresis: Advances, challenges, and applications," *Electrophoresis*, vol. 34, pp. 1085-1096, Apr 2013.

[47] B. A. Simmons, G. J. McGraw, R. V. Davalos, G. J. Fiechtner, Y. Fintschenko, and E. B. Cummings, "The development of polymeric devices as dielectrophoretic separators and concentrators," *Mrs Bulletin*, vol. 31, pp. 120-124, Feb 2006.

[48] A. C. Kandemir, D. Erdem, H. Ma, A. Reiser, and R. Spolenak, "Polymer nanocomposite patterning by dippen nanolithography," *Nanotechnology*, vol. 27, Apr 2016.

[49] S. W. Chung, D. S. Ginger, M. W. Morales, Z. F. Zhang, V. Chandrasekhar, M. A. Ratner, *et al.*, "Top-down meets bottom-up: Dip-pen nanolithography and DNA-directed assembly of nanoscale electrical circuits," *Small*, vol. 1, pp. 64-69, Jan 2005.

[50] J. Kim, Y. H. Shin, S. H. Yun, D. S. Choi, J. H. Nam, S. R. Kim, *et al.*, "Direct-Write Patterning of Bacterial Cells by Dip-Pen Nanolithography," *Journal of the American Chemical Society*, vol. 134, pp. 16500-16503, Oct 2012.

[51] K. B. Lee, S. J. Park, C. A. Mirkin, J. C. Smith, and M. Mrksich, "Protein nanoarrays generated by dip-pen nanolithography," *Science*, vol. 295, pp. 1702-1705, Mar 2002.

[52] B. A. Nelson, W. P. King, A. R. Laracuente, P. E. Sheehan, and L. J. Whitman, "Direct deposition of continuous metal nanostructures by thermal dip-pen nanolithography," *Applied Physics Letters*, vol. 88, Jan 2006.

[53] A. Lewis, Y. Kheifetz, E. Shambrodt, A. Radko, E. Khatchatryan, and C. Sukenik, "Fountain pen nanochemistry: Atomic force control of chrome etching," *Applied Physics Letters*, vol. 75, pp. 2689-2691, Oct 1999.

[54] K. Lieberman, A. Lewis, G. Fish, S. Shalom, T. M. Jovin, A. Schaper, *et al.*, "MULTIFUNCTIONAL, MICROPIPETTE BASED FORCE CANTILEVERS FOR SCANNED PROBE MICROSCOPY," *Applied Physics Letters*, vol. 65, pp. 648-650, Aug 1994.

[55] M. K. Ghatkesar, H. H. P. Garza, F. Heuck, and U. Staufer, "Scanning Probe Microscope-Based Fluid Dispensing," *Micromachines*, vol. 5, pp. 954-1001, Dec 2014.

[56] M. Sokuler and L. A. Gheber, "Nano fountain pen manufacture of polymer lenses for nano-biochip applications," *Nano Letters*, vol. 6, pp. 848-853, Apr 2006.

[57] T. Yeshua, M. Layani, R. Dekhter, U. Huebner, S. Magdassi, and A. Lewis, "Micrometer to 15 nm Printing of Metallic Inks with Fountain Pen Nanolithography," *Small*, vol. 14, Jan 2018.

[58] T. Yeshua, C. Lehmann, U. Hubner, S. Azoubel, S. Magdassi, E. E. B. Campbell, *et al.*, "Nanodrawing of Aligned Single Carbon Nanotubes with a Nanopen," *Nano Letters*, vol. 16, pp. 1517-1522, Mar 2016.

[59] D. A. Bullen, X. Wang, J. Zou, S.-W. Chung, C. Liu, and C. A. Mirkin, "Development of Parallel Dip Pen Nanolithography Probe Arrays for High Throughput Nanolithography," *MRS Proceedings*, vol. 758, p. LL4.2, 2011.

[60] C. Ru, J. Luo, S. Xie, and Y. Sun, "A review of non-contact micro- and nano-printing technologies," *Journal of Micromechanics and Microengineering*, vol. 24, May 2014.

[61] S. H. Ko, H. Pan, C. P. Grigoropoulos, C. K. Luscombe, J. M. J. Frechet, and D. Poulikakos, "All-inkjet-printed flexible electronics fabrication on a polymer substrate by

low-temperature high-resolution selective laser sintering of metal nanoparticles," *Nanotechnology,* vol. 18, Aug 2007.

[62] H. Sirringhaus, T. Kawase, R. H. Friend, T. Shimoda, M. Inbasekaran, W. Wu, *et al.*, "High-resolution inkjet printing of all-polymer transistor circuits," *Science,* vol. 290, pp. 2123-2126, Dec 2000.

[63] L. Setti, A. Fraleoni-Morgera, B. Ballarin, A. Filippini, D. Frascaro, and C. Piana, "An amperometric glucose biosensor prototype fabricated by thermal inkjet printing," *Biosensors & Bioelectronics,* vol. 20, pp. 2019-2026, Apr 2005.

[64] J. Li, F. Rossignol, and J. Macdonald, "Inkjet printing for biosensor fabrication: combining chemistry and technology for advanced manufacturing," *Lab on a Chip,* vol. 15, pp. 2538-2558, 2015 2015.

[65] B. Derby, "Inkjet Printing of Functional and Structural Materials: Fluid Property Requirements, Feature Stability, and Resolution," in *Annual Review of Materials Research, Vol 40*. vol. 40, D. R. Clarke, M. Ruhle, and F. Zok, Eds., ed, 2010, pp. 395-414.

[66] R. P. Tortorich and J. W. Choi, "Inkjet Printing of Carbon Nanotubes," *Nanomaterials,* vol. 3, pp. 453-468, Sep 2013.

[67] Y. L. Ta and Z. G. Yang, "Flexible, Transparent, Thickness-Controllable SWCNT/PEDOT:PSS Hybrid Films Based on Coffee-Ring Lithography for Functional Noncontact Sensing Device," *Langmuir,* vol. 31, pp. 13257-13264, Dec 2015.

[68] B. Derby, "Bioprinting: inkjet printing proteins and hybrid cell-containing materials and structures," *Journal of Materials Chemistry,* vol. 18, pp. 5717-5721, 2008.

[69] G. M. Nishioka, A. A. Markey, and C. K. Holloway, "Protein damage in drop-on-demand printers," *Journal of the American Chemical Society,* vol. 126, pp. 16320-16321, Dec 22 2004.

[70] J.-U. Park, M. Hardy, S. J. Kang, K. Barton, K. Adair, D. K. Mukhopadhyay, *et al.*, "High-resolution electrohydrodynamic jet printing," *Nature Materials,* vol. 6, pp. 782-789, Oct 2007.

[71] M. S. Onses, E. Sutanto, P. M. Ferreira, A. G. Alleyne, and J. A. Rogers, "Mechanisms, Capabilities, and Applications of High-Resolution Electrohydrodynamic Jet Printing," *Small,* vol. 11, pp. 4237-4266, Sep 9 2015.

[72] K. Kim, G. Kim, B. R. Lee, S. Ji, S.-Y. Kim, B. W. An, *et al.*, "High-resolution electrohydrodynamic jet printing of small-molecule organic light-emitting diodes," *Nanoscale,* vol. 7, pp. 13410-13415, 2015 2015.

[73] R. T. Collins, J. J. Jones, M. T. Harris, and O. A. Basaran, "Electrohydrodynamic tip streaming and emission of charged drops from liquid cones," *Nature Physics,* vol. 4, pp. 149-154, Feb 2008.

[74] S. Coppola, L. Mecozzi, V. Vespini, L. Battista, S. Grilli, G. Nenna, *et al.*, "Nanocomposite polymer carbon-black coating for triggering pyro-electrohydrodynamic inkjet printing," *Applied Physics Letters,* vol. 106, Jun 2015.

[75] D. J. Lipomi, M. Vosgueritchian, B. C. K. Tee, S. L. Hellstrom, J. A. Lee, C. H. Fox, *et al.*, "Skin-like pressure and strain sensors based on transparent elastic films of carbon nanotubes," *Nature Nanotechnology,* vol. 6, pp. 788-792, Dec 2011.

[76] T. Schwamb, N. C. Schirmer, B. R. Burg, and D. Poulikakos, "Fountain-pen controlled dielectrophoresis for carbon nanotube-integration in device assembly," *Applied Physics Letters,* vol. 93, Nov 2008.

[77] T. Y. Choi, D. Poulikakos, and C. P. Grigoropoulos, "Fountain-pen-based laser microstructuring with gold nanoparticle inks," *Applied Physics Letters,* vol. 85, pp. 13-15, Jul 5 2004.

[78] B. Kang, H. Min, U. Seo, J. Lee, N. Park, K. Cho, *et al.*, "Directly Drawn Organic Transistors by Capillary Pen: A New Facile Patterning Method using Capillary Action for Soluble Organic Materials," *Advanced Materials,* vol. 25, pp. 4117-4122, Aug 2013.

[79] J. W. Han, B. Kim, J. Li, and M. Meyyappan, "A carbon nanotube based ammonia sensor on cellulose paper," *Rsc Advances,* vol. 4, pp. 549-553, 2014.

[80] K. A. Mirica, J. M. Azzarelli, J. G. Weis, J. M. Schnorr, and T. M. Swager, "Rapid prototyping of carbon-based chemiresistive gas sensors on paper," *Proceedings of the National Academy of Sciences of the United States of America,* vol. 110, pp. E3265-E3270, Aug 2013.

[81] C. W. Lin, Z. B. Zhao, J. Kim, and J. X. Huang, "Pencil Drawn Strain Gauges and Chemiresistors on Paper," *Scientific Reports,* vol. 4, Jan 2014.

[82] L. M. Demers, D. S. Ginger, S. J. Park, Z. Li, S. W. Chung, and C. A. Mirkin, "Direct patterning of modified oligonucleotides on metals and insulators by dip-pen nanolithography," *Science,* vol. 296, pp. 1836-1838, Jun 7 2002.

[83] J. Chung, K. H. Lee, J. Lee, and R. S. Ruoff, "Toward Large Scale Integration of Carbon Nanotubes," *Langmuir,* vol. 20, pp. 3011-3017, 2004.

[84] D. A. Brown, J.-H. Kim, H.-B. Lee, G. Fotouhi, K.-H. Lee, W. K. Liu, *et al.*, "Electric Field Guided Assembly of One-Dimensional Nanostructures for High Performance Sensors," *Sensors,* vol. 12, pp. 5725-5751, May 2012.

[85] M. Burghard, G. Duesberg, G. Philipp, J. Muster, and S. Roth, "Controlled adsorption of carbon nanotubes on chemically modified electrode arrays," *Advanced Materials,* vol. 10, pp. 584-+, Jun 1998.

[86] J. Kim, M.-W. Moon, K.-R. Lee, L. Mahadevan, and H.-Y. Kim, "Hydrodynamics of Writing with Ink," *Physical Review Letters,* vol. 107, Dec 20 2011.

[87] C. A. Pope, 3rd, R. T. Burnett, G. D. Thurston, M. J. Thun, E. E. Calle, D. Krewski, *et al.*, "Cardiovascular mortality and long-term exposure to particulate air pollution: epidemiological evidence of general pathophysiological pathways of disease," *Circulation,* vol. 109, pp. 71-7, Jan 6 2004.

[88] D. W. Dockery, C. A. Pope, 3rd, X. Xu, J. D. Spengler, J. H. Ware, M. E. Fay, *et al.*, "An association between air pollution and mortality in six U.S. cities," *N Engl J Med,* vol. 329, pp. 1753-9, Dec 9 1993.

[89] F. Dominici, R. D. Peng, M. L. Bell, L. Pham, A. McDermott, S. L. Zeger, *et al.*, "Fine particulate air pollution and hospital admission for cardiovascular and respiratory diseases," *JAMA,* vol. 295, pp. 1127-34, Mar 8 2006.

[90] S. Becker, L. A. Dailey, J. M. Soukup, S. C. Grambow, R. B. Devlin, and Y. C. Huang, "Seasonal variations in air pollution particle-induced inflammatory mediator release and oxidative stress," *Environ Health Perspect,* vol. 113, pp. 1032-8, Aug 2005.

[91] C. A. Dick, P. Singh, M. Daniels, P. Evansky, S. Becker, and M. I. Gilmour, "Murine pulmonary inflammatory responses following instillation of size-fractionated ambient particulate matter," *J Toxicol Environ Health A,* vol. 66, pp. 2193-2207, Dec 12 2003.

[92] M. I. Gilmour, J. McGee, R. M. Duvall, L. Dailey, M. Daniels, E. Boykin, *et al.*, "Comparative toxicity of size-fractionated airborne particulate matter obtained from different cities in the United States," *Inhal Toxicol,* vol. 19 Suppl 1, pp. 7-16, 2007.

[93] M. S. Happo, R. O. Salonen, A. I. Halinen, P. I. Jalava, A. S. Pennanen, V. M. Kosma, *et al.*, "Dose and time dependency of inflammatory responses in the mouse lung to urban air coarse, fine, and ultrafine particles from six European cities," *Inhal Toxicol,* vol. 19, pp. 227-46, Mar 2007.

[94] M. I. Gilmour, S. O'Connor, C. A. Dick, C. A. Miller, and W. P. Linak, "Differential pulmonary inflammation and in vitro cytotoxicity of size-fractionated fly ash particles from pulverized coal combustion," *J Air Waste Manag Assoc,* vol. 54, pp. 286-95, Mar 2004.

[95] J. Seagrave, J. D. McDonald, M. D. Reed, S. K. Seilkop, and J. L. Mauderly, "Responses to subchronic inhalation of low concentrations of diesel exhaust and hardwood smoke measured in rat bronchoalveolar lavage fluid," *Inhal Toxicol,* vol. 17, pp. 657-70, Nov 2005.

[96] P. Singh, D. M. DeMarini, C. A. Dick, D. G. Tabor, J. V. Ryan, W. P. Linak, *et al.*, "Sample characterization of automobile and forklift diesel exhaust particles and comparative pulmonary toxicity in mice," *Environ Health Perspect,* vol. 112, pp. 820-5, Jun 2004.

[97] J. Zhang, X. H. Liu, G. Neri, and N. Pinna, "Nanostructured Materials for Room-Temperature Gas Sensors," *Advanced Materials,* vol. 28, pp. 795-831, Feb 2016.

[98] D. E. Motaung, G. H. Mhlongo, A. S. Bolokang, B. P. Dhonge, H. C. Swart, and S. S. Ray, "Improved sensitivity and selectivity of pristine zinc oxide nanostructures to H2S gas: Detailed study on the synthesis reaction time," *Applied Surface Science,* vol. 386, pp. 210-223, Nov 2016.

[99] Z. J. Li, Z. J. Lin, N. N. Wang, J. Q. Wang, W. Liu, K. Sun, *et al.*, "High precision NH3 sensing using network nano-sheet Co3O4 arrays based sensor at room temperature," *Sensors and Actuators B-Chemical,* vol. 235, pp. 222-231, Nov 2016.

[100] S. G. Surya, B. S. N. Ashwath, S. Mishra, A. R. B. Karthik, A. B. Sastry, B. L. V. Prasad, *et al.*, "H2S detection using low-cost SnO2 nano-particle Bi-layer OFETs," *Sensors and Actuators B-Chemical,* vol. 235, pp. 378-385, Nov 2016.

[101] K. K. Sadasivuni, D. Ponnamma, H. U. Ko, H. C. Kim, L. Zhai, and J. Kim, "Flexible NO2 sensors from renewable cellulose nanocrystals/iron oxide composites," *Sensors and Actuators B-Chemical,* vol. 233, pp. 633-638, Oct 2016.

[102] L. W. Wang, Y. H. Wang, K. F. Yu, S. P. Wang, Y. Y. Zhang, and C. S. Wei, "A novel low temperature gas sensor based on Pt-decorated hierarchical 3D SnO2 nanocomposites," *Sensors and Actuators B-Chemical,* vol. 232, pp. 91-101, Sep 2016.

[103] M. I. Kim and Y.-S. Lee, "A Comprehensive Review of Gas Sensors Using Carbon Materials," *Journal of nanoscience and nanotechnology,* vol. 16, 2016 2016.

[104] M. Meyyappan, "Carbon Nanotube-Based Chemical Sensors," *Small,* vol. 12, pp. 2118-2129, Apr 2016.

[105] N. L. W. Septiani and B. Yuliarto, "Review-The Development of Gas Sensor Based on Carbon Nanotubes," *Journal of the Electrochemical Society,* vol. 163, pp. B97-B106, 2016.

[106] U. Latif and F. L. Dickert, "Graphene Hybrid Materials in Gas Sensing Applications," *Sensors,* vol. 15, pp. 30504-30524, Dec 2015.

[107] K. Balasubramanian and K. Kern, "25th Anniversary Article: Label-Free Electrical Biodetection Using Carbon Nanostructures," *Advanced Materials,* vol. 26, pp. 1154-1175, Feb 2014.

[108] J. Kong, N. R. Franklin, C. W. Zhou, M. G. Chapline, S. Peng, K. J. Cho, *et al.*, "Nanotube molecular wires as chemical sensors," *Science*, vol. 287, pp. 622-625, Jan 2000.
[109] J. Li, Y. J. Lu, Q. Ye, M. Cinke, J. Han, and M. Meyyappan, "Carbon nanotube sensors for gas and organic vapor detection," *Nano Letters*, vol. 3, pp. 929-933, Jul 2003.
[110] Q. F. Pengfei, O. Vermesh, M. Grecu, A. Javey, O. Wang, H. J. Dai, *et al.*, "Toward large arrays of multiplex functionalized carbon nanotube sensors for highly sensitive and selective molecular detection," *Nano Letters*, vol. 3, pp. 347-351, Mar 2003.
[111] K. Persaud and G. Dodd, "ANALYSIS OF DISCRIMINATION MECHANISMS IN THE MAMMALIAN OLFACTORY SYSTEM USING A MODEL NOSE," *Nature*, vol. 299, pp. 352-355, 1982.
[112] Y. J. Lu, M. Meyyappan, and J. Li, "Fabrication of carbon-nanotube-based sensor array and interference study," *Journal of Materials Research*, vol. 26, pp. 2017-2023, Aug 2011.
[113] H. Ogihara, H. Kibayashi, and T. Saji, "Microcontact Printing for Patterning Carbon Nanotube/Polymer Composite Films with Electrical Conductivity," *Acs Applied Materials & Interfaces*, vol. 4, pp. 4891-4897, Sep 2012.
[114] T. Zhang, S. Mubeen, N. V. Myung, and M. A. Deshusses, "Recent progress in carbon nanotube-based gas sensors," *Nanotechnology*, vol. 19, p. 33201, 2008.
[115] G. Sulis, R. Centis, G. Sotgiu, L. D'Ambrosio, E. Pontali, A. Spanevello, *et al.*, "Recent developments in the diagnosis and management of tuberculosis," *Npj Primary Care Respiratory Medicine*, vol. 26, Nov 2016.
[116] S. Gupta and V. Kakkar, "Recent technological advancements in tuberculosis diagnostics - A review," *Biosensors & Bioelectronics*, vol. 115, pp. 14-29, Sep 2018.
[117] C. f. D. C. a. Prevention, *Guidelines for Preventing the Transmission of Mycobacterium tuberculosis in HealthCare Settings* vol. 54(No. RR-17), 2005.
[118] E. Sada, D. Aguilar, M. Torres, and T. Herrera, "DETECTION OF LIPOARABINOMANNAN AS A DIAGNOSTIC-TEST FOR TUBERCULOSIS," *Journal of Clinical Microbiology*, vol. 30, pp. 2415-2418, Sep 1992.
[119] K. Dheda, M. Ruhwald, G. Theron, J. Peter, and W. C. Yam, "Point-of-care diagnosis of tuberculosis: Past, present and future," *Respirology*, vol. 18, pp. 217-232, Feb 2013.
[120] A. L. Garcia-Basteiro, A. DiNardo, B. Saavedr, D. R. Silva, D. Palmero, M. Gegia, *et al.*, "Point of care diagnostics for tuberculosis," *Pulmonology*, vol. 24, pp. 73-85, Mar-Apr 2018.
[121] C. C. Boehme, P. Nabeta, D. Hillemann, M. P. Nicol, S. Shenai, F. Krapp, *et al.*, "Rapid Molecular Detection of Tuberculosis and Rifampin Resistance," *New England Journal of Medicine*, vol. 363, pp. 1005-1015, Sep 9 2010.
[122] A. Luabeya, R. Wood, J. Shenje, E. Filander, C. Ontong, S. Mabwe, *et al.*, "Non-invasive detection of tuberculosis by oral swab analysis," *J Clin Microbiol. 2018*, p. PubMed PMID: 30541931, 2019.
[123] R. C. Wood, A. K. Luabeya, K. M. Weigel, A. K. Wilbur, L. Jones-Engel, M. Hatherill, *et al.*, "Detection of Mycobacterium tuberculosis DNA on the oral mucosa of tuberculosis patients," *Scientific Reports*, vol. 5, Mar 2015.
[124] A. Maroto, K. Balasubramanian, M. Burghard, and K. Kern, "Functionalized metallic carbon nanotube devices for pH sensing," *Chemphyschem*, vol. 8, pp. 220-223, Feb 2 2007.

[125] H. R. Byon and H. C. Choi, "Network single-walled carbon nanotube-field effect transistors (SWNT-FETs) with increased Schottky contact area for highly sensitive biosensor applications," *Journal of the American Chemical Society*, vol. 128, pp. 2188-2189, Feb 22 2006.

[126] C. Li, M. Curreli, H. Lin, B. Lei, F. N. Ishikawa, R. Datar, *et al.*, "Complementary detection of prostate-specific antigen using ln(2)O(3) nanowires and carbon nanotubes," *Journal of the American Chemical Society*, vol. 127, pp. 12484-12485, Sep 14 2005.

[127] I. Heller, A. M. Janssens, J. Mannik, E. D. Minot, S. G. Lemay, and C. Dekker, "Identifying the mechanism of biosensing with carbon nanotube transistors," *Nano Letters*, vol. 8, pp. 591-595, Feb 2008.

[128] B. L. Allen, P. D. Kichambare, and A. Star, "Carbon nanotube field-effect-transistor-based biosensors," *Advanced Materials*, vol. 19, pp. 1439-1451, Jun 4 2007.

[129] D. J. Lee, Y. Chander, S. M. Goyal, and T. H. Cui, "Carbon nanotube electric immunoassay for the detection of swine influenza virus H1N1," *Biosensors & Bioelectronics*, vol. 26, pp. 3482-3487, Apr 2011.

[130] M. S. Yoo, M. Shin, Y. Kim, M. Jang, Y. E. Choi, S. J. Park, *et al.*, "Development of electrochemical biosensor for detection of pathogenic microorganism in Asian dust events," *Chemosphere*, vol. 175, pp. 269-274, May 2017.

[131] D. Wasik, A. Mulchandani, and M. V. Yates, "A heparin-functionalized carbon nanotube-based affinity biosensor for dengue virus," *Biosensors & Bioelectronics*, vol. 91, pp. 811-816, May 2017.

[132] R. Singh, A. Sharma, S. Hong, and J. Jang, "Electrical immunosensor based on dielectrophoretically-deposited carbon nanotubes for detection of influenza virus H1N1," *Analyst*, vol. 139, pp. 5415-5421, 2014.

[133] A. Sobhan, J. H. Oh, M. K. Park, and J. Lee, "Detection of Peanut Allergen Ara h 6 in Commercially Processed Foods using a Single-Walled Carbon Nanotube-Based Biosensor," *Journal of Aoac International*, vol. 101, pp. 1558-1565, Sep-Oct 2018.

[134] P. Ramnani, Y. N. Gao, M. Ozsoz, and A. Mulchandani, "Electronic Detection of MicroRNA at Attomolar Level with High Specificity," *Analytical Chemistry*, vol. 85, pp. 8061-8064, Sep 2013.

[135] J.-H. Kim, M. Hiraiwa, H.-B. Lee, K.-H. Lee, G. A. Cangelosi, and J.-H. Chung, "Electrolyte-free amperometric immunosensor using a dendritic nanotip," *Rsc Advances*, vol. 3, pp. 4281-4287, 2013 2013.

[136] C. T. Kim, J. H. Kim, J. H. Chung, H. G. Lee, and S. J. Jun, "Single Walled Carbon Nanotube-Based Junction Biosensor for Detection of Escherichia coli," *Plos One*, vol. 9, p. e105767, 2014.